Probing the blueprint of life

Sitters, G.

2015

Probing the blueprint of life

The development and application of novel single molecule methods

Gerrit Sitters

This thesis was reviewed by the following committee:

Prof. dr. Wesley P. Wong
Harvard Medical School, Boston, USA

Prof. dr. Lene B. Oddershede
Niels Bohr Institute, Copenhagen, Denmark

Prof. dr. Menno W.J. Prins
Eindhoven University of Technology, Eindhoven, the Netherlands

Prof. dr. Nynke H. Dekker
Delft University of Technology, Delft, the Netherlands

Prof. dr. Daniel Bonn
University of Amsterdam, Amsterdam, the Netherlands

Prof. dr. Davide Iannuzzi
VU University Amsterdam, Amsterdam, the Netherlands

Dr. Remus Th. Dame
Leiden University, Leiden, The Netherlands

ISBN: 978-94-6295-291-1
Cover by: Jerom Langeveld
Printed by: Uitgeverij BOXPress, ‘s Hertogenbosch, the Netherlands

A digital version is available at: www.ubvu.vu.nl/dissertations

The production of this thesis is financially supported by LUMICKS B.V. and VU University Amsterdam.

The work in this thesis has been financed by the Netherlands Organisation for Scientific Research (NWO) and via a European Research Council (ERC) starting grant. The research was performed in the Department of Physics and Astronomy at the VU University Amsterdam, Amsterdam, The Netherlands.

VRIJE UNIVERSITEIT

Probing the blueprint of life

The development and application of novel single molecule methods

ACADEMISCH PROEFSCHRIFT

ter verkrijging van de graad Doctor aan
de Vrije Universiteit Amsterdam,
op gezag van de rector magnificus
prof.dr. F.A. van der Duyn Schouten,
in het openbaar te verdedigen
ten overstaan van de promotiecommissie
van de Faculteit der Exacte Wetenschappen
op donderdag 3 december 2015 om 15.45 uur
in de aula van de universiteit,
De Boelelaan 1105

door

Gerrit Sitters

geboren te Eindhoven

promotoren: prof.dr.ir. G.J.L. Wuite
prof.dr.ir. E.J.G. Peterman

Table of Contents

1 Biophysics: Physics of Life

The research described in this thesis is performed in the *single-molecule biophysics* field. Biophysics is the study of biological systems, life, using a physics approach. From a physics point of view living systems consist, just like non-living systems, of matter and therefore obey the laws of physics. Since these laws are well known and there are a lot of mysteries concerning life, physicists have a valuable role in resolving these mysteries. Living matter is organized in an extremely complex manner and is constantly interacting with itself and its surroundings (section 1.1). A valuable method in resolving this complexity is a "bottom-up" approach: understanding how the individual molecular building blocks work and adding complexity along the way. The elegance of life is that although different lifeforms might look fundamentally different (e.g. an elephants compared to a pine tree), they share a large fraction of building blocks: DNA and proteins.

The development of single-molecule technologies (section 1.2) allowed the observation and often manipulation of individual DNA and protein molecules and the interactions between them. Studying life at the single molecule level has the appreciated advantage that one is not measuring the averaged behavior of a large population of molecules, something that is done using conventional biochemical "bulk" approaches. This enables single-molecule methods to measure heterogeneity within a population of molecules and measure their dynamical behavior in real time. In addition, physical manipulation of the biomolecules, such as pulling, twisting and bending provides a lot of additional information.

This first chapter is aimed to briefly introduce the biological systems (section 1.1) and techniques (section 1.2) used in this thesis. The outline of the rest of the thesis is described in section 1.3

1.1 Introducing DNA and its surroundings

1.1.1 Cells, proteins, DNA

Every organism consists of cells, which are the smallest units of life that are able to create new cells in their own image out of raw materials from their environment. A cell, typically tens of microns large, is a closed compartment that contains an enormous amount of proteins (order of a trillion) and at least one DNA molecule. The amount of cells per organism varies enormously per species: from one to several trillion.[1]

Most functions in cells are fulfilled by proteins. They play a central role in a large number of tasks of different processes that are vital for cell survival. Some proteins build up larger structures to give cells distinct form. Some proteins have an enzymatic role to catalyze certain biochemical reactions in the cell, while others repair damaged DNA or play a role in the production of other proteins.

DNA, deoxyribonucleic acid, can be considered as the most important molecule within the cell since it contains all information needed for life functions. It is a long polymeric molecule built up from four different nucleotides, each comprised of a sugar ring, a phosphate group and one of four bases: Adenine (A), Thymine (T), Cytosine (C) or Guanine (G). These four bases form the genetic letters in which the blueprint of life is written. Genes are sections of this code and represent the primary structure of proteins that are built up from amino acids. Three successive nucleotides encode one of twenty possible amino acids, which directly link DNA sequence to the primary structure of proteins. This amino acid chain folds in a well-defined three dimensional structure which is function specific.[2]

1.1.2 Structural properties of DNA

The genetic code comprising all information needed for life is stored in long polymers written in the four letters A, C, G and T. Individual nucleotides, consisting of a sugar ring, a phosphate group and a base, are covalently linked through a sugar-phosphate backbone. Two chains of nucleotides form a double right-handed helical structure with the bases pointing inward. The two strands are connected to each other via base-pairing formed by hydrogen bonds that which only occurs between two complementary nucleotides (Watson-Crick pairs): A only pairs with T

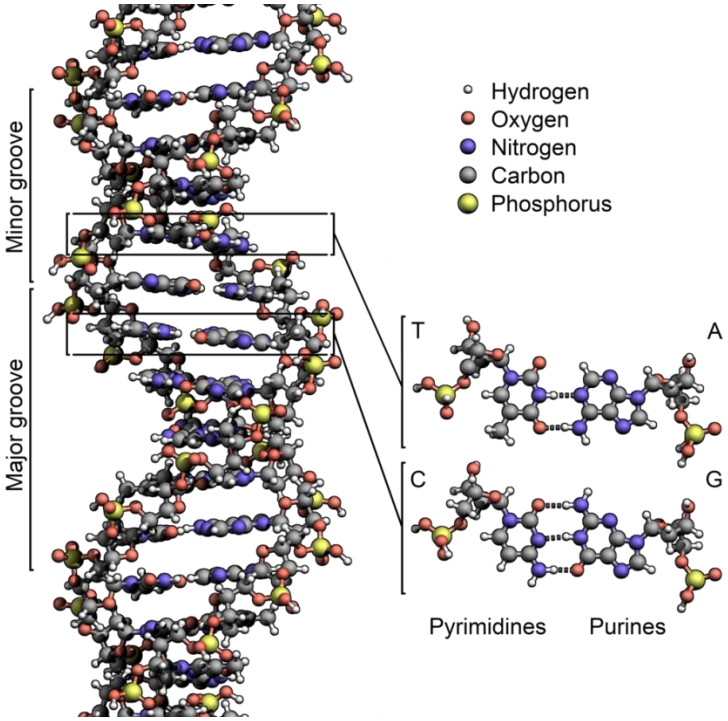

Figure 1.1 Structure of double stranded DNA. Two strands of nucleotides are connected via base-pairing forming a double helical structure. Because the strands are not symmetrically located with respect to each other, the grooves of the helix are unequally spaced resulting in a major and minor groove. Image credit: Wikipedia.

via two hydrogen bond and C only pairs with G via three hydrogen bonds (Figure 1.1). Due to this complementary base-pairing, the two strands themselves are complementary and oriented in an antiparallel fashion. The double helix has a diameter of approximately 2 nm and makes a full turn roughly every 10 base pairs, corresponding to 3.4 nm.[2]

1.1.3 Mechanical properties of DNA

In cells, DNA is constantly interacting in a mechanochemical manner with its cellular environment. While performing their tasks many proteins bend, twist or loop DNA,

causing the elasticity of DNA to affect a wide variety of cellular processes. It is therefore, next to the genetic code, essential to understand the mechanical properties of DNA if one wants to unravel the mysteries of life. Since the first DNA stretching experiments were performed on a single molecule[3] much effort has been devoted to obtain a complete picture of the mechanical properties of DNA. The double helix is a so-called semi-flexible polymer that is remarkable stiff for its small diameter.

Different phases of distinct elastic behavior can be observed when stretching a double stranded DNA molecule up to 100 pN (Figure 1.2). If the ends of the DNA are subjected to low forces (sub piconewton) the DNA's extension will be significantly lower than the contour length due to thermal fluctuations caused by the bombardment of the DNA molecule by solvent molecules. At these low forces the DNA molecule acts as an entropic spring, giving rise to the "entropic regime". By stretching the DNA in the entropic regime the amount of possible conformations of the molecule decrease which leads to a higher entropic force. When the DNA is (almost) fully stretched to its contour length the "enthalpic regime" is entered. In this regime the DNA backbone is stretched which occurs in a fairly linear fashion until the last regime, namely the "overstretching regime", is reached at approximately 65 pN. In this regime the DNA lengthens to approximately 170% of its contour length without the need to apply a substantial amount of extra force, which gives rise to the observed plateau shown in Figure 1.2. It has been shown that this overstretching behavior is a local melting transition of the individual bases and is a reversible process.[4]

The force extension behavior of double stranded DNA is well described by the "extensible worm-like chain model" [5]:

$$F = \frac{k_B T}{L_p}\left[\frac{1}{4}\left(1 - \frac{L}{L_0} + \frac{F}{S}\right)^{-2} - \frac{1}{4} + \frac{L}{L_0} - \frac{F}{S}\right],$$

with F the applied force, k_B Boltzmann constant, T the temperature, L DNA end-to-end extension, L_0 the contour length, L_p the persistence length (~50 nm) and S the DNA stretch modulus (~1200 pN).[6]

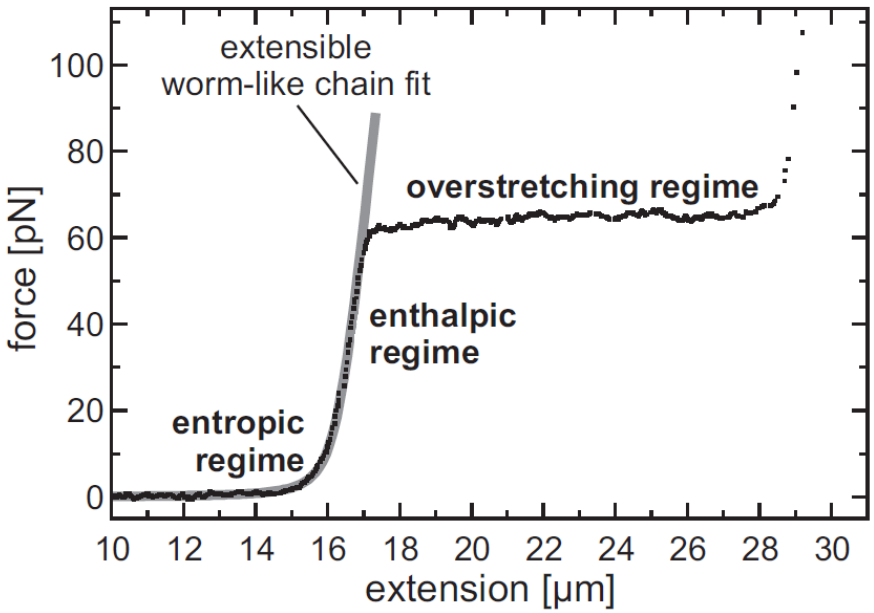

Figure 1.2 Typical force-extension curve of a double stranded DNA molecule with a contour length of 16.45 µm. Several distinct regimes in the elastic behavior is observed as the DNA is pulled to larger extension. Adopted with permission from ref [4].

1.1.4 DNA transcription, replication, repair and organization

DNA in living cells has a highly dynamic and heterogeneous structure on which molecular machineries, proteins, perform specific tasks. Often multiple proteins are involved in a dynamic interplay to accomplish their function. Most DNA-protein interactions can be divided into roughly four categories: DNA replication, transcription, repair and organization (Figure 1.3).[7]

DNA needs to be replicated before a cell can divide. A complex protein machinery consisting of multiple proteins perform this task in four different protein mediated processes. (i) Double stranded DNA is divided into two single strands, which form the templates to form two new double stranded DNA strands. (ii) A primase conducts the second step by laying down primers on an unwound single strand,

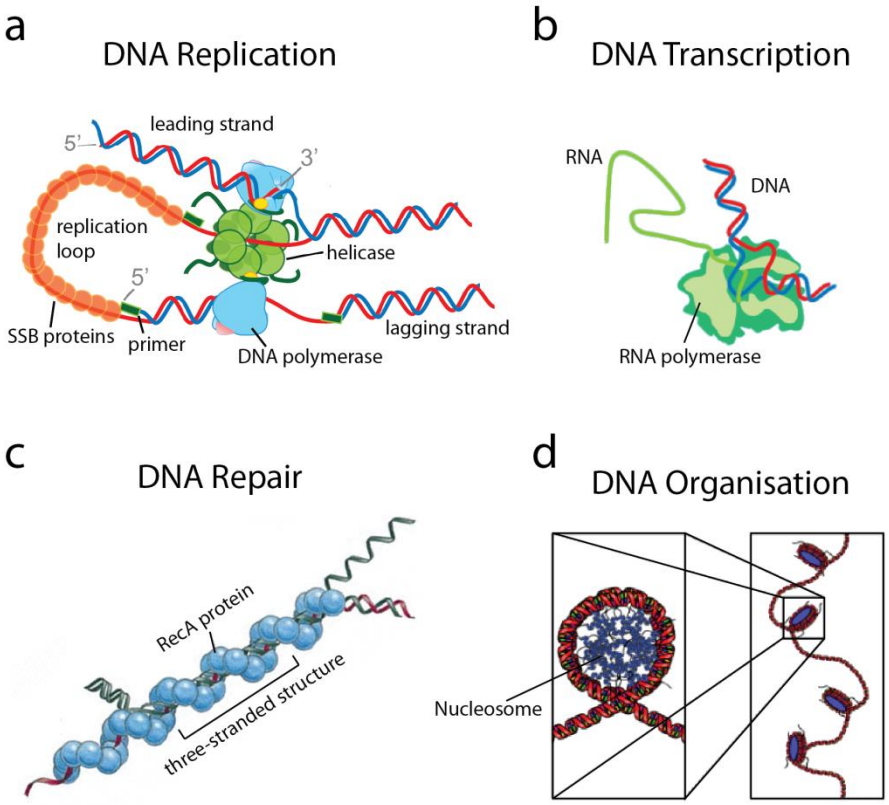

Figure 1.3 Protein-DNA interactions. (**a**) The DNA replication machinery is responsible for creating DNA copies. (**b**) RNA polymerase reads the genetic code of the DNA and transcribes it to RNA. (**c**) RecA plays a role in the homologous recombination DNA-repair pathway by binding to single stranded DNA and forming a structure with the complementary region present on the sister chromosome. (**d**) Eukaryotic DNA is wrapped around histones to from nucleosomes in order to organize the DNA in the nucleus.

which form the launching pad of DNA polymerase that (iii) synthesizes the double stranded DNA by catalyzing the incorporation of complementary nucleotides. DNA polymerase is only able to add nucleotides in the 5'-3' direction, which gives rise to a "leading" and "lagging" strand due to the antiparallel orientation of double stranded DNA. (iv) Single-stranded binding (SSB) proteins are responsible of

protecting the generated single stranded DNA that is created by the DNA helicase (Figure 1.3a).

DNA transcription is the process in which the genetic code on the DNA is read and transcribed to messenger ribonucleic acid (mRNA). This mRNA is translated to proteins by ribosomes, which consist of RNA molecules themselves that are folded in a specific manner. The protein responsible for the transcription of DNA is RNA polymerase (Figure 1.3b).

DNA is constantly corrupted by synthesis errors and damages occurring for example due to free radicals or ultraviolet light. The cell possesses several mechanisms that scan the DNA for damages and recruit the necessary repair proteins to maintain the integrity of the genome. Depending on the type of damage, there are several DNA-repair pathways that can be followed such as homologous recombination (Figure 1.3c), non-homologous end-joining (Chapter 4), base mismatch repair and base excision repair.

DNA in the cell is completely covered with proteins and forms structures called chromosomes. The total length of these chromosomes in the human cell is several meters containing approximately 3 billion base pairs. To fit the chromosomes (23 in the case of a human) in the cell's nucleus the DNA is condensed by specialized proteins. In eukaryotic species (higher order organisms) the DNA is wrapped around small proteins complexes, called histones. These structures fold into higher structures called chromatin (Figure 1.3d). How chromatin is organized influences the transcription of the underlying DNA and is used by the cell to regulate genes expressions.

1.2 Manipulating and imaging methods in this thesis

A large part of the research discussed in this thesis focuses on the development and application of several novel single-molecule tools. This development was driven by two key objectives. The first objective was to bridge the gap between the ideal in vivo and the far more complex in vitro conditions. Practically this means that I want to manipulate and visualize the interactions between DNA and proteins in an environment that better resembles the interior of a cell. To achieve this we combined optical tweezers (section 1.2.1) with confocal (section 1.2.4) and STED microscopy (section 1.2.5), allowing us to measure protein interactions on densely

protein coated DNA in the presence of a high concentration of labeled proteins surrounding the DNA. In cells protein-coated DNA constantly interacts with itself and other DNA molecules. To mimic and measure these interactions we use a method that allows optically trapping two individual DNA molecules and bringing them into contact while visualizing them using wide-field fluorescence microscopy (section 1.2.4). The second important objective was to develop a technique that enables manipulating and measuring a large quantity (hundreds to thousands) of single molecules at the same time. This allows performing statistical analysis on these molecules in one go without the need to repeat a measurement many times. In a first attempt, I tried to achieve this with optical means, by using the radiation pressure of a collimated laser beam (section 1.2.1). The major drawback of this technique, however, is that relatively high laser intensities are needed to exert forces that are biologically relevant. This creates unwanted heating effects and thereby limits the amount of molecules that can be manipulated simultaneously. To overcome these issues we pursued the idea of using acoustic forces to manipulate single molecules (section 1.2.2). This technique proved to be far superior and has, in my mind, a high probability of wide-spread adaptation by the scientific community.

1.2.1 Optical manipulation

Two methods I use to manipulate single biomolecules are based upon optical manipulation: optical tweezers and optical pushing. In Chapters 2, 3 and 4, I make use of optical tweezers which are able to hold and move small micrometer sized objects. Chapter 6 describes optical pushing, a novel method to optically manipulate single molecules.

Optical tweezers are able to trap particles due to the transfer of momentum from light to the micrometer sized objects, which result in a force directed to the focus of the beam. This trapping force can be quantitatively understood in terms of refraction of light rays due to the higher refraction index of the object with respect to its surroundings (Figure 1.4). If the laser beam is tightly focused the momentum transfer from the light to the object will force the object towards the focus of the laser (Figure 1.4a). [8]

In Chapter 6 I use a novel biophysical method that makes use of a collimated laser beam that has a diameter much larger than the manipulated objects. In that case rays A and B have similar intensities causing a net force directed in the travelling direction of the light (Figure 1.4b). By using a large beam diameter it is possible to exert forces on multiple objects simultaneously. To use optical manipulation for

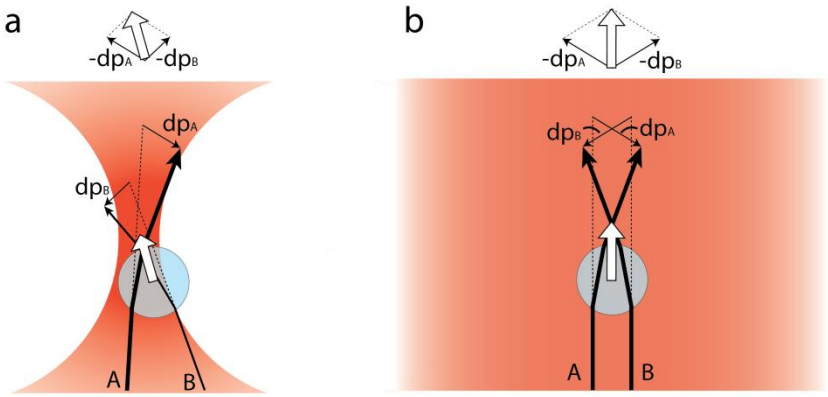

Figure 1.4 Qualitative picture of the origin of the optical forces. Due to a difference in the index of refraction photons are deflected by the microsphere and results in a transfer of momentum from the light to the microsphere. (**a**) In a tightly focused beam the optical force is directed towards the focus. Two light paths, A and B, are compared. The momentum balance is shown at the top. (**b**) In a collimated beam the rays have the same intensity causing a net force directed in the travelling direction of the light.

biophysical purposes we use microspheres which we attach to single DNA molecules that are chemically modified in order to stick to the microspheres and or to a glass surface. In section 1.2.3 the workflow is explained how to "catch" a DNA molecule between two microspheres held in a dual optical trap.

1.2.2 Acoustical manipulation

A completely novel approach to conduct force spectroscopy measurements on biomolecules is discussed in Chapter 7: acoustic force spectroscopy. This method makes use of acoustic forces to manipulate micrometer sized spheres. The device I used is a so called layered resonator (Figure 1.5). In such a device a planar acoustic standing wave is created over a flow cell using a piezo element that is driven by an oscillating voltage. Particles in the flow cell, which are denser than the surrounding medium, will scatter the sound waves causing momentum transfer from the sound to the particles. This causes the particles to be driven towards the closest acoustic pressure node. By changing the voltage over the piezo element the acoustic force

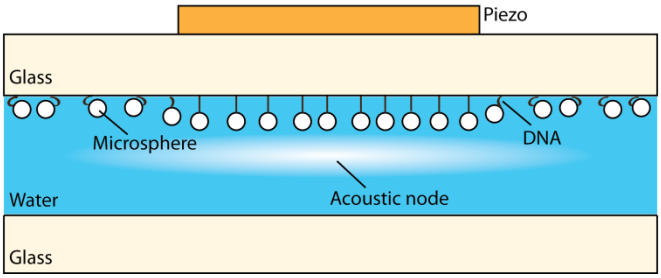

Figure 1.5 Layered resonator device used for acoustic manipulation. The device consists of two glass plates with a fluid chamber in between. An acoustic wave-generating piezo plate is used to create a standing wave over the flow chamber. Microspheres are forced towards the acoustic nodes enabling the manipulation of DNA molecules that are attached to a microsphere at one end and to a surface at the other.

can be tuned. To use acoustic forces to manipulate DNA molecules we tethered them between microspheres and a glass-water interface (**Figure 1.5**). By subjecting the microspheres to a planar acoustic wave they will be forced towards the closest acoustic node, which results in a controllable force on the DNA.

1.2.3 Microfluidics

A crucial element of single-molecule measurements on DNA and proteins is the control of the chemical environment of the assay. In our measurements this is achieved by the use of a microfluidic chip. Microfluidics allows the fine control of tiny volumes of solutions. Experiments in this thesis have been performed with single channel (Chapters 5-7) and multiple channel flow cells (Chapters 2-4). In the multiple channel flow cell multiple entrance channels converge into a larger common channel (Figure 1.6). Due to the low Reynolds number of the system the flow is laminar, which results in almost no mixing between the fluids originating from the different channels. This makes it possible to switch rapidly between different buffer conditions when using an optical trap by simply moving the sample in the orthogonal direction of the fluid flow. This enables us to trap microspheres in the first channel, catch DNA between the spheres in the second, check the integrity of the DNA in the third and perform the actual measurement (e.g. protein DNA

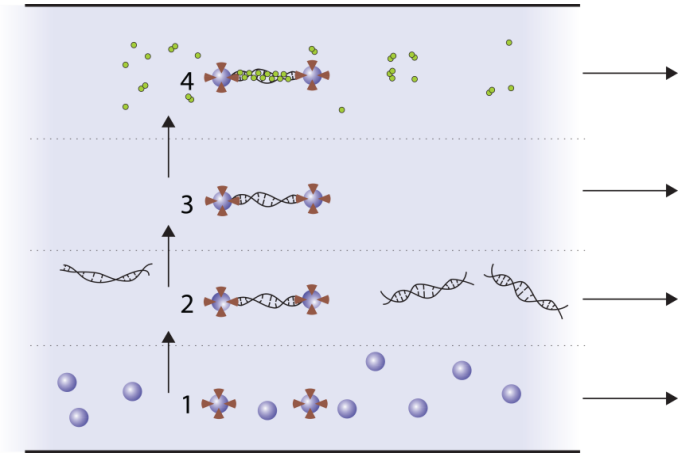

Figure 1.6 The microfluidic flow cell creates several laminar flow channels that do not mix (no physical barriers are involved). The following steps are performed to conduct a measurement: 1) catching of two microspheres; 2) attaching a DNA molecule between the microspheres; 3) checking the integrity of the DNA; 4) loading proteins on the DNA and performing a measurement.

binding experiment) in the fourth. Without microfluidics it would be extremely challenging to perform such measurements.

1.2.4 Fluorescence microscopy

DNA and proteins are two orders of magnitude smaller than the wavelength of light and have too little scattering properties in order to observe these structures with conventional optical microscopy. By using fluorescence microscopy it is possible to visualize single molecules by the use of fluorescent dyes. Fluorescent molecules are able to absorb a photon that causes the electronic configuration of the molecule to be excited from the ground to the excited state (Figure 1.7a). The excited molecule can subsequently send out a photon that has a wavelength that is slightly larger (red-shifted) than the absorbed photon. This wavelength shift occurs due to partial transfer of the absorbed photon's energy to molecular vibrations. This red-shift in the spectrum can be used to separate fluorescence from the excitation light. By fluorescently labeling the specimen of interest (DNA or proteins) it is possible to detect them although they are much smaller than the optical resolution. Two forms

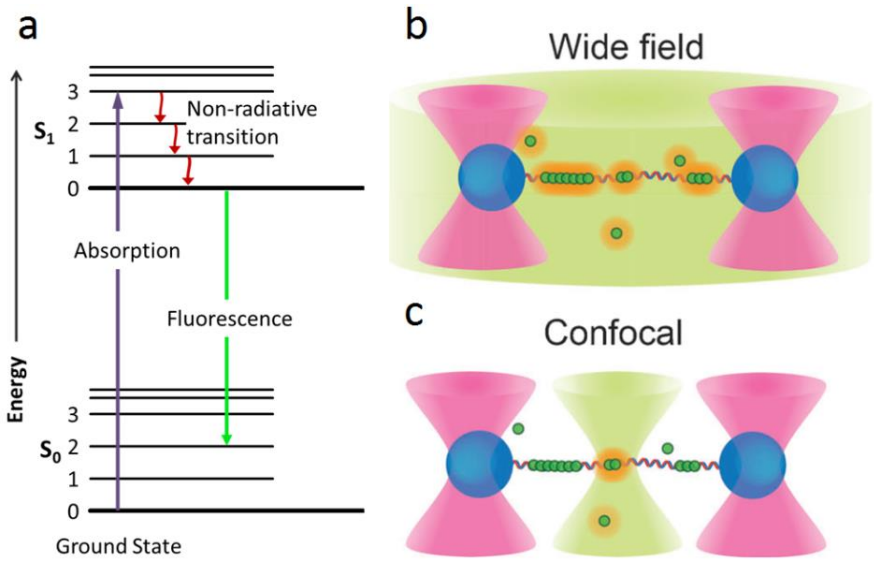

Figure 1.7 Fluorescence microscopy.(a) Energy diagram of a fluorescent molecule. An incoming photon is able to excite the molecule from the ground state to the excited state. The excited molecule will return back to the ground state by the emission of a photon (fluorescence). (b) Wide-field fluorescence microscopy combined with an optical trap. A micrometers-wide excitation beam illuminated the sample chamber. (c) Confocal fluorescence microscopy, where a focused excitation beam is placed over the sample. To acquire an image scanning of the confocal spot over the DNA is required.

of fluorescence microscopy are used in this thesis: wide field in which the whole sample is illuminated by a collimated excitation laser and confocal in which a focal excitation spot is scanned over the sample (Figure 1.7b and c). The major advantage of confocal fluorescence microscopy is that one is able to reject the out of focus fluorescence which increases the signal to noise ratio. A drawback of fluorescence microscopy is that the dyes have a finite lifetime due to photobleaching. Typical fluorophores in aqueous solution photobleach after emitting 10^5-10^6 photons[9], which is sufficient to observe a single fluorophore for hundreds to thousands of frames.

1.2.5 STED nanoscopy

Fluorescence microscopy has a resolution that is diffraction limited, which is the fundamental maximum of the resolution of an optical system due to the diffraction properties of light. This resolution (typically $\sim 250\ \mathrm{nm}$) is proportional to the numerical aperture of the objective and inversely proportional to the wavelength of the imaging light. If the spacing of two fluorescent objects (i.e. two fluorescently labelled proteins on DNA) lies below the diffraction limit, it is impossible to distinguish them. This forms a problem if one wants to distinguish individual proteins on densely coated DNA since a lot of proteins (order of a few nanometers) fit in the diffraction limit. Several techniques have been developed to overcome the diffraction limit for which the Nobel Prize in chemistry has been awarded in 2014. The super resolution method used in this thesis (Chapter 2) is pulsed Stimulated Emission Depletion (STED) confocal nanoscopy, which enhances the spatial resolution by inhibiting fluorescence emission at the periphery of the focal region. This is done by hitting excited fluorophores within a few nanoseconds with a depletion pulse which effectively forces them back to a vibrational ground state via stimulated emission. While doing so the fluorophore will emit a photon with the same wavelength as the depletion beam (Figure 1.8a). By using depletion wavelength that is red shifted compared to the wavelength of the spontaneous occurring fluorescence one can differentiate between fluorescence photons and stimulated emitted photons. To effectively enhance the resolution a specific region needs to be depleted by the STED beam after which fluorescence is detected from a region smaller than the diffraction limit (Figure 1.8b).

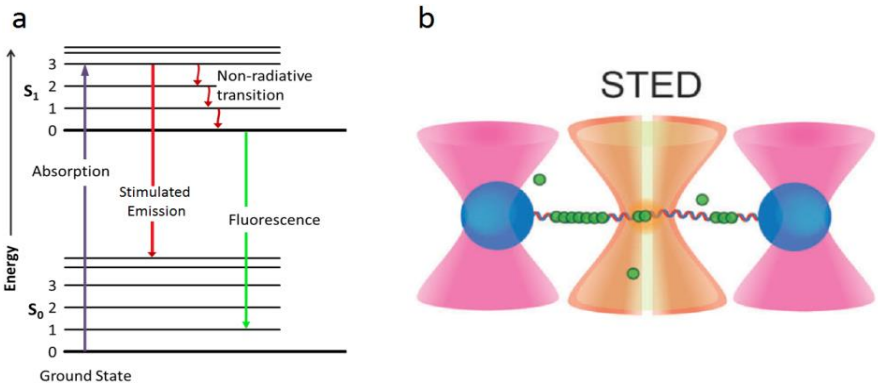

Figure 1.8 STED microscopy.(**a**) Energy diagram of a fluorescent molecule. An incoming photon is able to excite the molecule from the ground state to the excited state. The excited molecule can be forced back to the ground state via stimulated emission by a photon from a depletion beam. If stimulated emission does not occur the excited molecule will return to the ground state by emitting photon (fluorescence). (**b**) STED microscopy combined with optical an optical trap. The focal intensity distribution of the depletion beam is modified to exhibit zero intensity at the central focal point, such that fluorescence emission only takes place in this region which is smaller than the diffraction limit.

1.3 Outline of this thesis

In this thesis novel single molecule methods are described and used to obtain new insights in the physical mechanisms of various protein DNA interactions.

Chapter 2 introduces a novel method that combines optical tweezers with STED nanoscopy. This approach enables us to bridge the gap between idealized *in vitro* experiments with the *in vivo* situation. So far optical tweezers combined with fluorescence experiments were subjected to restrictive experimental conditions, such as a low protein density environment, to obtain a high enough sensitivity and resolution. Combining optical tweezers with STED nanoscopy helps us overcome these restrictions, making it possible to perform single-molecule measurements in conditions similar to those in living cells.

Chapter 3 compares different imaging techniques and parameters used to analyze the mobility of proteins on optically stretched DNA. The benefits and drawbacks of different fluorescent imaging techniques, namely wide-field, confocal and STED, are evaluated in this Chapter. Furthermore we quantified the effect of imaging conditions on the accuracy of 1D diffusion analysis using simulated data. We also consider the case of confined diffusion due to roadblocks, which is particularly interesting for DNA bound proteins. The results in this chapter form guidelines to optimize experimental conditions for the analysis of protein mobility on DNA.

Chapter 4 presents the study of the binding and bridging mechanisms of XRCC4 and XLF, two crucial proteins in the non-homologous end joining repair pathway of DNA. These measurements are performed using a dual optical trap combined with confocal fluorescence in order to measure real time binding of the proteins and a quadruple optical trap with wide-field fluorescence to measure the bridging between two different DNA molecules. We show that XLF facilitates the binding of XRCC4 and that XLF-XRCC4 complexes have the ability to form extremely stable DNA bridges. We furthermore observe that XRCC4-XLF filaments do not alter the mechanical properties of DNA and that they are highly mobile, giving us hints how XRCC4 and XLF perform their tasks on the DNA.

Chapter 5 describes a Brownian dynamics simulation of DNA tethered microspheres. In a lot of single molecule measurement techniques, such as tethered particle motion (TPM), magnetic tweezers (MT) and flow stretching (FS), DNA molecules are attached between a surface and a microsphere. The microsphere can be tracked in time and acts as a reporter for the state of the DNA.

Understanding the three dimensional motion of this microsphere is therefore of crucial importance to interpret measured data correctly. A theoretical framework that is able to describe all different techniques that use DNA tethered microspheres is therefore highly desirable. In this chapter I introduce a simulation method that is able to describe measured TPM, MT and FS data with high accuracy. This simulation program provides insights on the effect of different physical influences on the motion of tethered particles, making it a useful calibration tool for biophysicists to create a better understanding of their measured data.

Chapter 6 introduces a novel method, optical pushing, that uses a collimated beam to manipulate surface tethered microspheres. The great benefit of using a collimated laser is that it enables us to manipulate multiple microspheres that are placed in the laser beam. On the single-molecule level, discriminating heterogeneous behavior and rare events from intrinsic stochasticity requires obtaining many independent measurements. It is therefore highly desirable to manipulate and measure on multiple DNA molecules simultaneously. A drawback of this method we found is that one needs a lot of laser power to achieve a biophysical relevant force regime. This requires an expensive laser and causes unwanted heating effects in the sample.

Chapter 7 describes a novel single molecule method, acoustic force spectroscopy (AFS), that uses acoustic manipulation to perform force-spectroscopy measurements on DNA molecules. I show that this approach enables us to exert forces from sub piconewtons to hundreds of piconewtons on thousands of biomolecules in parallel, with sub millisecond response time and inherent stability. It is furthermore a simple and cheap method with a small footprint and can therefore be readily integrated in lab-on-a-chip devices. In this chapter I show a proof of principle by performing a variety of experiments using AFS, including force extension, constant-force and dynamic force spectroscopy measurements.

References

1. Bryson, B. *A short history of nearly everything*. (Transworld publishers, 2004).

2. Watson, J. D. *The double helix*. (Phoenix, 2010).

3. Smith, S., Finzi, L. & Bustamante, C. Direct mechanical measurements of the elasticity of single DNA molecules by using magnetic beads. *Science (80-.).* **258,** 1122–1126 (1992).

4. Van Mameren, J. *et al.* Unraveling the structure of DNA during overstretching by using multicolor, single-molecule fluorescence imaging. *Proc. Natl. Acad. Sci. U. S. A.* **106,** 18231–6 (2009).

5. Marko, J. F. & Siggia, E. D. Stretching DNA. *Macromolecules* **28,** 8759–8770 (1995).

6. Wang, M. D., Yin, H., Landick, R., Gelles, J. & Block, S. M. Stretching DNA with optical tweezers. *Biophys. J.* **72,** 1335–46 (1997).

7. Heller, I., Hoekstra, T. P., King, G. a, Peterman, E. J. G. & Wuite, G. J. L. Optical tweezers analysis of DNA-protein complexes. *Chem. Rev.* **114,** 3087–119 (2014).

8. Ashkin, A. Forces of a single-beam gradient laser trap on a dielectric sphere in the ray optics regime. *Biophys. J.* **61,** 569–582 (1992).

9. Kapanidis, A. N. & Weiss, S. Fluorescent probes and bioconjugation chemistries for single-molecule fluorescence analysis of biomolecules. *J. Chem. Phys.* **117,** 10953–10964 (2002).

2 STED Nanoscopy Combined with Optical Tweezers

Dense coverage of DNA by proteins is a ubiquitous feature of cellular processes such as DNA organization, replication and repair. We present a single-molecule approach capable of visualizing individual DNA-binding proteins on densely covered DNA and in presence of high protein concentrations. Our approach combines optical tweezers with multicolor confocal and STED fluorescence microscopy. Proteins on DNA are visualized at a resolution of 50 nm, a 6-fold resolution improvement over confocal microscopy. High temporal resolution (<50 ms) is ensured by fast one-dimensional beam scanning. Individual trajectories of proteins translocating on DNA can thus be distinguished and tracked with enhanced precision. We demonstrate our multimodal approach by visualizing the assembly of dense nucleoprotein filaments with unprecedented spatial resolution in real time. Experimental access to the force-dependent kinetics and motility of DNA-associating proteins at biologically relevant protein densities is essential for linking idealized in vitro experiments with the in vivo situation.

Based on: Iddo Heller, Gerrit Sitters, Onno D Broekmans, Géraldine Farge, Carolin Menges, Wolfgang Wende, Stefan W Hell, Erwin JG Peterman & Gijs JL Wuite, *Nature Methods* **10**, 910-916 (2013)

2.1 Introduction

Single-molecule studies have greatly enhanced our understanding of life at the molecular scale.[1,2] However, to obtain a high enough sensitivity and resolution for single-molecule studies, restrictive experimental conditions such as low protein density usually need to be imposed. Great challenges lie in overcoming these restrictions and performing experiments that reveal life at the single-molecule level in conditions similar to those in living cells.

Force spectroscopy[3] and fluorescence microscopy[2,4] provide access to global mechanical information and local structural information[5], respectively, of single DNA-protein complexes[6]. The combination of wide-field fluorescence microscopy and optical tweezers enables localization of labeled proteins on optically stretched DNA with sub-10 nm precision.[5,7,8] Confocal fluorescence microscopy has also been integrated with optical tweezers, which allows analyzing fluctuations in fluorescence intensity within a fixed confocal volume.[9–11] Yet, confocal imaging of optically trapped DNA remains unexploited, despite its potential to resolve local binding, activity, and motility of biomolecules on DNA at high concentrations of labeled protein in solution.

By providing nanoscale images from dense molecular environments, superresolution fluorescence microscopy has prepared the ground for carrying out single-molecule experiments at higher molecular density.[12] Stimulated emission depletion (STED)[13] confocal nanoscopy is a photon-efficient, and thus fast superresolution technique in the sense that it requires much fewer photons per unit of time to probe molecular information as compared to its spatially stochastic counterparts.[12]

Here, we present a multimodal approach designed to elucidate the dynamics and mechanochemistry of complex cellular processes at high protein concentrations in solution on densely covered DNA. To this end, we designed an instrument that combines 1) optical tweezers, to control the conformation and tension on the DNA; 2) beam-scanning confocal fluorescence microscopy, to image protein dynamics on DNA in a background of fluorescently labeled proteins; and 3) one-dimensional STED nanoscopy, to distinguish individual labeled proteins and protein filaments on densely covered DNA.

2.2 Results

2.2.1 Experimental setup

Our experimental assay is based on a bacteriophage λ DNA molecule tethered between two optically trapped microspheres (Figure 2.1a).[17] For optical trapping, two orthogonally-polarized laser beams are focused by a 1.27 NA water-immersion objective (Figure 2.1b). Force is measured on both microspheres, which allows enhancing the force resolution through differential force detection.[19] For fluorescence measurements, a pulsed laser system is used that provides both the STED and excitation pulses. A binary phaseplate[20] (PP), inserted in the path of the STED beam, enables 1D STED.[13] We used relatively large (3.2 µm diameter) microspheres to spatially separate the fluorescent labels on the DNA-protein complexes from the trapping beams. This separation prevents photobleaching due to the simultaneous presence of fluorescence excitation and trapping laser beams,[9,21] and simplifies instrument design and operation compared to the previously reported method of temporal separation[11].

2.2.2 Force spectroscopy with optical tweezers

DNA-dumbbell constructs were created *in situ* and characterized by force-distance analysis (Figure 2.2). To test the performance of force spectroscopy with large microspheres, we quantified the resolution of our optical tweezers while stretching λ DNA. The force and position fluctuations, ΔF_{rms} and Δx_{rms}, were determined for the individual microspheres in each trap (Figure 2.2, colored circles), as well as for differential detection (Figure 2.2, black diamonds).[19] The measured resolution, of order 0.1 pN or 0.2 nm, is in good agreement with the *ab initio*-calculated resolution limit set by thermal fluctuation of the dumbbell (solid curves, Appendix A). For comparison, the resolution limit for widely used 900 nm diameter microspheres is merely about twofold better (dashed curves).

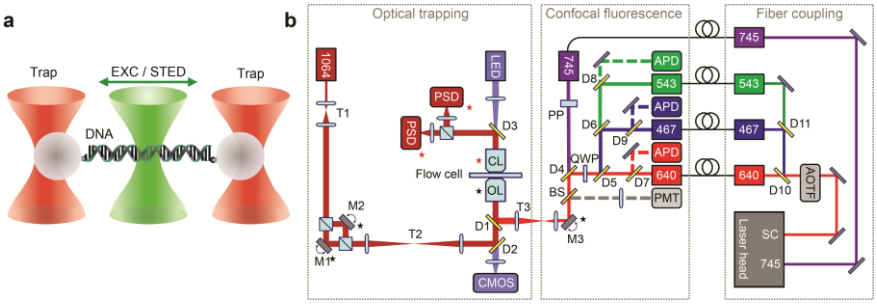

Figure 2.1 Experimental layout. (a) Schematic of the measurement assay showing two optically trapped microspheres tethered by DNA. An excitation beam (and superimposed STED beam) that is scanned over the DNA is shown in green. (b) Experimental setup showing beam paths and crucial components. Optical trapping (1064 nm, dark red): Two orthogonally polarized optical traps are independently steered using tip/tilt mirrors (M1 and M2), and microsphere displacements are measured on two position-sensitive detectors (PSDs) using back-focal plane interferometry. The microsphere-to-microsphere distance is obtained from LED-illuminated CMOS camera images (875 nm, blue). Fluorescence: One laser system supplies STED (745 nm, purple) and excitation beams (640 nm, 543 nm, and 467 nm, respectively red, green, and dark blue, filtered from a supercontinuum spectrum (SC) using an acousto-optical tunable filter (AOTF)). These beams are fiber coupled and delivered to the confocal tip/tilt piezo mirror scanner (M3) after being combined by dichroics (yellow). The descanned fluorescence signal (dashed lines) is collected on fiber-coupled APDs, while descanned excitation light can optionally be detected using a photomultiplier tube (PMT) by placing a pellicle beamsplitter (BS, orange) in the common path. A STED stripe is formed by a binary phaseplate (PP), and optionally the excitation beams can be cirularly polarized using a λ/4 retarder (QWP). Black and red stars indicate planes conjugate to the objective and condensor back-focal plane, respectively. CL, condensor lens; D1-11, dichroic mirrors; OL, water-immersion objective lens; T1-T3, telescopes.

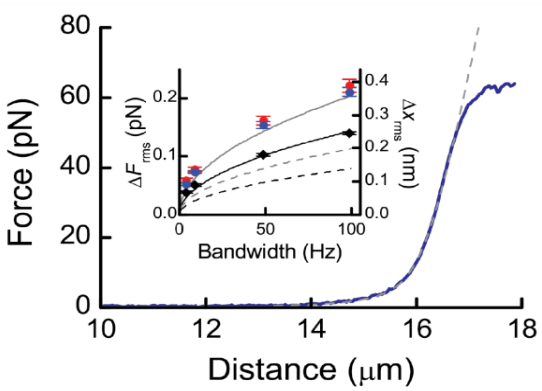

Figure 2.2 Experimental force-distance curve of λ DNA in PBS. The dashed curve shows the extendible worm-like-chain model calculated using a persistence length of 55 nm, a contour length of 16.5 μm, and a stretching modulus of 1350 pN. DNA overstretching occurs near 65 pN. The inset shows the measured (symbols) and calculated (curves) force and position noise as function of measurement bandwidth (average trap stiffness 0.57 pN/nm, F = 25 pN). Red, blue and grey, noise for single-bead detection; Black, noise for differential detection; Solid curves, 3.2 μm diameter microspheres; Dashed curves, 0.9 μm diameter microspheres.

2.2.3 Multicolor confocal imaging and background rejection

To demonstrate the confocal imaging capabilities of our instrument and confirm single-fluorophore sensitivity, we imaged a range of (individual) fluorescent dyes on DNA (Figure 2.3a-e, typical acquisition time ~1 Hz, see also single-step photobleaching traces in Supplementary Figure 2.1). Simultaneous multicolor imaging enables more complex, multicomponent biomolecular studies (Figure 2.3e). Importantly, no elevated photobleaching rate was observed near the optically trapped microspheres during confocal imaging (Figure 2.3a-e).

To qualitatively test background rejection in our confocal imaging layout, we imaged Atto647N-labeled proteins on DNA in the absence (Figure 2.3f) and presence (Figure 2.3g) of free dye in solution (~40 nM Atto647N-NHS). At 1 ms integration time, we estimate the upper limit of background concentration for

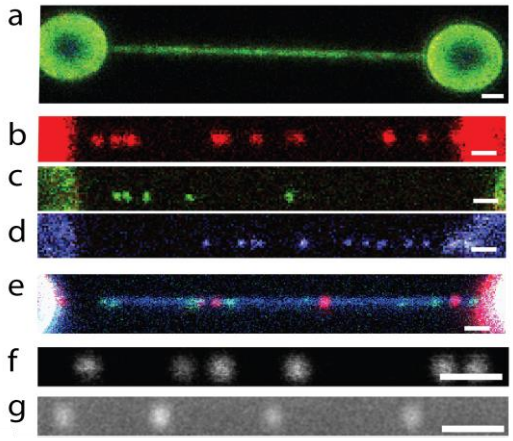

Figure 2.3 Confocal fluorescence microscopy. (**a**) Confocal microscopy image of Sytox Orange labeled λ DNA between two 3.2 µm microspheres (exc 543 nm). (**b-d**) Confocal microscopy images of individual EcoRV-Atto647N (**b**, exc 640 nm), Sytox Orange dyes (**c**, exc 543 nm), and EGFP-labeled proteins (**d**, exc 467 nm). (**e**) Simultaneous multicolor imaging of Sytox Orange, Sytox Blue, and BsoBI-Atto647N. (**f**,**g**) Confocal microscopy images of individual BsoBI-Atto647N restriction enzymes bound specifically to optically stretched λ DNA in the absence (**f**), and presence (**g**) of 100 nM of free Atto647N-NHS (the local concentration in the flow cell is estimated to be lower due to adsorption, approximately 40 nM). All scale bars 1 µm. Typical frame rate for a 25 µm x 2 µm field of view using 100 µs dwell time per 75 nm pixel is 1 Hz.

which we obtain single-molecule sensitivity to be about 100 nM, which is approximately 1 to 2 orders of magnitude higher than the typical limit for wide-field imaging.

2.2.4 STED nanoscopy of proteins on DNA

We employed STED to perform sub-diffraction imaging in optical tweezers. STED allows fast imaging on DNA at a rate that is ultimately limited by the scanning speed and the rate of fluorescence emission. For STED, we use a focal intensity distribution that features a one-dimensional central line of nearly zero intensity (cf.

Figure 2.4a-d, Appendix A)[20], rather than a central zero point of a doughnut-shaped distribution[22]. By orienting the zero-line perpendicular to the stretched DNA, the spatial resolution is enhanced along the length of the DNA only. Importantly, this 1D-STED scheme renders 1D-line scanning far less sensitive to lateral DNA fluctuations, misalignment, or drift between the optical trapping and fluorescence imaging systems than a doughnut.

A comparison of confocal and STED images of Atto647N-labeled restriction enzymes specifically bound to optically stretched DNA demonstrates the clear resolution enhancement along the DNA that is provided by STED imaging (cf. Figure 2.4e and f and the intensity profiles in Figure 2.4g). Notably, no significant additional DNA photo nicking was observed during STED imaging (Appendix A).

Next, we demonstrate the importance of precise control of tension on the DNA to achieve high resolution imaging. Thermal fluctuations of suspended DNA will blur the images taken of DNA-bound proteins.[5] However, the amplitude of such fluctuations can be reduced by applying tension to the DNA using optical tweezers. The inset of Figure 2.4h strikingly illustrates that reducing the DNA tension from 30 pN down to 0.4 pN completely abolishes the ability of STED nanoscopy to resolve two DNA-bound proteins in close proximity. We measured the FWHM of STED images of single fluorophores as function of applied force (Figure 2.4h, symbols), revealing a loss of effective resolution at forces below ~5 pN. Our data is well-described by a model (Figure 2.4h, black line) that convolves the optical resolution with estimated longitudinal DNA fluctuations (dashed line, Appendix A).

The scaling of resolution with STED power was further characterized by imaging restriction enzymes on optically stretched DNA (Figure 2.4g). At P_{STED} = 26 mW, we obtained a resolution of 50 +/- 5 nm (s.e.m.) full-width at half maximum (FWHM), corresponding to a 6-fold resolution enhancement over confocal imaging under the same conditions (given by the water immersion lens and the aqueous medium).

The scaling of resolution with P_{STED} is well described by taking into account the blurring due to thermal fluctuation of the DNA (solid line Figure 2.4g, Appendix A, and Supplementary Figure 2.2). Most notably, the gain in resolution allows imaging DNA-protein complexes in optical tweezers at a resolution comparable to the persistence length of DNA.

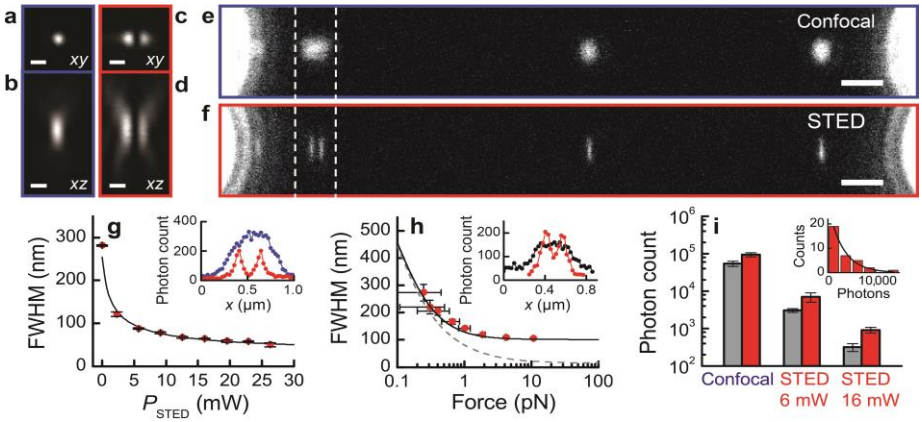

Figure 2.4 Characterization of STED nanoscopy of proteins on optically stretched DNA. (**a-d**) Focal intensity distributions of the 640 nm excitation (**a**,**b**) and 745 nm STED beam (**c**,**d**) imaged in xy (**a**,**c**) and xz (**b**,**d**) (scale bars 500 nm). (**e**,**f**) Confocal microscopy (**e**) and subsequent STED image (**f**, P_{STED} = 6 mW) of EcoRV-Atto647N on λ DNA (scale bars 1 µm). (The ellipticity of intensity distributions in **e** is likely due to linear polarization of the excitation light, to lateral DNA fluctuations,[5] or to aberrations associated with residual tilt of the cover glass with respect to the water-immersion lens.) (**g**,**h**) Scaling of effective resolution with P_{STED} (**g**, F = 4 pN) and with force (**h**, P_{STED} = 4 mW), showing the average FWHM (<n> = 9.7) of Gaussian fits to intensity profiles obtained from BsoBI-Atto647N and EcoRV-Atto647N on DNA (vertical error bars, s.e.m.; horizontal error bars **h**, s.e. = 0.2 pN). Solid lines, fits to data; dashed line, amplitude of longitudinal DNA fluctuations (Appendix A). The insets show projected intensity profiles of Atto647N-labeled enzymes on DNA, for the DNA section as indicated by the dashed lines in **e** (**g**, blue) and **f** (**g**, red), and for P_{STED} = 4 mW at 0.4 pN (**f**, black) and 30 pN (**f**, red) tension. (**i**) Average number of photons detected from individual fluorophores before photobleaching (s.e.m., <n> = 43) obtained from exponential fits of photon-count distributions as in inset, for TRIS (grey) and ROXS (red) buffers at P_{STED} 0 mW, 6 mW, and 16 mW.

To characterize photobleaching, we counted the number of photons collected from individual Atto647N fluorophores on optically stretched DNA before bleaching (Figure 2.4i). For confocal imaging in Tris buffer, about 55,000 photons could be

collected. For STED imaging, however, about one and two orders of magnitude fewer photons were collected for P_{STED} = 6 mW (87 nm FWHM) and P_{STED} = 16 mW (64 nm FWHM), respectively, which is comparable to the signal reduction that is also observed under two-photon excitation.[23] We note that in our case, some of the photobleaching may also be due to the fact that in our high NA water immersion system, the STED focal intensity was not perfectly zero at the minimum, which starts playing a role at higher STED powers. Nevertheless, it is important to note that the 500 to 5,000 photons collected per fluorophore (at 64 nm FWHM and 87 nm FWHM, respectively) are sufficient for imaging up to 50 to 500 frames, allowing nanoscale observation of protein dynamics over extended periods of time (see below). By using anti-bleaching buffer ROXS (Appendix A and Supplementary Figure 2,3), the number of collected photons can be increased about 2-3-fold (ie. to ~1,000 photons at 64 nm FWHM, cf. Figure 2.4i).

Next we explored the localization precision of proteins for confocal and STED imaging by acquiring kymographs of immobilized restriction enzymes on DNA (Figure 2.5a). For comparison, we also imaged a protein that undergoes 1D diffusion on DNA (Figure 2.5b). The positions of the proteins were tracked by fitting a 1D Gaussian function to each line scan. We calculated the power spectral density (PSD) of the fluctuations in the tracked position of proteins on DNA (Figure 2.5c). Whereas a diffusing protein exhibits a power spectrum with $1/f^2$-frequency dependence (squares), which is characteristic for free diffusion, immobilized proteins exhibit a frequency-independent power spectrum (circles). The latter power spectra represent the experimental noise floor for particle tracking. Strikingly, 1D-STED imaging provides an enhanced localization precision (i.e. lower noise floor, cf. closed circles) compared to confocal imaging (open circles), enabling observation of protein translocation at higher spatial or temporal resolution.

To further quantify the localization precision, we plot the root-mean-square fluctuations of the tracked position, Δx_{rms}, for immobilized enzymes as function of P_{STED} in Figure 2.5d (circles). A near twofold enhancement of the localization precision of STED over confocal microscopy is observed, saturating at ~6 nm for high P_{STED}. Analysis of the measured localization precision provides information on the stability and reliability of STED imaging on optically stretched DNA. In Figure 2.5d, the solid curve represents the "ideal" localization precision, neglecting DNA fluctuations, which is solely governed by photon-counting noise, pixilation noise, and background noise (Appendix A).[24] Strikingly, the ideal localization precision is only ~2 nm better than the measured localization precision. This illustrates that

STED superresolution imaging on optically manipulated DNA is highly reliable and stable. The additional experimental noise may include contributions from slow thermal fluctuations of the dumbbell construct, from drift and fluctuations between the separate optical trapping and confocal imaging systems, and from the line-to-line repeatability of the confocal beam scanner. Furthermore, the observed saturation of localization precision at high P_{STED} implies sub-optimal tracking, which can be due to a reduced maximum fluorescence emission rate from the non-zero intensity of the focal STED beam. Figure 2.5d also indicates the calculated optimal localization precision (dashed curve) when there is no loss in peak brightness of the fluorophores with increasing STED power. In the optimal 1D-STED case, the photon-counting noise scales as $\sqrt{FWHM}$. Intriguingly, the enhanced photon yield by ROXS should be sufficient to obtain single basepair localization precision in this optimal case (i.e. by collecting 10,000 photons at P_{STED} = 6 mW).

Finally, we demonstrate that also double-stranded DNA can be imaged with sub-diffraction resolution using STED.[25] In the kymograph of Figure 2.6a, which was acquired sequentially by confocal and STED microscopy, binding of individual Sytox Red dyes to DNA can be observed. The intensity profiles of Figure 2.6b show a resolution enhancement of a factor of 4 over confocal microscopy.

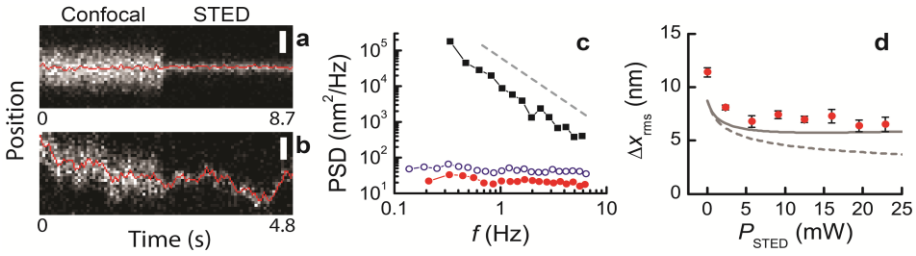

Figure 2.5 Characterization of localization precision. (**a**,**b**) Kymographs of Atto647N-labeled proteins on optically stretched DNA, imaged partially by confocal microscopy and partially by STED nanoscopy (P_{STED} = 6 mW), for immobilized EcoRV-Atto647N (**a**) and for diffusing TFAM-Atto647N (**b**) (scale bars 200 nm). Red lines track the centers of the photon distributions and were obtained by fitting 1D Gaussians to each pixel column. (**c**) Power-spectral density (PSD) for tracked positions of proteins on DNA. Black squares, PSD for a single diffusing TFAM-Atto647N; Dashed line, $1/f^2$ behavior; Circles, averaged PSDs for immobilized BsoBI-Atto647N for confocal imaging (open blue circles, n = 6) and STED imaging (filled red circles, n = 10). (**d**) Localization precision Δx_{rms} as function of P_{STED} (F = 4 pN). Red symbols, localization precision as obtained from tracking immobilized proteins on DNA (s.e.m., <n> = 10.9); Solid curve, ideal localization precision that neglects DNA fluctuations; Dashed curve, optimal ideal localization precision that assumes no loss in peak brightness of the fluorophores with increasing STED power (Appendix A).

2.2.5 Imaging protein dynamics at high protein density

Now we demonstrate our multimodal approach by studying the DNA binding dynamics of the human mitochondrial transcription factor TFAM,[26,27] labeled with Atto647N (Figure 2.7). In contrast to earlier wide-field microscopy recordings,[28] confocal microscopy allows real-time observation of individual TFAM-Atto647N binding to DNA in a solution containing up to ~100 nM TFAM-Atto647N. Indeed, we observed binding followed by diffusion of TFAM-Atto647N on stretched DNA (Figure 2.7a, TFAM-Atto647N concentration ~5 nM). The initial TFAM intensity distribution, measured immediately after binding, peaks at 1 fluorophore (Figure 2.7c, blue bars). This is consistent with previous findings that TFAM primarily binds

DNA as monomer[28] (a labeling ratio below unity, however, prevents us from extensive interpretation of the fluorescence intensity).

In vivo, the abundance of TFAM in mitochondria is large enough to coat the entire mitochondrial genome and form filaments on DNA. We intended to mimic this regime *in vitro* by studying TFAM-coated DNA at high TFAM concentration. However, confocal microscopy cannot resolve individual protein trajectories at high protein densities (Figure 2.7a, right-hand side). Using STED, we observed many TFAM-Atto647N molecules diffusing on DNA (Figure 2.7b, 75 nm FWHM, line rate 18 Hz). The advantage of STED over confocal imaging can be readily appreciated in this high-protein-density regime. STED allows observation of individual protein (filament) trajectories along the DNA at sub-diffraction resolution. Bright regions that might be misinterpreted as stable filaments in confocal microscopy, are identified by STED to consist of individual TFAM-Atto647N proteins or filaments that diffuse rapidly within diffraction-limited regions (Figure 2.7b, arrows). In addition, STED nanoscopy over periods > 20 s clearly reveals that TFAM molecules oligomerize after collision with other TFAM molecules as reported before[28]. Although the imaging resolution in this experiment is insufficient to distinguish adjacent proteins within an oligomer (~10 nm separation), repeated imaging reveals whether proteins were in mere coincidental proximity, or were in fact diffusing colocalized in an oligomer over an extended period of time. Notably, such oligomers can occasionally break up again (Figure 2.7b, asterisks). In Supplementary Figure 2.4, we exploited the maximum STED resolution to image TFAM on DNA at even higher density.

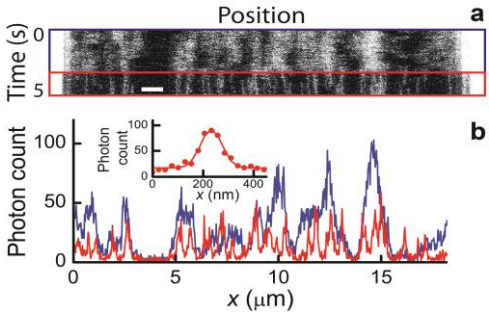

Figure 2.6 STED nanoscopy of Sytox Red on optically stretched DNA. (**a**) Kymograph showing Sytox Red dyes binding to double-stranded λ DNA (Scale bar 1 μm). The top half (blue) was acquired by confocal microscopy whereas the bottom half (red) was recorded using STED nanoscopy (P_{STED} = 6 mW). (**b**) Intensity profiles obtained from the confocal (blue) and STED (red) imaging section of **a**. The inset shows the intensity profile of an individual Sytox Red dye bound to DNA. A Gaussian fit (line) yields a FWHM of 99 nm.

Furthermore, STED allows individual proteins to be tracked at high density with less ambiguity, providing higher particle number statistics, and allowing studies of diffusive behavior on crowded DNA. We performed mean-square-displacement (MSD) analysis of individual TFAM-Atto647N trajectories on DNA in order to estimate the diffusion constants, D (Figure 2.7d). Interestingly, we find a mean diffusion constant of 0.028 +/- 0.004 $\mu m^2/s$ (s.e.m., n = 143), which is much slower than the diffusion constant measured previously for TFAM monomers that diffuse on very sparsely covered DNA,[28] $D_{ref} \approx 0.08\ \mu m^2/s$. This finding suggests that at the high TFAM density used here, TFAM oligomerization occurs, which can reduce D. One such oligomerization event is shown in Figure 2.7e. Indeed, the slope of the MSD versus time curve is reduced by ~50% after oligomerization (Figure 2.7f). The expected distribution of D for a single population of TFAM monomers with $D = D_{ref}$ (Figure 2.7d, dashed line), calculated using simulated diffusion data (Appendix A), fails to describe the measured data. Instead, a simulation that assumes a mix of oligomers having different diffusion constants (Figure 2.7d, solid line, Appendix A) is in good agreement with the measured diffusion data.

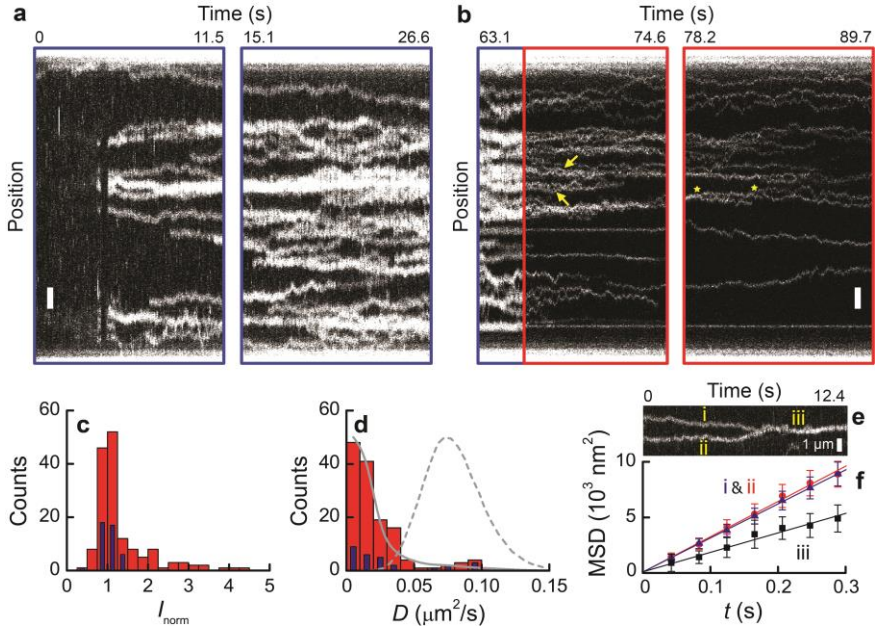

Figure 2.7 TFAM binding and diffusion dynamics on optically stretched DNA. (**a**,**b**) Kymographs of TFAM-Atto647N dynamics on λ DNA (F = 4 pN, scale bars 1 μm). In **a**, the DNA is moved into a channel with 50 nM human TFAM-Atto647N (estimated concentration is lower due to adsorption, ~5 nM) and imaged using confocal microscopy. In **b**, the DNA is in ROXS buffer and at t = ~66 s, the STED beam is switched on at 6 mW (red borders). Imaging in **a** and **b** was performed at 10 μs per 25 nm pixel, line rate 90 Hz, 5-line averages are displayed. (**c**,**d**) Histograms of the intensity of TFAM-Atto647N on DNA normalized to the number of fluorophores, I_{norm}, (**c**) and of the diffusion coefficient, D, (**d**), obtained both by STED and confocal imaging. Blue bars, TFAM immediately after binding DNA (n = 42); Red bars, the full dataset (n = 143), including already bound TFAM and TFAM filaments. D was calculated by fitting the mean-squared-displacement (MSD) determined from individual traces (<lines> = 150 +/- 75 (s.d.), with a minimum of 50 lines) to MSD = 2Dt + offset. Grey curves, normalized distributions of D for simulated diffusion data (Appendix A) with D_{ref} = 0.08 $\mu m^2/s$ (dashed) and with a range of diffusion constants D = D_{ref}/N_{TFAM} where N_{TFAM} = 1,2,3,…,12 (solid, Appendix A). (**e**) Kymograph of a TFAM-Atto647N oligomerization event (line rate 122 Hz, 5-line average displayed). (**f**) MSD analysis of trajectories i-iii as indicated in **e** (s.d., <lines> = 130).

2.3 Discussion and conclusion

We introduced a new multimodal approach that combines optical tweezers with confocal and STED microscopy. Confocal microscopy allows imaging of single DNA-bound proteins on optically stretched DNA at up to two orders of magnitude higher background concentrations than wide-field microscopy. A time resolution comparable to typical wide-field imaging is ensured by fast confocal line scanning along DNA that is linearized by optical tweezers. This allows new experiments at biologically relevant protein concentrations where protein binding and dynamics can be spatially resolved in real-time at high time resolution of 50 ms (up to 5 ms). Multicolor imaging enables more complex studies of multicomponent biomolecular systems.

The addition of superresolution imaging provides a drastic (6-fold) resolution enhancement over confocal imaging, granting unique access to more physiologically compatible conditions, in which DNA is densely coated with proteins. A spatial resolution of 50 nm has been demonstrated, which compares directly to biologically interesting length scales such as the persistence length of double-stranded DNA, the length of eukaryotic Okazaki fragments, and typical nucleosome-nucleosome spacings in a beads-on-a-string configuration. Importantly, the time resolution of confocal imaging is not compromised by STED. In fact, the time resolution of localization and tracking is enhanced, due to better localization accuracy. STED thus allows observation of rapid dynamics with sub-diffraction resolution. As an alternative to STED, stochastic superresolution techniques based on single-molecule on/off switching are optically less complex and can readily be integrated with wide-field fluorescence on optically stretched DNA.[30] These techniques, however, are currently slower than STED, because larger numbers of detected photons are needed to localize the position of the molecules and to construct images.

Finally, our approach uniquely combines STED and optical tweezers. The optical tweezers allow precise control of DNA location and tension, which is crucial to suppress thermal fluctuations that can inhibit sub-diffraction imaging. In addition, the 1D-STED scheme prevents problems associated with lateral DNA fluctuations. Our characterization of the effective imaging resolution as a function of DNA tension outlines the conditions required for nanoscale imaging of proteins bound to suspended DNA. Quantifying these conditions is highly relevant for superresolution imaging of DNA manipulated by techniques that do not have obvious force-

measuring capabilities (ie. flow-stretched DNA, DNA curtains or DNA confined in nanochannels). Furthermore, optical tweezers are uniquely complemented by STED to enable nanoscale visualization of the force-dependent behavior of DNA-protein interactions. Access to the force dependence of kinetics and motility thus allows unraveling the mechanochemistry of DNA-protein interactions at the nanometer length scale and under biologically relevant conditions. We anticipate that our combined force-superresolution approach can be readily extended to other one-dimensional systems such as (trains of) molecular motors on the cytoskeleton as well as superresolution imaging on optically manipulated cells or cellular components. Moreover, experimental access to real-time information on kinetics and motility of DNA-bound proteins at biologically relevant protein concentrations is essential for linking idealized *in vitro* experiments with the *in vivo* situation, where DNA is densely coated with proteins.

Appendix A: Additional information

DNA and proteins. DNA-dumbbell constructs are created from bacteriophage λ DNA, biotinylated as described previously.[31] Streptavidin-coated microspheres (3.2 μm diameter, Spherotech. Inc.) were coupled to the λ DNA *in situ*.[31]

The restriction enzymes were labeled as described previously.[32] DNA-protein complexes were obtained by pre-incubating 10 nM BsoBI-Atto647N or EcoRV-Atto647N with biotinylated λ DNA in a buffer containing 0.5 mM EDTA, 10 mM $CaCl_2$, 20 mM Tris at pH 7.6, and 100 mM NaCl. A ROXS buffer containing 2 mM trolox, 1 mM methyl viologen, and enzymatic oxygen removal using 0.43 mg/ml glucose oxidase, 72 μg/ml catalase, and 4.5 mg/ml D-glucose was used to study bleaching.

TFAM was expressed, purified and fluorescently labeled with Atto647N dye as described previously.[28] The labeling ratio was approximately 1 fluorophore per 2 TFAM molecules. Real-time binding was studied in buffer consisting of 10 mM Tris HCl pH 7.6, 25 mM NaCl, 5 mM DTT, and 50 mM TFAM-Atto647N.

Finally, Sytox Blue, Sytox Orange, and Sytox Red were obtained from Invitrogen. For high coverage, 1-10 nM Sytox Blue and Sytox Orange were used, whereas individual dyes were imaged in presence of trace levels of Sytox Orange (~100 pM). Sytox Red was imaged at ~10 nM.

Microscope and microfluidics. The experiments were performed on a custom-built inverted microscope based on a water-immersion objective (CFI Plan Apo IR 60X WI, Nikon, NA 1.27) placed on a vertical stage MVN80 (Newport Corporation) using a custom-built adapter. A 5-channel laminar flow cell (Micronit Microfluidics BV) was mounted on an automated XY-stage (MS-2000, Applied Scientific Instrumentation), which allowed rapid, *in situ* construction and characterization of dumbbell constructs (typically, a construct is created in less than one minute), and facilitated swift and complete transfer of the tethered DNA between different flow channels (allowing force spectroscopy and visualization experiments to be performed on > 20 DNA molecules per hour).[17] A condenser toplens (P 1.40 OIL S1 11551004, Leica) is placed on top of the flow cell. The flow cell and microspheres are illuminated by an 875 nm LED (LED-1115-ELC-875-19-5, IMM Photonics), and imaged in transmission onto a CMOS camera (DCC1545M, Thorlabs).

Optical trapping. Optical trapping is performed using a 10 W CW fiber laser (YLR-10-LP, 1064 nm, IPG Photonics) with coupled optical isolator. The laser beam is expanded using lenses with focal lengths of 75 mm and 150 mm. Here, the 75 mm lens is placed on an automated linear stage (AG-LS25, Newport) to modify the collimation for aligning the optically stretched DNA with the focal plane of the confocal imaging system. Two polarizing beam-splitter cubes (10BC16PC.9, Newport) are used to split the 1064 nm laser into two independently steerable optical traps and recombine these. One coarse positioning piezo stepper mirror (AG-M100N, Newport), and one accurate piezo mirror (Nano-MTA2X Aluminium, Mad City Labs) is used for beam steering the two traps. Two 300 mm lenses couple the trapping beams into the objective. The displacements of the trapped microspheres from the center of the trap are measured and converted into a force signal. Force measurements are performed by back-focal plane interferometry[18] of the condensor lens using two position sensitive detectors (DL100-7PCBA3, Pacific Silicon Sensor) after separating the two polarized beams using a polarizing beam-splitter cube. Two dichroic mirrors (950DCSP, Chroma Technology Corporation) separate the trapping light from the LED illumination before and after the flowcell. We use approximately 1 W per trap, which, for 3.2 µm microspheres, yields a trap stiffness of roughly 0.5 pN/nm and allows forces up to 500 pN to be applied.

Confocal and STED fluorescence microscopy. A single laser system (ALP-710-745-SC, Fianium Ltd, Southampton, UK) is used for fluorescence excitation and STED. This turn-key system simplifies the implementation of STED and provides flexibility in excitation wavelength. Moreover, this system allows dual color STED (STED wavelengths 711 nm and 745 nm compatible with for example Atto590 and Atto647N) as detailed in ref. [33] In this study we have only used the 745 nm beam for single-color STED. We select three excitation bands (centered at 467 nm, 543 nm, and 640 nm, compatible with a range of conventional fluorescent dyes) from a supercontinuum spectrum. After polarizing (Glan-Thompson prism PGT 1.08.05, Bernhard Halle Nachfl. GmbH) and filtering the supercontinuum spectrum using an AOTF (AOTFnc-VIS-TN, AA Opto-Electronic) the three beams are separated and filtered using appropriate dichroic mirrors (F43-088 and F43-093, AHF Analysentechnik GmbH) and filters (F94-640, F94-543, and F34-467, AHF). The three excitation beams and the STED beam are coupled into single-mode fibers (PMC-640 and PMC-460, Schafter & Kirchoff GmbH) using laser beam couplers (60SMS-1-4-M15-26 and 60SMS-1-4-M15-37, Schafter & Kirchoff), and subsequently collimated again (collimator 60FC-L-4-M20L-02, Schafter & Kirchoff or f = 20mm achromats G052006000, Qioptiq) to yield beams of 3.6 mm diameter. Fine adjustment of the

polarization angle of the 745 nm beam before fiber coupling is done using an achromatic λ/2 retarder (RAC 4.2.10 L, Bernhard Halle). The four beams are combined using dichroic mirrors (F48-533, F33-632, and F73-726, AHF). Beam scanning using a fast tip/tilt piezo mirror (S-334.1SD, Physik Instrumente GmbH & Co, scan rate up to 200 Hz)) is followed by 1:3 beam expansion and combining with the trapping laser using a dichroic mirror (F43-800, AHF). After beam expansion, the excitation and STED beams (10.8 mm diameter) overfill the back aperture of the objective (8.5 mm diameter). All (dichroic) mirrors that encounter the STED beam are at least 6 mm thick and have flatness better than λ/10. The STED beam is centered on a custom-made binary phaseplate consisting of a flat glass window that features a MgF_2-layer (approximately 1 μm thick) deposited onto a section of the phase plate in order to provide a 180° phase step to half of the STED beam.[20] In the sample, the resulting focal intensity distribution ideally exhibits a line of zero intensity at the center of the focus such that saturated stimulated emission only occurs in the high-intensity periphery of the STED beam.[13] This 1D-STED scheme can be readily adapted to 2D STED[22] by, for example, replacing the binary phaseplate with a helical phaseplate and inserting a λ/4 retarder between the phaseplate and objective to establish circular polarization. Further modification including a second phaseplate[13] can also enable 3D STED. For confocal microscopy, the excitation beams can be circularly polarized using a λ/4 retarder (RAC 4.4.10, Schafter & Kirchoff). For confocal detection, the emitted fluorescence is descanned, separated from the excitation by dichroic mirrors (F48-640, F33-554, and F38-484, AHF), filtered using appropriate emission filters (F42-652&F47-686, F47-586, and F37-510, AHF) and photons are counted using fiber-coupled APDs (APDs SPCM-AQRH-14-FC, fibers SPCM-QC9, Perkin Elmer). The multimode fibers serve as confocal pinholes (100 μm diameter) that provide background rejection, thus increasing the signal-to-background ratio such that single fluorophores can still be resolved on the DNA even when high concentrations of labeled proteins are present in solution. Because the confocal pinhole size is large (~1.75 Airy disks), the expected confocal imaging resolution is set by the focal intensity distribution of the excitation beam. To block the STED beam from the detection paths, a multiphoton emission filter (F75-750, AHF) is used.

Hardware control and data acquisition. For force detection, we sample the output voltages of the PSDs at 50 kHz using a data acquisition card (NI PCI-4472B, National Instruments). Photon counting, beam steering, and digital I/O is performed using a multifunction card (NI PCIe-6323, National Instruments). All optical trapping, force detection, and confocal fluorescence and STED hardware is controlled using custom

software, written in LabVIEW 2010 (National Instruments), and standard calibration, dumbbell-construction, mechanical characterization, and visualization procedures are largely automated. Through its clean, user-friendly interface, which can be controlled with a gaming joystick (Logitech), the LabVIEW software allows for automation of many of the complex experimental procedures. A hardware abstraction layer and a plug-in system enable the same software to run on a range of instruments in our lab.

Optical tweezers resolution. To calculate the force noise, $\sqrt{\langle \delta F^2 \rangle}$, we use the expressions derived previously in ref. [19] for the signal-to-noise ratio, $SNR = \langle \Delta x \rangle / \sqrt{\langle \delta x^2 \rangle} = \langle \Delta F \rangle / \sqrt{\langle \delta F^2 \rangle}$ (we used eq. 3 of ref. [19] for force detection on a single bead, and eq. 8 in ref. [19] for the case of differential force detection). Here, $\langle \Delta F \rangle$ represents a change in force due to a small change in DNA contour length, ΔL, such that $\langle \Delta F \rangle = \Delta L \, k_{\mathrm{trap}} k_{\mathrm{DNA}} / \left(k_{\mathrm{trap}} + 2k_{\mathrm{DNA}} \right)$, where k_{DNA} is the force-dependent stiffness of the DNA, and we assume that the two traps have equal trap stiffness, k_{trap}.

Focal intensity distribution imaging. To facilitate straightforward alignment and optimization, a photomultiplier tube (PMT) was used to directly image the focal intensity distribution of the excitation and STED beams. A 50:50 pellicle beamsplitter (BP145B1, Thorlabs) is placed in the beam path, and light, scattered by Au microspheres scanned through the focus using a piezo stage (NanoLP200, Mad City Labs), is detected using a PMT (MD 963 CPM DC, Perkin Elmer). Here, 80 nm Au nanoparticles (EM.GC80/4, British Biocell International) were first mounted in a 2 % (w/w) agarose gel to avoid imaging near to the glass-liquid interface where reflections swamp the signal from the Au nanoparticles.

Longitudinal DNA fluctuations. The amplitude of the longitudinal DNA fluctuations was calculated assuming equipartition of energy as $\langle {\sigma_{\mathrm{DNA}}}^2 \rangle = k_B T / K_{\parallel}(x)$. Here,

$$K_{\parallel}(x) = \left(\frac{x}{L k_{\mathrm{DNA}}} + \frac{1}{k_{\mathrm{trap}}} \right)^{-1} + \left(\frac{L - x}{L k_{\mathrm{DNA}}} + \frac{1}{k_{\mathrm{trap}}} \right)^{-1} \qquad \text{Equation 2.1}$$

represents the longitudinal stiffness (ie. in the direction parallel to the DNA axis) experienced at a point x along a DNA molecule that is stretched to end-to-end length L. The extendible worm-like-chain model was used to approximate the tension-dependent spring constant of a section of the DNA, $k_{\mathrm{DNA}} = \partial F / \partial L$. For analysis of experimental data on BsoBI, we averaged the amplitude of the longitudinal fluctuations over the restriction sites of BsoBI on lambda DNA.

Spatial imaging resolution. The spatial resolution of STED is given by

$$FWHM_{\mathrm{STED}} = \frac{\lambda}{2NA\sqrt{1+\frac{P_{\mathrm{STED}}}{P_S}}} \qquad \text{Equation 2.2}$$

where λ is the excitation wavelength and P_S is the STED power that corresponds to the saturation intensity of the fluorophore at the applied STED wavelength.[12] Longitudinal DNA fluctuations blur the image of DNA-bound proteins such that $FWHM_{\mathrm{meas}} = \sqrt{(FWHM_{\mathrm{STED}})^2 + (FWHM_{\mathrm{DNA}})^2}$. Figure 2.4g shows a fit of $FWHM_{\mathrm{meas}}$ to experimental data, using P_S as a fit parameter and assuming $FWHM_{\mathrm{DNA}} = 2\sqrt{2\ln 2}\sigma_{\mathrm{DNA}} \approx 31\ \mathrm{nm}$ at 4 pN tension. Supplementary Figure 2.2 highlights the relative contribution of longitudinal DNA fluctuations for the fit of $FWHM_{\mathrm{meas}}$.

Localization precision. The ideal localization precision is defined as: $\langle(\Delta x)^2\rangle = s^2/N + a^2/12N + 4\sqrt{\pi}s^3b^2/aN^2$, where the three right-hand side terms represent the mean-squared position fluctuations due to photon-counting noise, pixilation noise, and background noise, and *s*, *a*, *b*, and *N*, are the standard deviation of the effective focal intensity distribution, the pixel size, the background noise, and the number of photons, respectively.[24] To calculate the ideal localization precision for Figure 2.5d (solid curve), we estimated *s* using

$$s = \frac{FWHM_{\mathrm{STED}}}{2\sqrt{2\ln 2}} = \frac{\lambda}{4\sqrt{2\ln 2}NA\sqrt{1+\frac{P_{\mathrm{STED}}}{P_S}}} \qquad \text{Equation 2.3}$$

with P_S as determined from the fit of Figure 2.4g. We estimated *N*, the number of photons collected per line scan, by fitting a simple model to the experimentally determined number of photons, $N = As/(1 + BP_{\mathrm{STED}})$. Here, *A* and *B* are fit parameters that characterize, respectively, the dependence of the number of collected photons on the width of the intensity distribution and the reduction of maximum photon emission rate due to a non-zero intensity in the minimum of the STED stripe (Supplementary Figure 2.5). To determine the optimal ideal localization precision, B was set to 0 (Figure 2.5d, dashed curve). The experimental localization precision also includes DNA fluctuations, σ_{DNA}, and additional noise, σ_{add}, associated with, for instance, drift or non-ideal line-to-line-repeatability of beam scanning, such that $\langle(\Delta x)^2\rangle_{\mathrm{meas}} = \langle(\Delta x)^2\rangle + {\sigma_{\mathrm{DNA}}}^2/N + {\sigma_{\mathrm{add}}}^2$. Using σ_{DNA} = 13 nm (calculated for 4 pN tension), a fit of σ_{add} to our data in Figure 2.5d yields σ_{add} = 3.6 nm (Supplementary Figure 2.6).

1D diffusion simulation. Diffusion trajectories were simulated by successively adding displacements Δx, drawn randomly from a Gaussian distribution with $\langle \Delta x \rangle = 0$ and $\langle \Delta x^2 \rangle = 2D_{\mathrm{input}} \Delta t$, using a small time step Δt of 0.4 ms and a diffusion constant D_{input}. These trajectories were binned to match the line-scan rate of our TFAM data, and white noise was added with a standard deviation of 12 nm to account for the localization precision. For a given D_{input}, MSD analysis was performed on 100,000 trajectories, each 150 bins long (~8 s), to approximate the distribution of measured diffusion constants.

No evidence for enhanced photonicking by STED. An intrinsic advantage of performing STED imaging in optical tweezers is that the structural integrity of the DNA and the presence of nicks can be directly evaluated by monitoring the force on the microspheres and (over)stretching the DNA: A double-stranded break in the DNA would break the link between the two beads, leading to zero force on the beads, and loss of the DNA in the image. No such double-stranded breaks have been observed during confocal or STED imaging. Photonicking (single-stranded break), however, would keep the link between the beads intact. The presence of nicks can be evaluated by overstretching DNA in medium to low ionic conditions: As the double-helix melts during overstretching, the presence of a nick would lead to a loss in the link between the two beads.[06] Indeed, no significant additional photo nicking was observed after confocal or STED imaging of labeled proteins on DNA. Although there is a finite chance that single nicks in long molecules may not be observed in an incomplete overstretching experiment, the lack of observation of additional nicks implies that the rate of photonicking is not elevated to the extent that numerous nicks exist after STED imaging.

Retarded TFAM diffusion. The diffusion constant of monomeric TFAM,[26] $D_{\mathrm{ref}} \approx 0.08$ $\mu m^2/s$ is slower than diffusion of typical proteins that undergo rotation-coupled translation along the DNA helix ($D \approx 0.2 – 0.6$ $\mu m^2/s$).[07] Assuming large values of the TFAM radius R = 3 nm and the width of its helical path R_{oc} = 2 nm, and a typical average free energy barrier for sliding $\varepsilon = k_B T$, we obtain a lower estimate of the TFAM diffusion constant in case of rotation-coupled translation of D = 0.5 $\mu m^2/s$, which is indeed significantly higher than D_{ref}.[08] This suggests that TFAM translocation is heavily retarded by a strong DNA-protein interaction. This strong interaction can be related to the elongated structure of TFAM with three DNA-interaction sites, and is consistent with its ability to bend and compact mitochondrial DNA.[24,25]

To a first, overly simplified, approximation, D is considered to be inversely proportional to the number of TFAM monomers in an oligomer, N_{TFAM}, such that $D = D_{\mathrm{ref}}/N_{\mathrm{TFAM}}$. The solid grey line in Figure 2.7d represents the expected distribution of D if we assume a mix of equal populations of oligomers with N_{TFAM} = 1,2,3,…,12, which is in reasonable agreement with the measured diffusion data. Direct analysis of the correlation of D with I_{norm} (not possible here due to the low labeling ratio) could further elucidate the scaling of D with N_{TFAM} at high protein density.

Appendix B: Supplementary figures

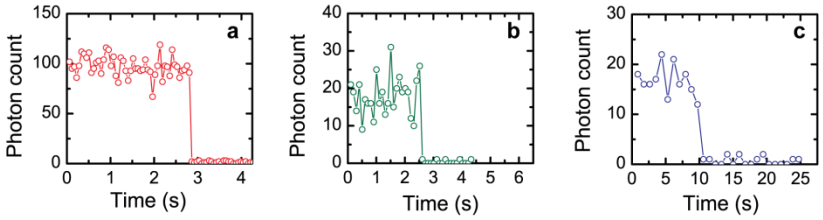

Supplementary Figure 2.1 Single fluorophore bleaching traces. (**a**-**c**) Show time traces of bleaching steps of respectively EcoRV-Atto647N, Sytox orange, and an EGFP-labeled protein, measured by confocal microscopy on optically stretched DNA.

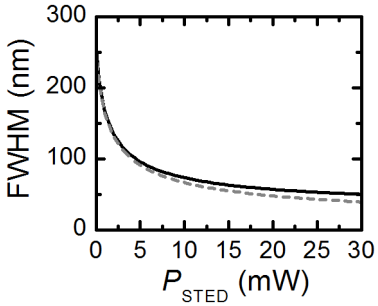

Supplementary Figure 2.2 Resolution scaling with STED power. The solid line corresponds to the fitted $FWHM_{meas}(P_{STED})$ of Figure 2.4g, where we used P_I as fit parameter and $FWHM_{DNA} = 31\,\mathrm{nm}$. By suppressing DNA fluctuations, the spatial resolution can be improved towards the dashed line, which uses $FWHM_{DNA} = 0\,\mathrm{nm}$, for instance by applying high tension. The difference between the two curves highlights the apparent reduction of the spatial resolution due to the fluctuations of the DNA, under the experimental conditions of Figure 2.4g (at 4 pN tension).

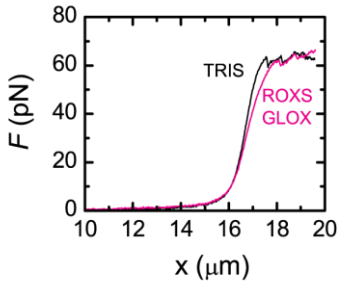

Supplementary Figure 2.3 Effect of ROXS and enzymatic oxygen removal (GLOX) on DNA mechanics. The black curve shows a force-distance curve of λ DNA in a 20 mM tris buffer with 100 mM NaCl. The magenta curve shows a force-distance curves of λ DNA in the same buffer supplemented with 1 mM methylviologen and 2 mM trolox (ROXS), with enzymatic oxygen removal by glucose oxidase, catalase, and glucose (GLOX). At forces over 30 pN, a small length increase (<5%) is apparent in presence of ROXS GLOX. Although this could be suggestive of intercalation of the ROXS components, it is a strikingly weak effect compared to intercalation by, for example, ethidium, YoYo-1, and ruthenium complexes,[04,05] which induce far more drastic changes to force-distance curves at concentrations that are 5 to 6 orders of magnitude smaller than those used here. Furthermore, the overstretching plateau, which is known to be sensitive to intercalating and groove binding buffer constituents, occurs at ~65 pN for all curves.

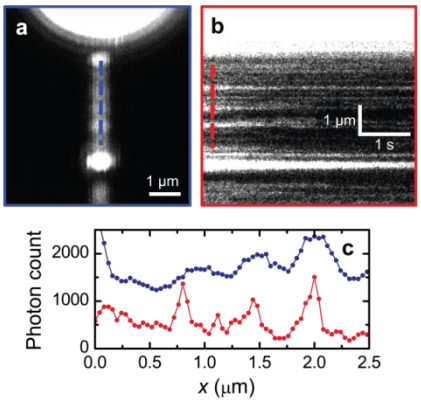

Supplementary Figure 2.4 STED nanoscopy of DNA that is densely coated with TFAM. (**a**) Confocal microscopy image of TFAM-Atto647N filaments at high density on DNA. (**b**) STED kymograph of the section of the DNA imaged in (b). STED power 16 mW. (**c**) Cumulative intensity profile as indicated in **a** (blue) and **b** (red), comparing confocal and STED profiles. The STED intensity profile exhibits peaks at ~100 nm spacing, indicating that STED can indeed be used to image dense DNA-bound protein filaments with unprecedented resolution.

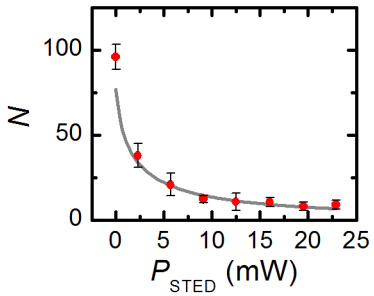

Supplementary Figure 2.5 Number of photons per line scan of a single DNA-bound protein as function of STED power. The symbols show the experimentally determined number of photons per line scan as function of STED power corresponding to the data of Figure 2.5d. The line is the fit of the model described in the Online Methods, which takes into account the dependence of the number of photons on the width of the intensity distribution and the loss of photons due to a non-zero intensity in the line-shaped minimum of the STED beam.

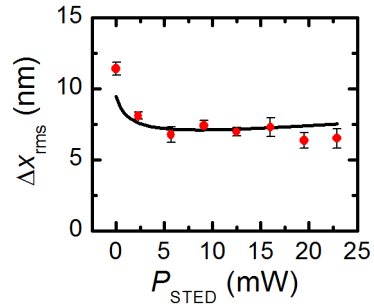

Supplementary Figure 2.6 Fit of the experimental localization precision of Figure 4d. The symbols correspond to the measured localization precision of **Figure 2.4d**. The line is a fit of the additional noise term σ_{add}, using the model described in Appendix A, yielding σ_{add} = 3.6 nm.

References

1. Cornish, P. V & Ha, T. A *ACS Chemical Biology* **2**, 53–61 (2007).

2. Moerner, W. E. *Proceedings of the National Academy of Sciences of the United States of America* **104**, 12596–12602 (2007).

3. Neuman, K. C. & Nagy, A. Single-molecule force spectroscopy: optical tweezers, magnetic tweezers and atomic force microscopy. *Nature Methods* **5**, 491–505 (2008).

4. Joo, C., Balci, H., Ishitsuka, Y., Buranachai, C. & Ha, T. Advances in single-molecule fluorescence methods for molecular biology. *Annual review of biochemistry* **77**, 51–76 (2008).

5. Candelli, A., Wuite, G. J. L. & Peterman, E. J. G. Combining optical trapping, fluorescence microscopy and micro-fluidics for single molecule studies of DNA-protein interactions. *Physical chemistry chemical physics : PCCP* **13**, 7263–7272 (2011).

6. Moffitt, J. R., Chemla, Y. R., Smith, S. B. & Bustamante, C. Recent advances in optical tweezers. *Annual review of biochemistry* **77**, 205–228 (2008).

7. Harada, Y. *et al.* Single-molecule imaging of RNA polymerase-DNA interactions in real time. *Biophysical journal* **76**, 709–715 (1999).

8. Van Mameren, J. *et al.* Counting RAD51 proteins disassembling from nucleoprotein filaments under tension. *Nature* **457**, 745–748 (2009).

9. Lang, M. J., Fordyce, P. M., Engh, A. M., Neuman, K. C. & Block, S. M. Simultaneous , coincident optical trapping and single-molecule fluorescence. *Nature Methods* **1**, 1–7 (2004).

10. Hohng, S. *et al.* Fluorescence-force spectroscopy maps two-dimensional reaction landscape of the holliday junction. *Science (New York, N.Y.)* **318**, 279–283 (2007).

11. Comstock, M. J., Ha, T. & Chemla, Y. R. Ultrahigh-resolution optical trap with single-fluorophore sensitivity. *Nature Methods* **8**, 335–340 (2011).

12. Hell, S. W. Microscopy and its focal switch. *Nature Methods* **6**, 24–32 (2009).

13. Klar, T. A., Jakobs, S., Dyba, M., Egner, A. & Hell, S. W. Fluorescence microscopy with diffraction resolution barrier broken by stimulated emission. *Proceedings of the National Academy of Sciences of the United States of America* **97**, 8206–8210 (2000).

14. Donnert, G. *et al.* Macromolecular-scale resolution in biological fluorescence microscopy. *Proceedings of the National Academy of Sciences of the United States of America* **103**, 11440–11445 (2006).

15. Moneron, G. *et al.* Fast STED microscopy with continuous wave fiber lasers. *Optics express* **18**, 1302–1309 (2010).

16. Kasper, R. *et al.* Single-molecule STED microscopy with photostable organic fluorophores. *Small* **6**, 1379–1384 (2010).

17. Noom, M. C., Van Den Broek, B., Van Mameren, J. & Wuite, G. J. L. Visualizing single DNA-bound proteins using DNA as a scanning probe. *Nature Methods* **4**, 1031–1036 (2007).

18. Gittes, F. & Schmidt, C. F. Interference model for back-focal-plane displacement detection in optical tweezers. *Optics letters* **23**, 7–9 (1998).

19. Moffitt, J. R., Chemla, Y. R., Izhaky, D. & Bustamante, C. Differential detection of dual traps improves the spatial resolution of optical tweezers. *Proceedings of the National Academy of Sciences of the United States of America* **103**, 9006–9011 (2006).

20. Klar, T., Engel, E. & Hell, S. Breaking Abbe's diffraction resolution limit in fluorescence microscopy with stimulated emission depletion beams of various shapes. *Physical Review E* **64**, 066613 (2001).

21. Dijk, M. A. Van, Kapitein, L. C., Mameren, J. Van, Schmidt, C. F. & Peterman, E. J. G. Combining optical trapping and single-molecule fluorescence spectroscopy: enhanced photobleaching of fluorophores. *The journal of physical chemistry. B* **108**, 6479–6484 (2004).

22. Willig, K. I., Rizzoli, S. O., Westphal, V., Jahn, R. & Hell, S. W. STED microscopy reveals that synaptotagmin remains clustered after synaptic vesicle exocytosis. *Nature* **440**, 935–939 (2006).

23. Sánchez, E. J., Novotny, L., Holtom, G. R. & Xie, X. S. Room-Temperature Fluorescence Imaging and Spectroscopy of Single Molecules by Two-Photon Excitation. *The Journal of Physical Chemistry A* **101**, 7019–7023 (1997).

24. Thompson, R. E., Larson, D. R. & Webb, W. W. Precise nanometer localization analysis for individual fluorescent probes. *Biophysical journal* **82**, 2775–2783 (2002).

25. Persson, F. *et al.* Fluorescence nanoscopy of single DNA molecules by using stimulated emission depletion (STED). *Angewandte Chemie (International ed. in English)* **50**, 5581–5583 (2011).

26. Ngo, H. B., Kaiser, J. T. & Chan, D. C. The mitochondrial transcription and packaging factor Tfam imposes a U-turn on mitochondrial DNA. *Nature structural & molecular biology* **18**, 1290–1296 (2011).

27. Rubio-Cosials, A. *et al.* Human mitochondrial transcription factor A induces a U-turn structure in the light strand promoter. *Nature Structural Molecular Biology* **18**, 1281–1290 (2011).

28. Farge, G. *et al.* Protein sliding and DNA denaturation are essential for DNA organization by human mitochondrial transcription factor A. *Nature communications* **3**, 1013 (2012).

29. Eggeling, C. *et al.* Direct observation of the nanoscale dynamics of membrane lipids in a living cell. *Nature* **457**, 1159–1162 (2009).

30. Patterson, G., Davidson, M., Manley, S. & Lippincott-Schwartz, J. Superresolution imaging using single-molecule localization. *Annual review of physical chemistry* **61**, 345–367 (2010).

31. Gross, P., Farge, G., Peterman, E. J. G. & Wuite, G. J. L. Combining optical tweezers, single-molecule fluorescence microscopy, and microfluidics for studies of DNA-protein interactions. *Methods in Enzymology* **475**, 427–453 (2010).

32. Bonnet, I. *et al.* Sliding and jumping of single EcoRV restriction enzymes on non-cognate DNA. *Nucleic acids research* **36**, 4118–4127 (2008).

33. Bückers, J., Wildanger, D., Vicidomini, G., Kastrup, L. & Hell, S. W. Simultaneous multi-lifetime multi-color STED imaging for colocalization analyses. *Optics express* **19**, 3130–3143 (2011).

34. Vladescu, I.D., McCauley, M.J., Nun, M.E., Rouzina, I. & Williams, M.C. Quantifying force- dependent and zero-force DNA intercalation by single-molecule stretching. *Nat. Methods* **4**, 517-522 (2007).

35. Murade, C.U., Subramaniam, V., Otto, C. & Bennink, M.L. Interaction of Oxazole Yellow Dyes with DNA Studied with Hybrid Optical Tweezers and Fluorescence Microscopy. *Biophys. J.* **97** 835–843 (2009).

36. van Mameren, J. *et al.* Unraveling the structure of DNA during overstretching by using multicolor, single-molecule fluorescence imaging. *Proc. Natl. Acad. Sci. USA* **106**, 18231-18236 (2009).

37. Blainey, P.C. *et al.* Nonspecifically bound proteins spin while diffusing along DNA. *Nat. Struct. Mol. Biol.* **16**, 1224-1229 (2009).

38. Bagchi, B., Blainey, P.C. & Xie, X.S. Diffusion Constant of a Nonspecifically Bound Protein Undergoing Curvilinear Motion along DNA *J. Phys. Chem. B* **112**, 6282–6284 (2008).

3 Mobility Analysis of Proteins on DNA

Fluorescence microscopy in conjunction with optical tweezers is well suited to the study of protein mobility on DNA. Here, we evaluate the benefits and drawbacks of super-resolution and conventional imaging techniques for the analysis of one-dimensional (1D) protein diffusion as commonly observed for DNA-binding proteins. In particular, we demonstrate the visualization of DNA-bound proteins using wide-field, confocal, and stimulated emission depletion (STED) microscopy. We review the suitability of these techniques to conditions of high protein density, and quantify their performance in terms of spatial and temporal resolution. Tracking proteins on DNA forces one to make a choice between localization precision on the one hand, and the number and rate of localizations on the other, by altering imaging modality, excitation intensity, and acquisition rate. Using simulated diffusion data, we quantify the effect of these imaging conditions on the accuracy of 1D diffusion analysis. In addition, we consider the case of diffusion confined between local roadblocks, a case particularly relevant for proteins bound to DNA. Together these results provide guidelines that can assist in judiciously optimizing the experimental conditions required for the analysis of protein mobility on DNA and other 1D systems.

Based on: Iddo Heller*, Gerrit Sitters*, Onno D Broekmans, Andreas S Biebricher, Gijs JL Wuite & Erwin JG Peterman, *Chemphyschem* **15**, 727-33 (2014)

3.1 Introduction

While processing and maintaining the genome, proteins continuously interact with and travel along DNA.[1] The motion of proteins on DNA can be diffusive, as is often the case when proteins scan the DNA for specific sequences or damages,[2] or it can be processive and directed, as in the case of helicases and polymerases.[3] Quantification of protein mobility can provide new insights into, for example, the enzymatic turnover cycle,[4] or the speed and efficiency of a one-dimensional (1D) target search while sliding over DNA.[5,6]

The single-molecule toolkit is equipped with exquisite techniques to study such protein mobility at the single-DNA and single-protein level.[7] In particular, fluorescence microscopy allows the visualization and tracking of proteins in three dimensions over both the micrometer and nanometer length scales.[7,8] Concurrently with visualization, optical tweezers can be used to manipulate the DNA molecule.[2,9,10] In this way, the DNA can be forced to adopt the conformation of a single, straight line, instead of the random 3D conformation of unconstrained DNA that severely hampers the study of proteins moving along the DNA.[11] Moreover, optical tweezers can be used to apply and measure tension on the DNA.[12-14] In the analysis of protein mobility it is particularly important that the tension applied to the DNA suppresses the amplitude of the thermal fluctuations in the DNA conformation, which can disturb image quality by motion blurring.[11,15] It is of additional experimental benefit if the optically trapped DNA is not tethered to the surface, such that buffers can be exchanged rapidly and effectively by moving the DNA between different channels of a microfluidic flow cell.[16]

To date, the fluorescence techniques that have been combined successfully with optical tweezers include total internal reflection (TIRF) microscopy,[2] wide-field microscopy,[14,17] and confocal microscopy.[9,11,18,19] Each of these visualization approaches has its own set of strengths and weaknesses for the analysis of protein mobility. More recently, stimulated emission depletion (STED) super-resolution microscopy has been integrated with optical tweezers, and provides access to the regime in which proteins are present on DNA at a high density, as is often the case in the cell.[11] Alternatively, localization-based super-resolution methods[20] such as photo-activated localization microscopy/stochastic optical reconstruction microscopy (PALM/STORM) should also be capable of resolving individual DNA-bound proteins present at high density, but this combination has not yet been

demonstrated. Moreover, these localization-based super-resolution techniques appear to be less well-suited for the study of rapid dynamics, as large amounts of photons need to be collected sequentially and in a spatially stochastic manner, which is detrimental for a good temporal resolution.

In this contribution, we review the strengths and weaknesses of both conventional and super-resolution visualization approaches in terms of their range of accessible assay conditions, as well as in terms of their range of accessible image acquisition parameters for the analysis of protein mobility. We have focused our discussion and experimentation on wide-field microscopy, confocal microscopy, and STED microscopy. Total internal reflection (TIRF) microscopy is not included in this discussion but should be comparable to conventional wide-field imaging, yet with an improved signal-to-background ratio. In addition to presenting an experimental demonstration of the aforementioned visualization techniques, we quantify, by means of simulations, the effects of the image acquisition parameters on the determination of diffusion parameters using mean-square displacement (MSD) analysis, taking into account both free and confined 1D diffusion. Finally, by relating the results of these simulations to the different imaging techniques, we aim to provide guidelines for selecting the best imaging technique and conditions for the analysis of protein mobility on DNA.

3.2 Results

3.2.1 Imaging Techniques

Figure 3.1a-c illustrates protein mobility assays on optically trapped DNA, based on wide-field fluorescence microscopy, confocal fluorescence microscopy, and 1D-STED microscopy, respectively. In wide-field microscopy, a relatively wide (tens of micrometers) excitation beam illuminates the entire DNA molecule and image acquisition involves relaying an image of the DNA onto a camera (Figure 3.1a). In confocal microscopy, a focused excitation beam is scanned over the DNA to generate an image point-by-point, using a point detector to detect (single) photon emission (Figure 3.1b). As an extension of confocal microscopy, STED microscopy uses a depletion beam superimposed onto the focused excitation beam to inhibit fluorescence emission in a spatially selective manner (Figure 3.1c). The focal intensity distribution of the depletion beam is modified to exhibit, for example, a central point of zero intensity (i.e. an STED doughnut), such that fluorescence

emission is only inhibited through saturated stimulated emission in the high-intensity periphery of the focal spot.[21] Consequently, the spatial resolution is enhanced to a value below the diffraction limit. Here we focus on 1D-STED, which uses a line of zero intensity and enhances resolution only in the direction parallel to the DNA.[11,21]

Spatial Resolution and Protein Density

Figure 3.1d-f shows images of proteins bound to optically stretched DNA, which were obtained with wide-field, confocal, and 1D-STED microscopy, respectively. The spatial resolution of conventional techniques such as wide-field and confocal microscopy is limited by diffraction to about 250 nm, as can be judged from the widths of the fluorescent spots due to the individual fluorophores (Figure 1d,e). STED can enhance the spatial resolution by up to 50 nm, depending on the intensity of the depletion beam and the quality of the focal spot (Figure 3.1f).[11] Consequently, STED is most suited to the study of DNA that is densely covered with proteins, as is the case in the cell. STED allows individual proteins to be distinguished on DNA that is covered by up to 20 labeled proteins per micrometer. In contrast, diffraction-limited techniques are only suited for imaging up to, on average, three to four proteins per micrometer (Table 3.1).

Temporal Resolution

The temporal resolution of the image acquisition can affect the results of protein tracking on DNA. High-end electron multiplying charge-coupled device (EMCCD) cameras have pixel readout rates as high as 10 MHz, such that bacteriophage λ DNA with a length of approximately 16 µm can, in principle, be imaged at sub-

Table 3.1 Characteristic specifications for fluorescence microscopy imaging of single labeled proteins on optically stretched DNA

	Spatial resolution [nm]	Temporal resolution [ms]	Localization precision [nm]	Protein density on DNA [μm^{-1}]	Protein concentration [nM]
wide-field	250	10	10[a]	4	1
confocal	250	10[b]	10[a]	4	100
1D-STED	50	5[c]	5[d]	20	100

[a] Typical values when number of photons per fluorophore is $N_{photons}$ = 100. [b] Assuming 1D-scanning confocal microscopy. [c] The spatiotemporal resolution for tracking is better for 1D-STED than for 1D confocal (c.f. Figure 3.2). [d] $N_{photons}$ = 10.

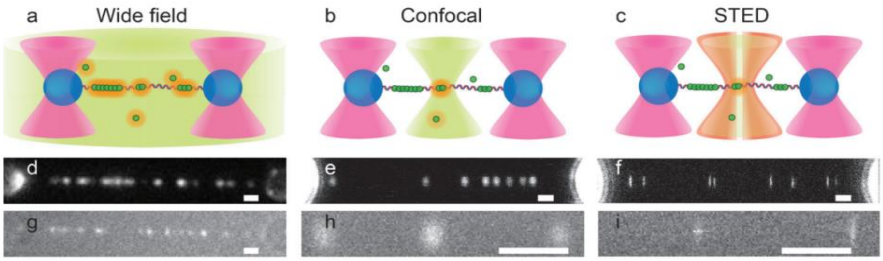

Figure 3.1 Concurrent optical trapping and fluorescence microscopy. (**a–c**) Illustration of assays of protein mobility on DNA using (**a**) wide-field, (**b**) confocal, and (**c**) STED microscopy. (**d–i**) Images of fluorescently labeled proteins on optically stretched DNA (**d–f**) in the absence, and (**g–i**) in the presence of labeled proteins in solution, acquired using d,g) wide-field, (**e,h**) confocal, and (**f, i**) STED microscopy. Scale bars: 1 mm. The maximum grayscale values (white) correspond to (**e**) 15, (**f**) 8, (**h**) 140, and (**i**) 80 photons. The slightly elliptical shape of the photon distributions in **e** and **h** is due to linear polarization of the excitation light. Background concentrations of proteins: (**d–f**) 0 nM, (**g**) approximately 5 nM, (**h–i**) approximately 50 nM.

microsecond frame times using wide-field microscopy (100 nm pixels). In practice, however, single-molecule imaging on DNA is limited by the excitation intensity and the fluorescence emission rate of the fluorophores, to values of about 10-100 Hz. Confocal and STED imaging are typically slower than wide-field microscopy, owing to the raster scanning that is required to generate 2D images using these beam-scanning techniques. However, in order to track proteins on optically stretched DNA, only 1D line scanning, along the DNA, is required, which drastically increases the speed of imaging. Fast scanning tip-tilt piezo stages have been shown to enable a temporal resolution below 10 ms (sub-microsecond temporal resolution is also made possible by employing galvanometric mirrors or resonant scanning mirrors).[11] In such scanning approaches, the focusing of the excitation beam can result in substantially higher excitation intensities than in wide-field illumination, and this enables higher temporal resolution. However, such high excitation intensities can result in enhanced photobleaching of the fluorophores, which reduces the number of photons that can be collected from a single protein trajectory.[11,22,23]

Background Rejection and Protein Concentration

The techniques illustrated in Figure 3.1a-c differ in their ability to image DNA-bound proteins in the presence of a background of fluorescently labeled proteins in solution (Figure 3.1g-i). In conventional wide-field microscopy, out-of-focus background signals originating from fluorescent labels that are excited throughout the sample volume, above and below the image plane, can overwhelm the signal from the DNA-bound proteins. Single dyes can be observed on the DNA in a labeled protein solution of at most about 5 nM (Figure 3.1g). In confocal fluorescence microscopy, the background signal is reduced by tight focusing of the excitation light on the DNA and spatial filtering of the fluorescence signal by a detection pinhole.[11,24] As a result, confocal microscopy is capable of resolving individual fluorophores on DNA at background concentrations of up to 100 nM (Figure 3.1h). In STED, the effective confocal volume is even further reduced, and this should provide access to even higher background concentrations. In the 1D-STED case, however, background rejection does not significantly exceed that of confocal microscopy; this is most likely due to the large contribution of background fluorescence that originates from just above or below the focal plane and is not effectively suppressed by 1D-STED.

Localization Precision

Tracking proteins on DNA typically involves localizing proteins in subsequent images in order to compose a trajectory that can be used for further analysis (Figure 3.2a). For large numbers of photons collected in a single image (>10), the precision with which a protein can be localized is, in general, limited by photon-counting noise.[25] In this case, the localization accuracy can be approximated as:

$$\Delta x_{\mathrm{pc}} = FWHM \Big/ \sqrt{N_{\mathrm{photons}}} \qquad \text{Equation 3.1}$$

where *FWHM* is the spatial resolution, and N_{photons} represents the number of photons collected per protein per image. The localization precision can thus be enhanced by collecting more photons (e.g. by increasing the intensity of the excitation beam and/or using a longer integration time per pixel). Interestingly, in the case of line-scanned STED with, for example, a doughnut or stripe-shaped intensity distribution, N_{photons} is directly proportional to *FWHM*, such that the localization precision improves with the square root of the spatial resolution enhancement as shown by:[11]

$$\Delta x_{\mathrm{pc}} \propto \sqrt{FWHM} \qquad \text{Equation 3.2}$$

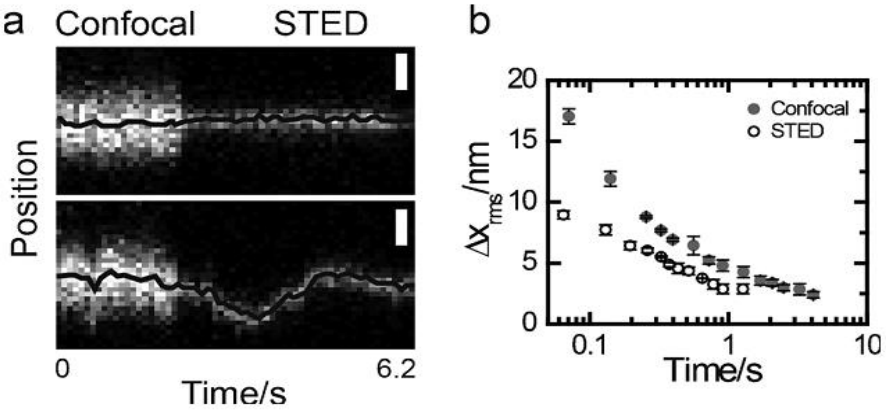

Figure 3.2 Spatiotemporal resolution for tracking proteins on DNA. (a) Kymographs of immobilized (top) and diffusing (bottom) Atto647N-labeled proteins on optically stretched DNA, imaged partially by confocal microscopy and partially by STED nanoscopy (PSTED = 6 mW) Scale bars: 200 nm. Black lines track the centers of the photon distributions and were obtained by fitting 1D Gaussians to each pixel column. (b) Localization precision (Δx_{rms}) measured for immobilized proteins on DNA, as a function of integration time.

which makes localization using STED more precise than the two conventional techniques (see Figure 2.5 in Chapter 2) Since tracking proteins on DNA relies on the repeated localization of proteins, the reduced photon-counting noise leads to an enhancement in spatiotemporal resolution (i.e. better localization precision for a given integration time, or a lower integration time for a given localization precision). We quantified this experimentally by tracking immobilized proteins on optically trapped DNA using confocal and STED microscopy, as shown in Figure 3.2a, top panel (for comparison, the bottom panel of Figure3.2a shows a protein that diffuses along the DNA). The fluctuations in the tracked position of immobilized proteins (Δx_{rms}) are plotted as a function of the integration time in Figure 3.2b. The data in Figure 3.2b demonstrate that STED provides an approximately two-fold higher spatial or four-fold higher temporal resolution than confocal imaging (under conditions of equal excitation intensity). Finally, in cases in which $N_{photons}$ is very low, the background noise can contribute significantly to the localization precision. The background noise differs substantially between the imaging techniques (e.g.

due to differences in dark counts, read noise, amplification noise, quantum efficiency, acquisition time per pixel, and so forth).

Another factor to keep in mind when localizing proteins on DNA, is that thermal fluctuations of the strands during image acquisition will blur the image of DNA-bound proteins and set a lower limit to the effective localization precision. Tension applied to the DNA molecule by optical tweezers, however, can suppress such fluctuations in a controlled way.[15] As a result, localization with a precision in the order of 10 nm is possible at applied forces over 1—5 pN (for bacteriophage λ DNA).[11,15]

3.2.2 Image acquisition parameters

The techniques discussed above set boundaries for the accessible range of protein densities and concentrations, and for image acquisition parameters such as the accessible spatiotemporal resolution. But what is the rele vance of these imaging parameters for the accuracy of mean-squared-displacement (MSD) analysis of protein mobility? Below, we quantify the effect of image acquisition parameters on MSD analysis of simulated 1D diffusion trajectories, using a typical value for the diffusion constant of proteins on DNA, D=0.5 $\mu m\, s^{-2}$.[26] Although other more advanced methods exist to analyze and quantify diffusion,[27] we use MSD analysis here because it is the most widely used method.

As discussed above, the position of a protein can be localized with high precision if a large number of photons is collected (due to the lower photon-counting noise).[25] However, when tracking the motion of a fluorescently labeled protein on DNA (i.e. when repeatedly localizing the protein), only a limited total number of photons can be collected before the fluorophore photobleaches. For all simulations shown here we have assumed that the total number of photons that makes up a single trajectory is 5000.[28] When tracking proteins, a choice must be made as to whether this limited photon budget is spent on many localizations, N_{loc}, of low photon count, $N_{photons}$, which thus have poor localization precision (e.g. by using a low excitation intensity or short pixel integration time), or on few localizations of high precision (e.g. using a high excitation intensity or long pixel integration time). We quantified the effect of optimizing N_{loc} at the cost of $N_{photons}$, or vice versa, by performing MSD analysis on simulated trajectories of free 1D diffusion. Figure 3.3a shows simulated kymographs (frame rate 20 Hz) that represent the two extreme cases, with either an optimal number of localizations (N_{loc}=500, $N_{photons}$=10, and Δx_{rms}=35 nm), or an optimal number of photons $N_{photons}$ detected per frame (N_{loc}=50, $N_{photons}$=100, and

Δx_{rms}=11 nm; this latter case is shown in the inset in Figure 3.3a). We used such simulated kymographs to track proteins and calculate MSD curves as shown in Figure 3.3b. Linear fits of equation:

$$MSD = 2Dt + offset \qquad \text{Equation 3.3}$$

to the individual MSD curves yield estimates of the diffusion constant, *D*.[29,30] Figure 3.3c shows the two distributions of *D* obtained from MSD analyses of 10,000 such simulated trajectories (for either N_{loc}=50 (gray) and N_{loc}=500 (black), such as those shown in Figure 3.3a,b). These results clearly show that the spread in estimated *D* is much smaller if many low precision localizations are acquired, than if few high precision localizations are acquired, despite the better localization precision in the latter case. We further quantified this trend by analyzing simulated trajectories that vary in their value of $N_{photons}$ (and thus in the value of N_{loc}). Figure 3.3d,e shows that, although *D* is correctly estimated for all image acquisition parameters, the accuracy of the estimate is inversely related to the number of localizations, N_{loc} (Figure 3.3e), with a large relative error in *D* of up to 50 %. (Since the accuracy in the estimation of *D* cannot be determined through conventional error analysis due to the use of statistically correlated data in MSD analysis, we have instead displayed the 95 % and 68 % intervals of the distributions of estimated *D* in Figure 3.3d as objective parameters of accuracy).

Typically, however, proteins do not diffuse freely along DNA, as was assumed in Figure 3.3a-e; instead, their diffusion is in most cases confined, either by the tethered DNA ends, or by roadblocks such as other proteins. In the cell, in which many proteins are bound to DNA, this is also a relevant situation. In order to test the effect of this confined diffusion, we confined the simulated diffusion trajectories by introducing reflective boundaries at ±1 µm (Figure 3.3f). The confinement length, *L*=2 µm, was chosen as an intermediate distance between typical roadblocks *in vivo* (roughly 10—100 nm) and DNA ends or artificially low protein densities *in vitro* (about 1—10 µm). Individual MSD curves can be calculated using such simulated confined trajectories, which clearly deviate from those for free diffusion by showing a plateau at high dwell times (c.f. Figure 3.3b,g). We estimated values for *D* and *L* by fitting approximate equations, as derived in ref. [31] (see Experimental Section), to our MSD data. In the case of confined diffusion, the frame rate and/or trajectory length of the acquired data is of particular importance: for a given photon budget, one may choose to track a protein for a brief period of time at a high frame rate (e.g. for 5 s at 100 Hz, assuming N_{loc}=500), or for an extended period of time at a low frame rate (e.g. for 50 s at 10 Hz), as illustrated in Figure

3.3f. We analyzed simulated trajectories sampled at a range of frame rates and plotted the distribution of estimated values for *L* and *D* in Figure 3.3h,i, respectively (N_{loc}=500). The distribution of *D* obtained from MSD fits (Figure 3.3h) is not affected to a large extent by the frame rate. In contrast, the frame rate has a strong effect on the width of the distribution of estimated *L* (Figure 3.3i): longer trajectory lengths (i.e. lower frame rates) provide more accurate estimates of *L*. The median values and the 68 % and 95 % intervals of the distributions are displayed in Figure 3.3j,k, and confirm this trend: whereas the accuracy in the estimation of *D* is relatively unaffected by the sampling rate, the most accurate estimate of *L* is obtained if the total acquisition time exceeds the typical diffusion time between the boundaries (i.e. $t \gg 4$ s for D=0.5 $\mu m^2 s^{-1}$ and L=2 µm). Only when the frame rate is chosen to be so low that the time between individual localizations is comparable to the typical diffusion time between the boundaries does the accuracy of the determination of *D* deteriorate (in this case for f <1 Hz).

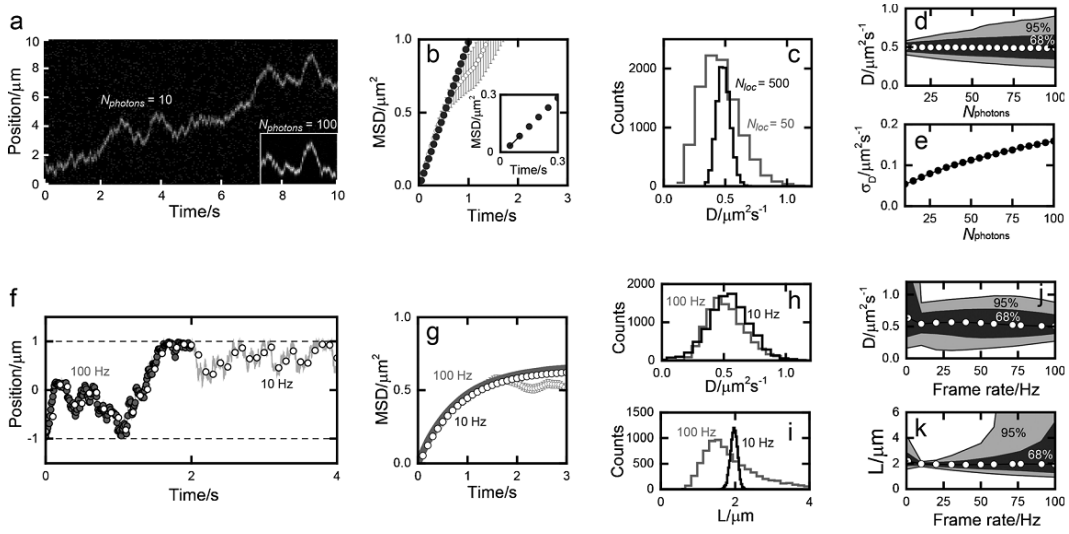

Figure 3.3 Effect of image acquisition parameters on the analysis of protein mobility quantified using simulated diffusion trajectories. (**a**) Simulated kymograph of a protein undergoing free 1D diffusion, sampled with Nphotons=10, Nloc=500 (only first 10 s shown). The inset shows the same trajectory sampled with Nphotons=100, Nloc=50. (**b**) Individual (open symbols, s.d. standard deviation as in Experimental Section) and averaged (filled symbols) MSD curves calculated for trajectories sampled as in **a**. The inset shows the first 0.3 s of the MSD curve. (**c**) Distributions of diffusion constants obtained from fits of individual MSD curves as in **b**. Gray, Nphotons=100, Nloc=50; black, Nphotons=10, Nloc=500. (**d**) Median values and (**e**) standard deviations of the distributions of diffusion constants (symbols), as in **c**, plotted as a function of Nphotons. The light and dark gray shaded areas in **d** represent the intervals that contain 95 % and 68 % of the distributions, respectively. (**f**) Simulated trajectories (gray line) of confined 1D diffusion, sampled at 100 Hz (filled gray symbols) and at 10 Hz (open symbols). (**g**) Individual (open gray symbols, s.d., 20 Hz) and averaged (filled symbols, 100 Hz; open symbols, 10 Hz) MSD curves calculated for trajectories sampled as in **f**. Here, different sampling rates cause different motion blurring, which leads to a difference in offsets between the curves. Distributions of (**h**) diffusion constants and (**i**) confinement lengths L, obtained from fits of MSD curves as in **g**. Median values of the distributions of (**j**) diffusion constants and (**k**) confinement lengths as in **h** and **i**, respectively, (symbols), plotted as a function of frame rate. The light and dark gray shaded areas represent the intervals that contain 95 % and 68 % of the distributions, respectively.

3.3 Discussion and Conclusion

In this article we have analyzed the effectiveness of wide-field, confocal, and STED microscopy for studying protein mobility on optically stretched DNA. We reviewed and quantified the precision of analysis of protein mobility using these techniques. What can we currently conclude to be the best imaging technique for the analysis of a specific biological problem? Before answering this question, we must mention that, although all of these techniques are readily capable of analyzing protein mobility on DNA over a wide range of conditions, differences between the techniques become most relevant when imaging at the more extreme limits of accessible conditions.

The actual assay conditions, in particular the protein concentration in solution, are the most important parameters for the choice of imaging technique. If a study must be performed in a background of fluorescently labeled proteins greater than 1 nM (e.g. in the case of low affinity and/or high off-rates), wide-field microscopy is typically not the best choice. The far more efficient background rejection of confocal and STED microscopy means these techniques perform substantially better under such conditions of high protein concentration (up to 100 nM). Furthermore, if protein mobility is studied at a high density of proteins on the DNA, STED microscopy is preferred over conventional, diffraction-limited imaging techniques, since it enables imaging and distinguishing of up to 20 proteins per micrometer of DNA. In addition, if the analyzable trajectories are short because of the short diffusion times before proteins unbind, hit boundaries, or oligomerize, which is likely to occur at higher protein density, the enhanced spatiotemporal resolution of STED is beneficial.

After evaluating restrictions based on assay conditions, what image acquisition parameters should be chosen for the analysis of protein mobility, and to what extent are these parameters limited by the imaging technique used? To answer these questions, we quantified the effect of imaging parameters on the accuracy of protein mobility analysis on DNA using simulated diffusion trajectories. These simulations demonstrated that, for the most accurate analysis of diffusion parameters, the available photon budget is best spent on maximizing the number of localizations at the expense of the number of photons per localization, which is of less importance. This implies that confocal microscopy and wide-field imaging are the best choices for the analysis of protein mobility because of their lower photobleaching rates, which result in better photon budgets. Here, imaging with a

low background noise allows localizations with lower numbers of detected photons to be performed.

Furthermore, the temporal resolution of the imaging technique sets an upper limit to the rate at which trajectories can be sampled. The sampling rate plays an important role if the diffusive motion of proteins is confined, for example, due to the use of short DNA, local roadblocks, or a high density of other proteins on the DNA. Under such confined diffusion circumstances it is important to use, on the one hand, a sampling rate that is high enough to properly estimate D (i.e. Δt smaller than the typical diffusion time between boundaries, for example, $\Delta t \ll 4$ s when L=2 μm and D=0.5 $\mu m^2 s^{-1}$). On the other hand, proper estimation of the typical confinement length demands an effective usage of the photon budget, such that trajectories can be sampled for a time longer than the typical time needed for the protein to diffuse between the boundaries. For all visualization techniques, it is possible to obtain a higher temporal resolution by increasing the excitation intensity in order to acquire photons at a higher rate. Such higher intensities, however, can lead to higher photobleaching rates due to nonlinear bleaching processes.[22,23] If these nonlinear photobleaching processes are relevant for the dye used, the higher intensity used in confocal microscopy might be disadvantageous compared with wide-field microscopy. Similarly, STED microscopy reduces the number of photons that can be collected due to enhanced photobleaching,[11] and this is partially compensated for by the lower number of photons (compared with confocal or wide-field microscopy) required to localize a protein with the same precision. In specific cases in which L is short (i.e. comparable to, or smaller than, the diffraction limit ≈250 nm), STED microscopy is most suitable for the estimation of both L and D for two reasons: STED allows for the highest temporal resolution for tracking, and it provides the highest spatial resolution. Moreover, if the boundaries can be discerned [e.g. if the (roadblock) proteins are labeled or the optically trapped microspheres are visible], the high spatial resolution of STED allows the tracking of proteins in closer proximity to the boundaries, and for longer. An additional advantage of the beam-scanning techniques is that, in cases in which only single 1D-scans are performed for tracking, less motion blur occurs because the time it takes for the beam to scan over a single protein is typically much smaller than the time set by the line-scan rate during which the entire DNA is scanned.

Analysis of protein mobility on DNA can be performed using a number of different imaging techniques. Of these techniques, wide-field imaging is most straightforwardly combined with optical trapping and it is the most benign in terms

of photobleaching. Moreover, wide-field microscopy is compatible with most biological assays under commonly used *in vitro* conditions that involve low protein densities. Under more extreme *in vitro* or typical *in vivo* conditions, however, wide-field imaging might not suffice. High concentrations of labeled proteins in solution or on DNA demand the use of confocal or STED imaging. In addition, when a higher temporal resolution is required, confocal or STED can be preferable to wide-field imaging. We have shown that STED provides a higher spatiotemporal resolution for tracking proteins on DNA than confocal microscopy. This is particularly useful for studies at biologically relevant protein densities. The technological advancements demonstrated and discussed here for confocal imaging and, in particular, STED imaging on optically trapped DNA, open the door for studies of DNA-protein interactions at biologically relevant protein densities as found inside the cell.

3.4 Experimental Section

Fluorescently labeled proteins were imaged on optically stretched bacteriophage λ DNA tethered to polystyrene microspheres using experimental setups and procedures described previously in refs. [14,15,32] (Figure 3.1a,d,g), and in Chapter 2 (Figure 3.1b,c,e,f,h,i). In brief, optical trapping was performed using 1064 nm trapping lasers with typical powers of 0.5-1 W per trap. Wide-field images were acquired using Cy5-labeled (Figure 3.1d, 647 nm excitation) and Cy3-labeled (Figure 3.1g, 532 nm excitation) proteins. Confocal and STED images were acquired using Atto-647N-labeled proteins (Figure 3.1e,h,f,i, 640 nm confocal excitation; Figure 3.1f,i, 745 nm depletion (STED) beam, ≈5 mW power).

To quantify the effect of imaging parameters on the accuracy of mobility analysis (Figure 3.3), we generated a database of 10,000 1D diffusion trajectories. Each diffusion trajectory was generated by successively adding 500,000 displacements Δ*x*, drawn randomly from a Gaussian distribution with mean=0 and standard deviation:

$$\sigma = 2D\Delta t \qquad \text{Equation 3.4}$$

where *D* is the diffusion constant as defined in the text and the time step Δ*t*=0.1 ms.

For the analysis of free diffusion (Figure 3.3a-e), the 10,000 trajectories were subsequently binned every 500 time steps to mimic data acquisition with a frame

rate of 20 Hz. Each bin was assigned $N_{photons}$ photons. Only a limited number of bins, N_{loc}, was used for further analysis such that the sum of photons over the used bins (i.e. the photon budget) equaled 5,000 and N_{loc}=5,000/N. White noise was added to the bins with a standard deviation:

$$\sigma_{\mathrm{loc}} = \sqrt{s^2/N + a^2/12N + 4\sqrt{\pi}s^3b^2/\left(aN^2\right)} \qquad \text{Equation 3.5}$$

to account for photon-counting noise, pixilation noise and background noise. s, a, b, and N are the standard deviation of the effective focal intensity distribution, the pixel size, the background noise, and the number of photons, respectively.[25] We assumed s=106 nm (i.e. *FWHM*=250 nm), a=75 nm and b=0.2 photons/pixel, such that, for example, the extreme cases N=10 and N=100, yield σ_{loc}=35 nm and σ_{loc}=11 nm, respectively. In the Supporting Information we show that motion blurring, which is not taken into account in this general approach, has negligible effect on the accuracy of mobility analysis.

For the analysis of confined diffusion (Figure 3.3f-k), each of the 10,000 trajectories was confined between two reflective boundaries by repetitively folding back the remainder of a trajectory after it crossed a boundary until the trajectory was entirely confined to ±L/2. Here, the initial positions of the traces were set to random values between ±L/2. Subsequently, the confined traces were binned with varying bin sizes to mimic data acquisition with different frame rates. Only the first 500 bins were used for further analysis, and no additional noise was added in order to rule out effects of poor localization precision on mobility analysis.

We calculated mean-squared-displacement (MSD) as function of lag time (t) from each binned free diffusion trace and fit these curves using Equation 3.6 with weights w_i:

$$MSD = 2Dt + offset \qquad \text{Equation 3.6}$$

$$w_i = 1/\sigma_i^2 = 3i\left(N_{\mathrm{loc}} - i + 1\right)/\left(\left(MSD_i - {\sigma_{\mathrm{loc}}}^2\right)^2 \times \left(2i^2 + 1\right)\right) \qquad \text{Equation 3.7}$$

where i is the index of the lag time.[30] We used only the first 2-3 points of these linear MSD curves in the fitting procedure, which, under the simulated conditions, represents the optimal number of points that provides the most accurate estimate of D.[29] To extract both D and L from MSD curves calculated using the confined

diffusion trajectories, we used the approximate equation derived in ref.[31] as fit function:

$$MSD = \frac{L^2}{6} - \frac{16L^2}{\pi^4} \sum_{n=1(\text{odd})}^{9} \frac{1}{n^4} \exp\left\{ -\frac{1}{2} \left(\frac{n\pi\sqrt{2D}}{L} \right)^2 t \right\} \quad \text{Equation 3.8}$$

Here, we used only the first five terms of the sum for our analysis, which represents >99.98 % of the total MSD(*t*). The fits were weighed by $1/\sigma_{MSD}^2$, where σ_{MSD} is the standard deviation calculated per trajectory for each lag time. For fitting we did not include the full MSD curve. Diffusing proteins typically explore the entire space between boundaries in a lag time:

$$t = L2/2D \quad \text{Equation 3.9}$$

which is equal to 4 s for *L*=2 µm and *D*=0.5 $\mu m^2 s^{-1}$. Thus, over the last 4 seconds of the MSD, the squared displacement is typically not averaged over the entire space between the boundaries, such that fits that include these MSD(*t*) values typically yield poor fitting results. Therefore, we discarded the last 4 seconds of the nonlinear MSD curve for the fitting procedure of confined diffusion MSDs.

Appendix A: Additional information

The simulated diffusion trajectories used to quantify the effect of image acquisition parameters on the analysis of protein mobility in Figure 3 of the main text have not taken into account motion blurring. The amount of motion blurring depends strongly on the visualization technique that is used: motion blurring will be largest if photon emission and detection occurs continuously, such as in wide-field microscopy where fluorescence excitation and image acquisition occurs continuously. In other cases, such as in stroboscopic excitation or in beam-scanning techniques such as confocal microscopy, motion blurring will have much smaller effects. To quantify the effect of motion blurring on the accuracy of mobility analysis, we have reproduced the analysis presented in main text Figure 3c both with and without motion blurring due to continuous photon emission. In detail, we simulated continuous photon emission by distributing photons according to a Poissonian distribution over the full temporal resolution (10 kHz) of the 10,000 trajectories. To account for the diffraction limited resolution of the microscope, we add a position offset drawn from a Gaussian distribution with a FWHM of 250 nm and a mean of 0 nm to every photon position. The photon positions are binned over 75 nm intervals to account for pixelation and are summed over 50 ms to mimic data acquisition at 20 Hz. Finally, background noise, which we assume to be distributed exponentially with an average of 0.2 photons/pixel, is added to these summed photon distributions. The mean position of the simulated diffusing emitter is tracked in each trajectory by performing Gaussian fits to the summed photon distributions and MSD analysis is performed as explained in the main text. Supplementary Figures 3.1 compares the averaged MSD curves and distributions of estimated diffusion constants, *D*, calculated using trajectories with (dashed lines) and without (solid lines) motion blurring. This direct comparison shows that motion blurring merely affects the offset of the MSD curve (Supplementary Figure 3.1a). The average slope of the MSD curve, however, which is used to estimate the diffusion constant, D, is unaffected. Since the distributions of estimated D (calculated as in main text **Figure 3.3c**) are indeed unaffected by motion blurring (Supplementary Figure 3.1b), we conclude that motion blurring has negligible effect on the accuracy of mobility analysis References.

Appendix B: Supplementary figures

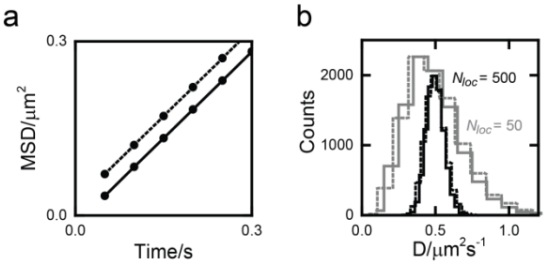

Supplementary Figure 3.1 Effect of motion blurring due to continuous photon emission on the accuracy of mobility analysis. (**a**) Averaged MSD curves calculated for trajectories simulated with (dashed line) and without (solid line) motion blurring (Nphotons = 10, Nloc= 500). (**b**) Distributions of diffusion constants obtained from fits of 10,000 individual MSD curves. Grey, Nphotons = 100, Nloc= 50; black, Nphotons = 10, Nloc= 500, solid, without motion blurring; dashed, with motion blurring.

References

1. R. Phillips, J. Kondev, J. Theriot, R. Bundschuh, *Phys. Today* **2009**, *62*, 44.

2. Y. Harada, T. Funatsu, K. Murakami, Y. Nonoyama, A. Ishihama, T. Yanagida, *Biophys. J.* **1999**, *76*, 709—715.

3. H. Yin, M. D. Wang, K. Svoboda, R. Landick, S. M. Block, J. Gelles, *Science* **1995**, *270*, 1653 -1657.

4. E. A. Abbondanzieri, W. J. Greenleaf, J. W. Shaevitz, R. Landick, S. M. Block, *Nature* **2005**, *438*, 460—465.

5. B. van den Broek, M. A. Lomholt, S.-M. J. Kalisch, R. Metzler, G. J. L. Wuite, *Proc. Natl. Acad. Sci. USA* **2008**, *105*, 15738 -15742.

6. A. Biebricher, W. Wende, C. Escudé, A. Pingoud, P. Desbiolles, *Biophys. J.* **2009**, *96*, L50 -2.

7. W. E. Moerner, *Proc. Natl. Acad. Sci. USA* **2007**, *104*, 12596 -12602.

8. C. Joo, H. Balci, Y. Ishitsuka, C. Buranachai, T. Ha, *Annu. Rev. Biochem.* **2008**, *77*, 51 -76.

9. M. J. Lang, P. M. Fordyce, A. M. Engh, K. C. Neuman, S. M. Block, *Nat. Methods* **2004**, *1*, 133 -139.

10. J. van Mameren, E. J. G. Peterman, G. J. L. Wuite, *Nucleic Acids Res.* **2008**, *36*, 4381 -4389.

11. I. Heller, G. Sitters, O. D. Broekmans, G. Farge, C. Menges, W. Wende, S. W. Hell, E. J. G. Peterman, G. J. L. Wuite, *Nat. Methods* **2013**, *10*, 910 -916.

12. M. A. Van Dijk, L. C. Kapitein, J. Van Mameren, C. F. Schmidt, E. J. G. Peterman, *J. Phys. Chem. B* **2004**, *108*, 6479 -6484.

13. G. Farge, N. Laurens, O. D. Broekmans, S. M. J. L. van den Wildenberg, L. C. M. Dekker, M. Gaspari, C. M. Gustafsson, E. J. G. Peterman, M. Falkenberg, G. J. L. Wuite, *Nat. Commun.* **2012**, *3*, 1013.

14. J. van Mameren, M. Modesti, R. Kanaar, C. Wyman, E. J. G. Peterman, G. J. L. Wuite, *Nature* **2009**, *457*, 745 -748.

15. A. Candelli, G. J. L. Wuite, E. J. G. Peterman, *Phys. Chem. Chem. Phys.* **2011**, *13*, 7263 -7272.

16. M. C. Noom, B. van den Broek, J. van Mameren, G. J. L. Wuite, *Nat. Methods* **2007**, *4*, 1031 -1036.

17. P. R. Bianco, L. R. Brewer, M. Corzett, R. Balhorn, Y. Yeh, S. C. Kowalczykowski, R. J. Baskin, *Nature* **2001**, *409*, 374 -378.

18. S. Hohng, R. Zhou, M. K. Nahas, J. Yu, K. Schulten, D. M. J. Lilley, T. Ha, *Science* **2007**, *318*, 279 -283.

19. M. J. Comstock, T. Ha, Y. R. Chemla, *Nat. Methods* **2011**, *8*, 335 -340.

20. G. Patterson, M. Davidson, S. Manley, J. Lippincott-Schwartz, *Annu. Rev. Phys. Chem.* **2010**, *61*, 345 -367.

21. T. Klar, E. Engel, S. Hell, *Phys. Rev. E* **2001**, *64*, 066613.

22. E. J. Sánchez, L. Novotny, G. R. Holtom, X. S. Xie, *J. Phys. Chem. A* **1997**, *101*, 7019 -7023.

23. A. N. Kapanidis, S. Weiss, *J. Chem. Phys.* **2002**, *117*, 10953.

24. G. Sirinakis, Y. Ren, Y. Gao, Z. Xi, Y. Zhang, *Rev. Sci. Instrum.* **2012**, *83*, 093708.

25. R. E. Thompson, D. R. Larson, W. W. Webb, *Biophys. J.* **2002**, *82*, 2775 -2783.

26. P. C. Blainey, G. Luo, S. C. Kou, W. F. Mangel, G. L. Verdine, B. Bagchi, X. S. Xie, *Nat. Struct. Mol. Biol.* **2009**, *16*, 1224 -1229.

27. A. J. Berglund, *Phys. Rev. E* **2010**, *82*, 011917.

28. J. Vogelsang, R. Kasper, C. Steinhauer, B. Person, M. Heilemann, M. Sauer, P. Tinnefeld, *Angew. Chem.* **2008**, *120*, 5545 -5550; *Angew. Chem. Int. Ed.* **2008**, *47*, 5465 -5469.

29. X. Michalet, *Phys. Rev. E* **2010**, *82*, 041914.

30. J. H. Kim, R. G. Larson, *Nucleic Acids Res.* **2007**, *35*, 3848 -3858.

31. A. Kusumi, Y. Sako, M. Yamamoto, *Biophys. J.* **1993**, *65*, 2021 -2040.

32. P. Gross, G. Farge, E. J. G. Peterman, G. J. L. Wuite, *Methods Enzymol.* **2010**, *475*, 427 -453.

4 The Role of XRCC4 and XLF in DNA Repair

The maintenance of the chromosome depends critically upon repairing double-strand breaks. Non-homologous end joining (NHEJ) is the most prevalent DNA damage repair mechanism in higher eukaryotes in which XRCC4 and XLF, two structurally similar proteins, fulfill key roles. The core components of the NHEJ machinery have been determined genetically and biochemically, but a clear picture of how broken ends are brought together and ligated is lacking. Here we use dual- and quadruple-trap optical tweezers combined with fluorescence microscopy to visualize XRCC4, XLF and XRCC4-XLF complexes on DNA in real time. We show that XLF stimulates the binding of XRCC4 and that both are able to diffuse rapidly over the DNA. We furthermore find that XRCC4-XLF is able to robustly bridge two independent DNA molecules. A substantial number of these bridges is able to slide along the DNA. Together, these findings suggest a novel binding mechanism for both XRCC4 and XLF in the early stages of NHEJ.

Based on: Ineke Brouwer*, Gerrit Sitters*, Andrea Candelli, Stephanie J. Heerema, Abinadabe J. de Melo, Davide Normanno, Mauro Modesti, Erwin JG Peterman, Gijs JL Wuite, Sliding XRCC4-XLF sleeves bridge DNA and connect DNA-ends (not published yet)

4.1 Introduction

DNA double-strand breaks (DSBs) occur during normal progression through the cell cycle and are estimated to occur in dividing cells around ten times per cell per day[1]. These breaks must be repaired in order to avoid genomic instability. Non-Homologous end Joining (NHEJ) is the predominant pathway in mammalian cells to repair two-ended DSBs[2]. Errors in the DNA repair mechanisms of the cell can result in chromosomal aberrations, such as DNA translocations and their corresponding gene fusions, which have been shown to lie at the origin of 20% of human cancer morbidity[3]. Most of these gene fusions remain poorly characterized at the DNA level. In order to develop understanding of this important issue it is essential to characterize the NHEJ pathway at the molecular level.

The key molecular actors involved in NHEJ are Ku70/80, DNA-PKcs, XRCC4, XLF and DNA Ligase IV[4–9]. It is believed that Ku70/80 is responsible of recognizing the ends of the broken DNA molecules and recruitment of DNA-PKcs[9]. A XRCC4-Lig IV complex is thought to ligate the broken ends together, stimulated by XLF[10]. What the mechanistic basis is of XLF's stimulatory effect and how an XRCC4-XLF complex functions during repair is not well understood and currently under debate. In the canonical view XRCC4 and XLF have a role at the end of the NHEJ repair pathway, stimulating the ligation step catalyzed by LigIV[11]. In recent studies it has been shown that XRCC4 and XLF are also present at an early stage of NHEJ, displaying a Lig IV independent function[12] and might have the capability of forming bridges between DNA molecules[2]. This capability is intriguing since it could provide a molecular explanation of the unknown function of XRCC4 and XLF at the early stages of NHEJ.

Resolving how XRCC4 and XLF interact with DNA and resolving their function are challenging research problems. Currently two different contradicting binding modes have been proposed: in one the DNA is wrapped around the XRCC4-XLF complex[13], while in the other the XRCC4-XLF filament binds around the DNA in a helical manner[2]. In this study we aim to shed light on the binding strategies using a single molecule approach. Another important focus of this study is to investigate and quantify the intramolecular DNA bridging of the XRCC4-XLF complex and proposing a model of the role of XRCC4 and XLF in the NHEJ repair pathway.

4.2 Results

4.2.1 Experimental setup and assay

To solve these questions we made use of combined dual- and quadruple-trap optical tweezers, microfluidics and quantitative fluorescence microscopy to monitor the binding, diffusion and mechanical behavior of XRCC4-XLF complexes on DNA. In addition, we used Atto647N-labeled XLF and Alexa Fluor 555-labeled XRCC4 (Figure 4.1a). Optical tweezers were used to hold the DNA (48.5 kbp) taut in order to visualize the DNA bound proteins in real time and to measure the mechanical properties of the protein-nucleic-acid complex (Figure 4.1b). A four-channel laminar flow cell was used to (1) trap two microspheres, (2) capture a DNA molecule between the trapped microspheres, (3) analyze the mechanical properties of the DNA molecule to ensure we have a single tethered DNA molecule, (4) incubation in a flow channel with fluorescently labelled protein and (5) visualization of the protein-DNA complex in buffer without labeled proteins (Figure 4.1c). In several cases we performed measurement directly in the flow channel with labeled proteins. We are able to visualize single DNA-bound proteins in a background of up to 100 nM of labeled proteins when using confocal fluorescence microscopy[14].

4.2.2 Binding, diffusion and mechanics of XRCC4 and XLF

To start our investigation of the interaction between XRCC4 and XLF with DNA, it is important to first investigate their binding affinity and their dynamics on the DNA once bound. Binding properties of XRCC4 and XLF were investigated using a combination of dual-trap optical tweezers with confocal fluorescent microscopy, which allows real-time visualization (time resolution < 1s) of the binding since the fluorescent background in the protein channel is efficiently suppressed[14]. When individually present, both XRCC4 and XLF oligomers bind to DNA with the rates $k_{on,XRCC4} = 23 \pm 5\ \mathrm{s^{-1}\ bp^{-1}\ M^{-1}}$ and $k_{on,XLF} = (6.0 \pm 0.5) \cdot 10^2\ \mathrm{s^{-1}\ bp^{-1}\ M^{-1}}$ respectively, measured at a protein concentration of 50 nM (Figure 4.2a,b). XRCC4 binding (50 nM) is increased in the presence of XLF (50 nM) by an order of magnitude ($k_{on,XRCC4} = (2.7 \pm 0.4) \cdot 10^2\ \mathrm{bp^{-1}\ M^{-1}}$) indicating that XLF facilitates XRCC4 binding to DNA (Figure 4.2c). No clear difference in binding of XLF was observed in the presence of XRCC4. We furthermore observed that 29 ± 5 % of the filaments are composed of both XRCC4 and XLF, 9 ± 3 % of XRCC4 alone and 62 ± 8 % of XLF alone (N = 94 binding events) at a concentration of 5 nM for both proteins. In practically all cases (> 98 %) we observe that XRCC4 and XLF bind as

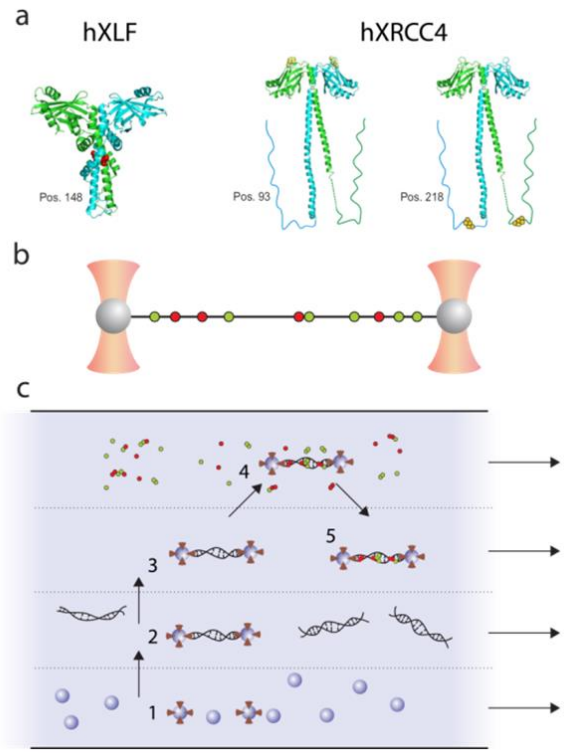

Figure 4.1 Experimental assay and setup. (**a**) Human XLF (hXLF) and human XRCC4 (hXRCC4) protein structures with the dye locations indicated (see Appendix A). XLF is labeled with a single Atto647N fluorophore and XRCC4 is labelled with two Alexa555 fluorophores. Both labelled XRCC4 variants have been used in our study for the different measurements. (**b**) Schematic of an individual DNA molecule tethered between two microspheres. The DNA is held taught to visualize the bound fluorescence labeled proteins. (**c**) A typical experiment is composed of five steps: (1) capture microspheres in the optical trap. (2) Tethering of DNA between the trapped microspheres. (3) Probing the DNA to ensure a single molecule between the microspheres. (4) The DNA is exposed to a buffer with labeled XRCC4 and XLF. (5) The DNA molecule is imaged in the absence of fluorescence protein.

oligomers, indicating that oligomers are present in solution (Supplementary Figure 4.1). Dissociation of the protein complexes is not observed on the timescales of our experiments (up to 1 hour), suggesting that binding is a near-irreversible process and filament disassembly might be a regulatory point in non-homologous end-joining. Once bound we observe that XRCC4, XLF and XRCC4-XLF complexes all have the ability to diffuse rapidly along DNA (Figure 4.2a-c). We furthermore observe that some complexes (15 ± 5 %) are static and that the complexes can switch between static and diffusing states (Supplementary Figure 4.2), suggesting there are two distinct binding modes. We quantified the diffusive behavior by tracking the mobile proteins for a large number of frames (typically more than 100) and calculating their diffusion coefficient D by using a mean square displacement analysis (MSD)[15]. The diffusion coefficient thus obtained for XLF oligomers ($\langle D \rangle = 0.73 \pm 0.09\ \mu m^2\ s^{-1}$) and XRCC4 oligomers ($\langle D \rangle = 0.68 \pm 0.09\ \mu m^2\ s^{-1}$) are comparable at low salt concentration (25 nM KCl) and do not depend on the tension applied to the DNA (Figure 4.2d, Supplementary Figure 4.3). Complexes containing both XRCC4 and XLF diffuse in a comparable manner ($\langle D \rangle = 0.6 \pm 0.2\ \mu m^2\ s^{-1}$, N=8). At higher salt concentration (160 nM KCl) the diffusion coefficient of XRCC4 increases by a factor three ($\langle D \rangle = 2.0 \pm 0.2\ \mu m^2\ s^{-1}$). We were unable to measure the diffusion coefficient of XLF at high salt concentration due to the formation of protein aggregates at these buffer conditions. Interestingly the diffusion rates of the oligomers do not seem to depend on their size (shown for XRCC4 in Figure 4.2e). Together with the observed fast diffusion of the complexes, it seems that the complexes do not follow the helical backbone of the DNA, but probably move in a linear fashion along the DNA (Supplementary Figure 4.4). A DNA-binding mechanism in which the DNA is wrapped around the proteins, as one of the current models predict, is therefore highly unlikely, since this would prevent the rapid motion of the complexes.

Next, we investigated the mechanical response of DNA due to binding of XRCC4 and XLF. In these experiments we observe that the mechanical properties, even of fully coated DNA molecules, remain unchanged (Figure 4.2f). This result is again in line with the idea that XLF-XRCC4 is wrapped around DNA instead of the other way around since a binding mechanism where the DNA is wrapped around the XRCC4-XLF complex would result in shortening of the DNA. To test the mechanical ability of the complex to bridge DNA we relaxed a DNA molecule to an end-to-end distance of 7 μm while incubating it in the protein solution. When DNA is relaxed the fluctuation of the DNA due to thermal motion, allow distinct XRCC4-XLF segments to come into contact forming a loop in the DNA. Afterwards, the force extension

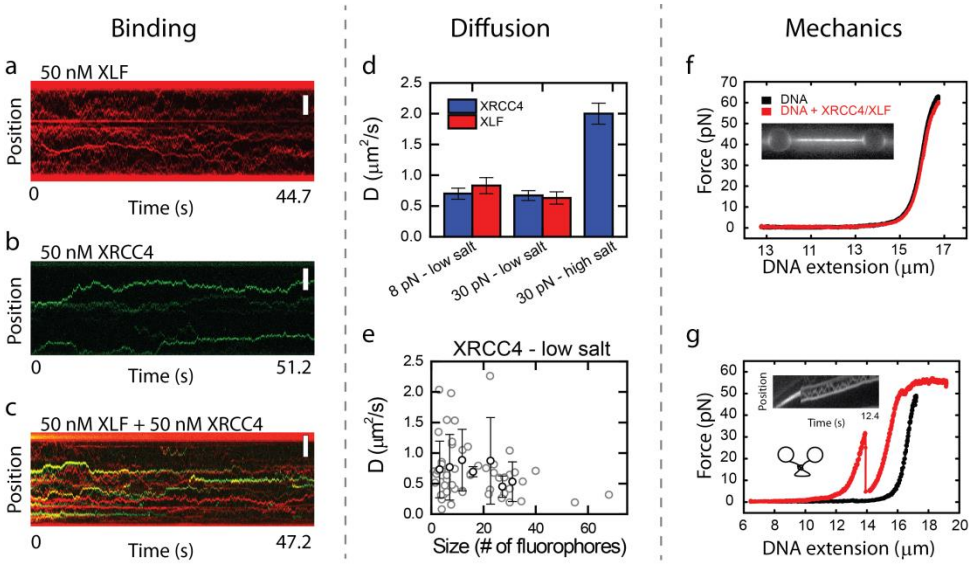

Figure 4.2 Binding, diffusion and mechanics of XRCC4 and XLF. (**a**) Kymograph of a dsDNA molecule in the presence of 50 nM XLF. (**b**) Kymograph of a dsDNA molecule in the presence of 50nM XRCC4. (**c**) Kymograph in the presence of 50 nM XLF and 50 nM XRCC4. Yellow traces are complexes containing both XLF (red) and XRCC4 (green). (**d**) Diffusion coefficients of mobile XLF and XRCC4 proteins measured in a low (25 nM KCl) and high salt (160 nM KCl) environment at two different DNA tensions. The diffusion coefficient of XLF could not be measured at high salt due to aggregate formation. (**e**) The diffusion coefficients of mobile XRCC4 complexes as a function of size. No clear size dependence on the diffusion rate is observed. (**f**) A typical force distance measurement of a DNA molecules, that is incubated under tension (> 1 pN) in the presence of 200 nM XRCC4 and 200 nM XLF, shows that the mechanical properties of the DNA molecule is not altered. The inset, a fluorescent snapshot of the DNA-protein complex after incubation, confirms a full fluorescent coverage. (**g**) A force distance measurement of a DNA molecule, that is incubated at low tension (< 1 pN) in the presence of 200 nM XRCC4 and 200 nM XLF, shows that intra-molecular bridges are formed indicated by the rupture event. The inset, a kymograph recorded during bead separation, shows the rupture event of the intra-molecular bridge mediated by XRCC4-XLF. Scale bars: 4 μm.

behavior shows a shortening of the DNA and large force ruptures, both distinct mechanical responses suggestive of loops in the DNA caused by XRCC4-XLF mediated intra-molecular bridges (Figure 4.2g). Sometimes, we can visualize the ruptures clearly in corresponding kymographs (see inset). Unfortunately, often we observe a shortening of the molecule which looks like protein induced DNA looping but which is in fact caused by sticking of the DNA molecule to one of the beads (Supplementary Figure 4.5).

4.2.3 Intra-molecular bridging

We set out to investigate bridging by XRCC4-XLF complexes with a greater level of control by performing experiments using a combination of quadruple-trap optical tweezers and wide-filed fluorescence microscopy. This combination of techniques enables simultaneous manipulation and visualization of two individual double-stranded DNA molecules. Experiments were performed on complexes formed by incubating 2 dsDNA molecules in either wrapped or crossed configuration in a channel containing 200 nM XLF-Atto647N and 200 nM XRCC4-Alexa555 for 2 minutes (Figure 4.3ai). In kymographs along the diagonal DNA segments (Figure 4.3b) clearly show the formation of static bridges at the junction while additional mobile complexes are observed on other sections of the DNA molecules. In most cases (72 +/- 8%; N= 112), we observe the formation of a DNA-protein bridge at the DNA crossing point within this incubation time. Interestingly, in contrast to the complexes observed on single dsDNA molecules, where only 29 ± 5% of the complexes contained both XRCC4 and XLF, all complexes observed at DNA crossings (112 complexes studied in total) contained both proteins. We also test that it is possible to generate bridges between DNA molecules that are preincubated with proteins and crossed in the absence of free protein in solution (Supplementary Figure 4.6). Finally, we observe that XLF and XRCC4 alone were also able to form intermolecular bridges (Supplementary Figure 4.7). In general however, these bridges seem to be less stable and we furthermore observe that XRCC4 is more prone to aggregation if XLF is not present (compare Supplementary Figure 4.7a to Supplementary Figure 4.6b).

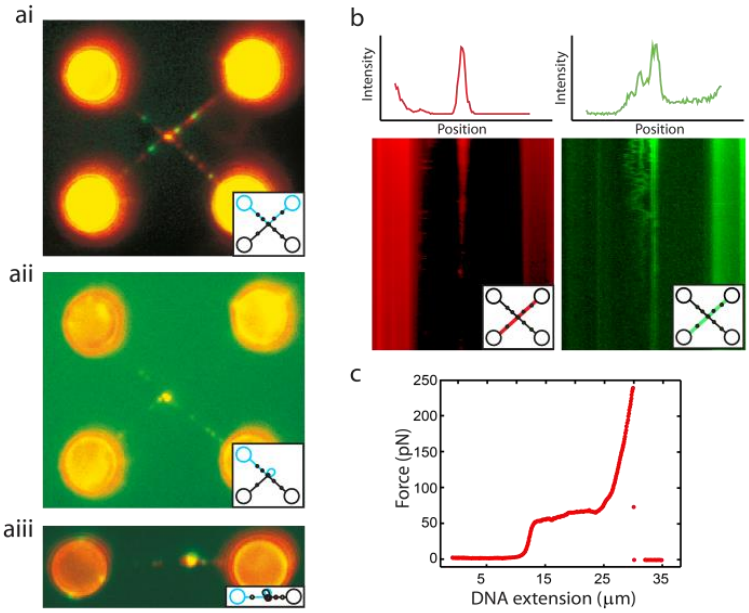

Figuur 4.3 Bridging: XRCC4 and XLF colocalize at DNA crossings where they form highly stable bridges. (**ai**) Fluorescence image (top panel, green shows XRCC4-Alexa555, red shows XLF-Atto647N and yellow shows colocalization) and schematic representation (bottom panel) of 2 dsDNA molecules bridges by an RCC40XF complex after 5 minutes incubation in wrapped conformation in 200 nM XRCC4 and 200 nM XLF. Similar results were obtained in 52 independent experiments. (**aii**) Fluorescence image (top panel) and schematic representation (bottom panel) fo the same XRCC4-XLF-dsDNA complex as in a after detachment of 1 of the 4 DNA segments from the bead. A bridge is still clearing present between the other 3 segments. (**aiii**) Fluorescence image (top panel) and schematic representation (bottom panel) of the same XRCC4-XLF-dsDNA complex as in **ai** and **aii** after rupture of a second DNA segment. Note that there is now a direct connection between two DNA segments originating from different dsDNA molecules. (**c**) Intensity traces along DNA strands connecting top right and bottom left beads. (**d**) Force-extension curve of the complex shown in **aiii**. Note that this is identical to the force-extension curve of a naked dsDNA molecule, indicating that the XRCC4-XLF complex forms a stiff linker between the 2 DNA segments and can withstand 100s of pN.

After bridge formation we tested the stability of the complexes at the junction. Upon the application of high forces (up to 100s of pN) we typically observe detachment of one of the DNA ends from one of the beads, while the other end of the DNA molecule is clearly still attached to the opposite bead (Figure 4.3aii). If a high force is applied once more, a second segment of the DNA will detach from one of the beads, where the protein complex now holds together 2 DNA ends which statistically speaking 2/3 of the time originates from a different DNA molecule (Figure 4.3aiii). Subsequently, a force-extension curve of this newly formed complex can be recorded (Figure 4.3c). This curve is identical to the stretching curve of a dsDNA molecule with an arbitrary length, showing us that we are merely stretching the 2 ends of the dsDNA that are linked by a very stiff and force-resistant complex. The average rupture force of these protein-DNA-complexes is 80 +/-16 pN (N = 14). We believe that the majority of these high-force rupture events are caused by DNA breakage (N = 7 broke at overstretching) or detachment of the biotin-streptavidin bonds linking the DNA to the microspheres (N = 4 broke at forces above overstretching such as the DNA in **Fig 4.3c**) and a minority caused by rupture of the protein bridges (N=3 broke below overstretching). The stability of this interaction suggests that in vivo another mechanism is needed to facilitate the dissociation of the protein complexes after completion of DNA repair. A possible player in this process might be DNA-PKcs, which has been shown to phosphorylate XRCC4 and ablate its bridging function[12] which may lead to protein disassembly.

Possibly the most remarkable property of these strong DNA-protein bridges is that in ~85% of the cases (N = 18 tests), they exhibit the ability to slide along one (~ 40% of the cases) or both (45% of the cases) of the dsDNA molecules (Figure 4.4a,b). The occurrence of this sliding does not depend on the molecular configuration of the dsDNA molecules during incubation: for both crossed and wrapped DNA molecules, the bridge is most likely to be mobile (Figure 4.4c). The ability of XLF-XRCC4 to form mobile junctions between DNA raises questions about the structure of the complexes. Given the evidence so far we conclude that the complexes are helices that wrap around DNA and in most cases they interact minimally with the DNA. Given the mobility of the bridges it now seems that these helices can also wrap around two DNA molecules, leading to a bridge that would still permit sliding of the DNA molecule with respect to each other. But at the same time, the fact that some of the bridges do not show this mobile behavior suggests that there is at least one other binding/bridging mode of the proteins on the DNA.

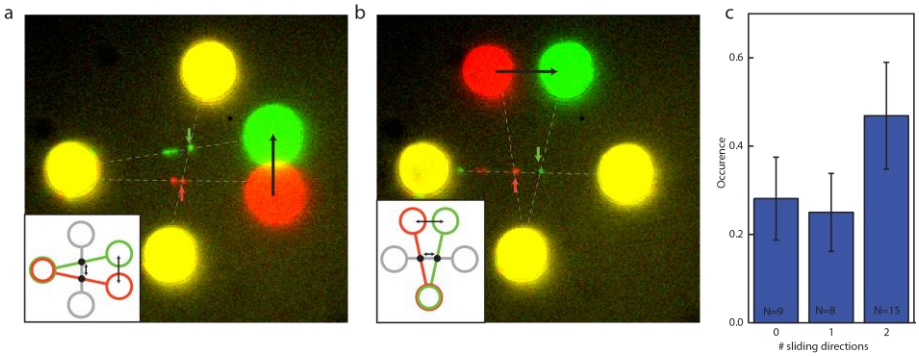

Figuur 4.4 Mechanics of bridging. (**a**) Summed intensity over 22 s of the fluorescence signal from XRCC4-A555 in which the horizontal DNA molecule has been moved upwards, showing that the complex bound at the junction may slide along one of the two DNA molecules. (**b**) The same complex shown in **a**, showing that the complex is also able to slide along the horizontal direction. (**c**) Histogram showing the mobility of XRCC4-XLF bridges at DNA crossings to slide along the dsDNA molecules.

4.3 Conclusion

In conclusion, XRCC4 and XLF form large stable clusters on dsDNA which show a highly dynamic behavior consisting of diffusion, static binding and switching between these states. Binding has no effect on the mechanical properties of the dsDNA, suggesting that the proteins may form a sleeve or cylinder around the DNA which can slide along the DNA helix which may help to localize and bind DNA breaks efficiently. This hypothesis agrees well with the formation of a protein filament around the DNA as proposed by X-ray data[2,11,13,17], where filaments with an inner diameter of 10 nm have been suggested. Once bound, XRCC4-XLF filaments interact with the DNA for long periods up to tens of minutes, suggesting the DNA binding is a near-irreversible process implying that the disassembly of the filaments could be a regulatory-point during NHEJ in vivo. A possible actor for this role could be DNA-PKcs that is able to phosphorylate XRCC4[12]. We have shown that XLF has a stimulatory effect on the binding of XRCC4, increasing its binding rate by an order of magnitude. In addition, we show that XRCC4-XLF complexes are able to bridge DNA molecules, consistent with previous work[2]. These bridges are highly stable,

resisting forces up to 100s of pN. We found that XLF and XRCC4 alone are also able to bridge, but these bridges are in general less stable and less defined. Unlike previously studied DNA bridging proteins, XRCC4-XLF-dsDNA bridges possess the unique capability to slide along the DNA. With this in mind, one could think of a role in Non-Homologous End-Joining for XRRC4-XLF complexes where they form an initial bridge between a broken DNA end and a random location along the other DNA fraction. The fast formation of such a bridge is vital for DNA repair by NHEJ as it prevents the broken ends from moving apart. Then this bridge may slide along the DNA molecules in search of the other broken end. Once this end is found and held together, LigIV could be recruited to perform the final ligation step of NHEJ. This is supported by previous work[2,6,18] where it is shown that both bridging and LigIV binding of XRCC4 takes place at the C-terminal, which could indicate that XRCC4-XLF bridging of broken DNA ends localizes LigIV at the break site, where it can perform the final ligation step of NHEJ.

Appendix A: Additional information

Dual-trap optical tweezers with confocal fluorescence. See chapter 2 for the description of this setup.

Quadruple-trap optical tweezers with wide field fluorescence. Optical trapping of four beads is performed using a 20-W 1064 nm CW fiber laser (YLR-20-LP-IPG, IPG Photonics) with a coupled optical isolator. The laser beam is split in two paths by a polarizing beam splitter after which they are expanded using lenses with focal lengths of 75 mm and 150 mm. Both beams are split again, one by a 50/50 beam splitter and one by a polarizing beam splitter after the polarization is rotated 45 degrees by a half-wave plate, creating four optical paths whereby three have the same polarization. The 150 mm lenses are placed on a linear stage (AG-LS25, Newport) to modify the collimation and with that the height of the traps. This enables us to move the height of two beads with respect to the other two. Beam steering of three traps is done by course-positioning piezo stepper mirrors (AG-M100N, Newport) and one is steered by an accurate piezo mirror (Nano-MTA2X Aluminum, Mad City Labs). The four optical paths are recombined to two paths using a 50/50 beam splitter cube (hereby dumping 50 % of the power) and a polarizing beam-splitter cube, after which these two paths are recombined using 50/50 beam splitter cube (hereby dumping 50 % of the power). Two 300 mm lenses are used to couple the trapping beams into the objective. Force measurements on two microspheres are performed by back focal plane interferometry of the condenser lens using two position sensitive detectors (DL100-7PCBA3, Pacific Silicon Sensor). To obtain the force on the first bead the three paths with the same polarization are separated and dumped before the detectors by a polarizing beam-splitter cube. The other path is detected and is used to perform a force measurement on a microsphere. The force on a second microsphere is detected by overlaying a 980 nm laser (IQ2C140, Power Technology) with an optical path (other than the optical path that is already detected by the PSD) and detected by the second position sensitive detector. LED illumination is used to image the beads on a complementary metal-oxide semiconductor (CMOS) camera (DCC1545M, Thorlabs). Approximately 2W per trap is used leading to a trap stiffness of approximately 0.4 pN/nm for 4.5 μm microspheres. Fluorescence excitation is performed in an epi-, wide-field illumination by a 532 nm laser (Compass 215M-20, Coherent) and a 635 nm laser(IQ1C10(635-12B), power technology). The emitted fluorescence signal is

passed through a band-pass filter and imaged on an EMCCD camera (Cascade 512 B, Princeton Instruments).

DNA, proteins and buffers. DNA constructs were created from biotinylated bacteriophage λ DNA as described previously[19]. The streptavidin microspheres (4.5 µm diameter, Spherotech) were attached to the ends of the DNA using laminar flow[19].

XRCC4 fluorescent labelling was performed with the Alexa Fluor 555 at position 93 or position 218. XLF fluorescent labelling was performed with Atto 647N at position 148. For all protein samples used, protein activity was similar to wild-type activity. This was confirmed by biochemical DNA binding assays and mass spectrometry analysis. In single-molecule assays, no difference was detected between the two different XRCC4 labelling positions (position 93 or 218).

Protein-DNA interactions and force-stretching experiments were conducted in 20 mM Tris-HClpH 7.5, 1 mM DDT and two concentrations of monovalent salt concentrations: 25 and 160 mM KCl.

Appendix B: Supplementary figures

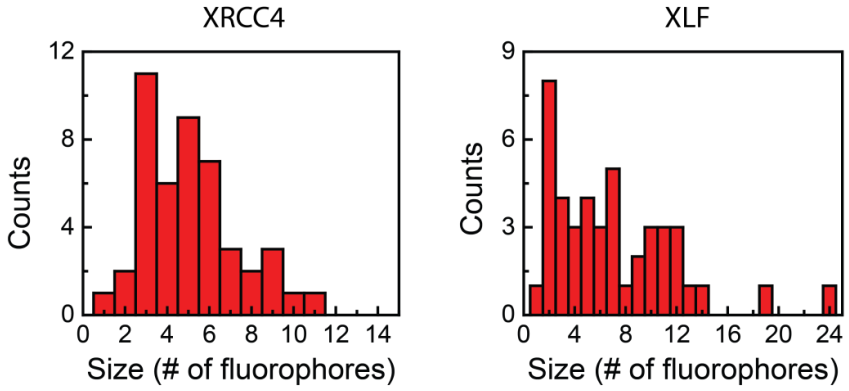

Supplementary Figure 4.1 Size of the protein complexes directly determined after binding by analysis of their fluorescent intensity (at 50 nM protein concentration).

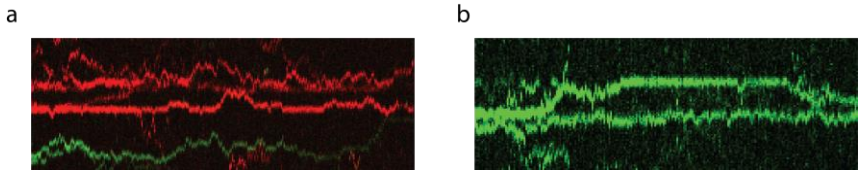

Supplementary Figure 4.2 Typical kymographs showing dynamic switching of (**a**) XLF and (**b**) XRCC4 between a static and a mobile state.

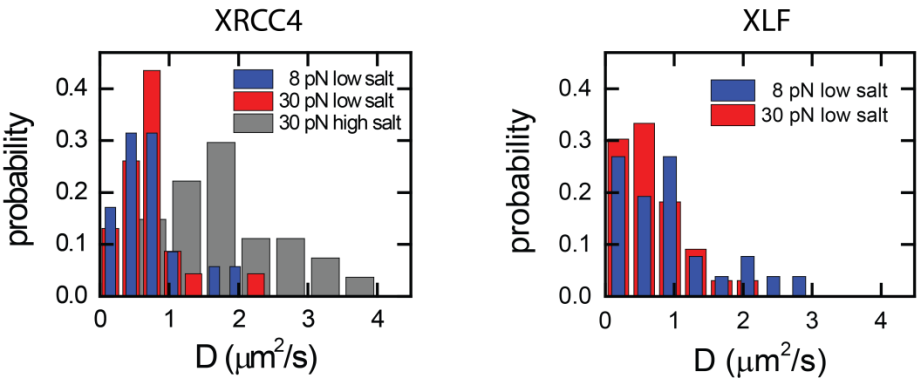

Supplementary Figure 4.3 Left panel shows diffusion coefficients of mobile XRCC4 in low (25 nM KCl) and high salt (160 nM KCl). XRCC4 shows increased mobility when the salt concentration is increased. The force on the DNA did not influence the diffusion. Right panel shows diffusion coefficients of mobile XLF and XRCC4 protein complexes in low salt (25 nM KCl). The force applied on the DNA molecule did not influence the diffusion of the XLF protein. The diffusion coefficient of XLF could not be measured in high salt (160 nM KCl) due to aggregate formation.

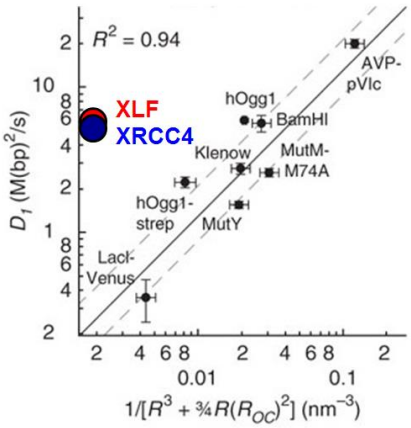

Supplementary Figure 4.4 The diffusion based on the helical diffusion model of Blainey et al[16]. For the XLF and XRCC4 a hydrodynamic radius of 7 nm was assumed, which is the radius of the XLF-XRCC4 filament proposed by Andres et al[2].

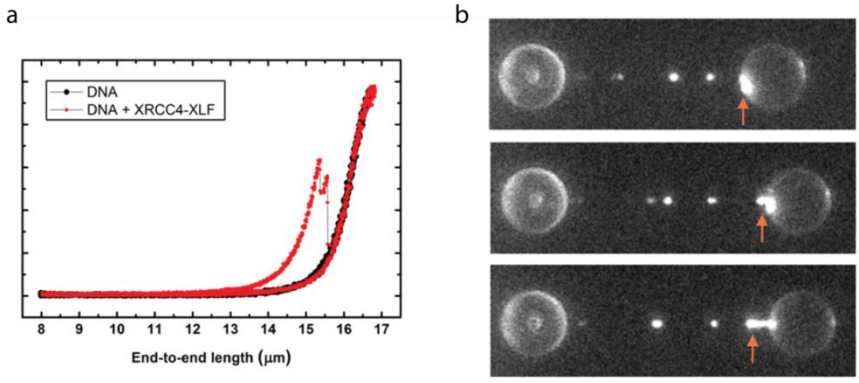

Supplementary Figure 4.5 DNA-protein complexes can attach to polystyrene microspheres (**a**) Force distance curve of bare DNA (black) and after incubation with XRCC4-XLF at low tension (<1 pN). In the red curve a clear force drop is detected, resembling the rupture of an intra-molecular bridge. (**b**) Concurrent fluorescent imaging during bead separation reveals the unspecific absorption of DNA-protein complexes onto the polystyrene microspheres.

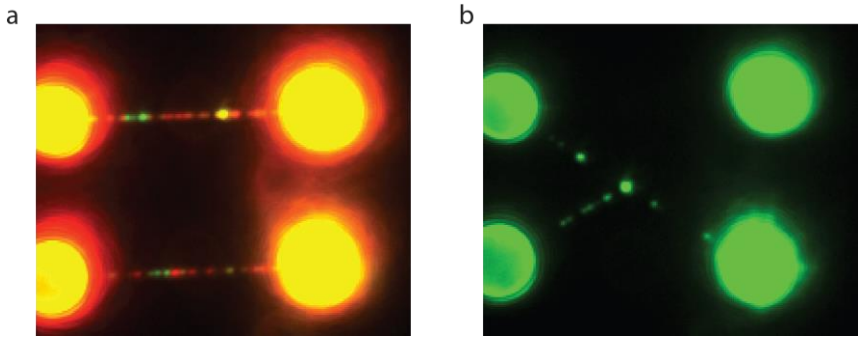

Supplementary Figure 4.6 Bridging can also occur in the absence of free protein in solution. (**a**) Overlay of 491-nm fluorescence and 639-nm fluorescence images taken after incubation of 2 separate dsDNA molecules in 200 nM XRCC4-A555 and 200 nM XLF-A647. Binding of XLF, XRCC4 and XLF-XRCC4 complexes to dsDNA are observed. (**b**) 491-nm fluorescence image taken of same dsDNA molecules after wrapping and unwrapping the molecules in the absence of free protein. Bridge formation is observed, showing that bridging can also occur between pre-formed XRCC4-XLF-dsDNA molecules and does not require free XLF and XRCC4 in solution.

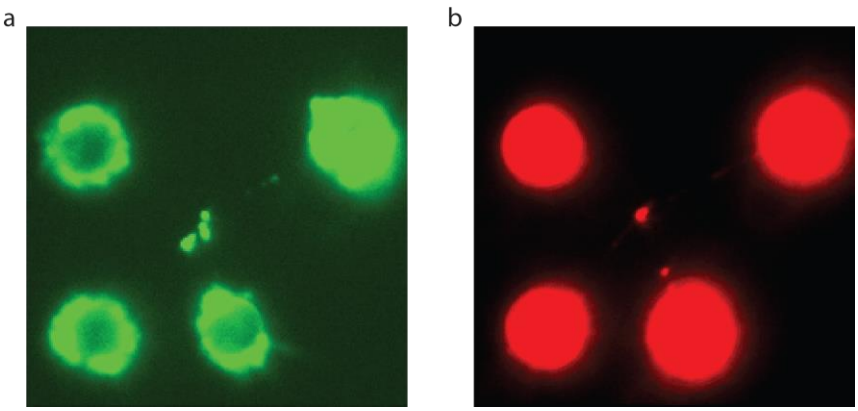

Supplementary Figure 4.7 Both XRCC4 and XLF are capable of intermolecular dsDNA bridging. (**a**) 491nm-fluorescence image taken after unwrapping a dsDNA-XRCC4 complex that was generated by incubating in a buffer containing 200 nM XRCC4-A555 in wrapped configuration. Image clearly shows the ability of XRCC4 to bridge between 2 dsDNA molecules in the absence of XLF. (**b**) 639-nm fluorescence image in a similar configuration the presence of 200 nM XLF-A647N. Again, clear bridge formation is observed in the presence of XLF and the absence of XRCC4.

References

1. Lieber, M. R. *et al.* Nonhomologous DNA End Joining (NHEJ) and chromosomal Translocations in Humans. *Subcell Biochem* **50,** 279–296 (2010).

2. Andres, S. N. *et al.* A human XRCC4-XLF complex bridges DNA. *Nucleic Acids Res.* **40,** 1868–78 (2012).

3. Mitelman, F., Johansson, B. & Mertens, F. The impact of translocations and gene fusions on cancer causation. *Nat. Rev. Cancer* **7,** 233–45 (2007).

4. Junop, M. S., Modesti, M. & Ghirlando, R. Crystal structure of the Xrcc4 DNA repair protein and implications for end joining. **19,** (2000).

5. Li, Y. *et al.* Crystal structure of human XLF/Cernunnos reveals unexpected differences from XRCC4 with implications for NHEJ. *EMBO J.* **27,** 290–300 (2008).

6. Sibanda, B. L. *et al.* Crystal structure of an Xrcc4-DNA ligase IV complex. *Nat. Struct. Biol.* **8,** 1015–9 (2001).

7. Sibanda, B. L., Chirgadze, D. Y. & Blundell, T. L. Crystal structure of DNA-PKcs reveals a large open-ring cradle comprised of HEAT repeats. *Nature* **463,** 118–21 (2010).

8. Andres, S. N., Modesti, M., Tsai, C. J., Chu, G. & Junop, M. S. Crystal structure of human XLF: a twist in nonhomologous DNA end-joining. *Mol. Cell* **28,** 1093–101 (2007).

9. Lieber, M. R. The mechanism of double-strand DNA break repair by the nonhomologous DNA end-joining pathway. *Annu. Rev. Biochem.* **79,** 181–211 (2010).

10. Ahnesorg, P., Smith, P. & Jackson, S. P. XLF Interacts with the XRCC4-DNA Ligase IV Complex to Promote DNA Nonhomologous End-Joining. *Cell* **124,** 301–313 (2006).

11. Wu, Q. *et al.* Non-homologous end-joining partners in a helical dance: structural studies of XLF-XRCC4 interactions. *Biochem. Soc. Trans.* **39,** 1387–92, suppl 2 p following 1392 (2011).

12. Roy, S. *et al.* XRCC4's interaction with XLF is required for coding (but not signal) end joining. *Nucleic Acids Res.* **40,** 1684–94 (2012).

13. Hammel, M. *et al.* XRCC4 protein interactions with XRCC4-like factor (XLF) create an extended grooved scaffold for DNA ligation and double strand break repair. *J. Biol. Chem.* **286,** 32638–50 (2011).

14. Heller, I. *et al.* STED nanoscopy combined with optical tweezers reveals protein dynamics on densely covered DNA. *Nat. Methods* **10,** 910–6 (2013).

15. Heller, I. *et al.* Mobility analysis of super-resolved proteins on optically stretched DNA: comparing imaging techniques and parameters. *Chemphyschem* **15,** 727–33 (2014).

16. Blainey, P. C. *et al.* Nonspecifically bound proteins spin while diffusing along DNA. *Nat. Struct. Mol. Biol.* **16,** 1224–9 (2009).

17. Ropars, V. *et al.* Structural characterization of filaments formed by human Xrcc4-Cernunnos/XLF complex involved in nonhomologous DNA end-joining. *Proc. Natl. Acad. Sci. U. S. A.* **108,** 12663–8 (2011).

18. Modesti, M. *et al.* Tetramerization and DNA Ligase IV Interaction of the DNA Double-strand Break Repair Protein XRCC4 are Mutually Exclusive. *J. Mol. Biol.* **334,** 215–228 (2003).

19. Gross, P., Farge, G., Peterman, E. J. G. & Wuite, G. J. Combining optical tweezers, single-molecule fluorescence microscopy, and microfluidics for studies of DNA-protein interactions. *Methods Enzymol.* **475,** 427–53 (2010).

5 Brownian Dynamics Simulation

Surface-tethered particles are widely used in single-molecule studies. For interpretation of data from such approaches, quantitative understanding of the dynamics of the tethered particle subjected to external forces is crucial. These quantitative descriptions often rely on multiple assumptions and simplifications, such as ignoring particle rotation, that impact this motion. Here we present a simulation method based on the translational and rotational Langevin equation that is able to simulate the motion of a wide variety tethered microsphere systems, over a biophysically relevant force regime, without fit parameters. We show that we are able to predict measured data from tethered-particle motion, magnetic tweezers and flow-stretching experiments. This simulation program provides insights into the effect of different parameters (such as particle size, tether length, medium viscosity, etc.) on the motion of tethered particles, making it a useful calibration tool for biophysicists, allowing the extraction of quantitative information from their measured data.

Based on: Gerrit Sitters, Karl Duderstadt, Erwin JG Peterman, Gijs JL Wuite. Brownian dynamics simulation of tethered microspheres (not published yet)

5.1 Introduction

Single-molecule techniques have greatly expanded our knowledge of biological processes[1]. Many of these techniques make use of surface-tethered particles, such as Tethered-Particle Motion (TPM)[2,3], Acoustic Force Spectroscopy[4], Magnetic Tweezers (MTs)[5,6] and Flow Stretching (FS)[7,8]. A theoretical framework that is able to describe all of these different techniques is highly desirable. Here we describe a numerical simulation that describes the three-dimensional Brownian motion of a tethered particle subjected to any force field (such as magnetic and flow drag) in the biologically relevant regime. We focus on DNA-tethered microspheres, but the model can be readily expanded to simulate other tethers.

Most simulation approaches proposed so far for TPM are based on Monte-Carlo simulations, and thus provide information of the thermodynamic equilibrium[9,10]. It has been shown that, in addition to the thermodynamic equilibrium, the Brownian dynamics of a TPM system can be used to extract valuable information from TPM data[11]. A simulation method that describes the dynamics of tethered particle systems is based on solving the Langevin equation numerically, which is the equation of motion for a particle that is subjected to thermal fluctuations and other external forces[12]. Several Langevin-based models exist but these models typically do not take in to account the microsphere Brownian rotation[13,14] or the (hydrodynamic) interaction between surface and microsphere[13]. As a result the model of Velthuis et al[14] is unable predict TPM data well and the model of Beausang et al[13] requires input parameters that need to be obtained from measured data.

Here we introduce a simulation method that allows us to describe the motion of a wide variety of tethered particle systems in a biologically relevant molecular force regime i.e. from 0 pN up to 30 pN. External forces and torques can be introduced in a straightforward way, allowing simulation of TPM, MTs, FS and other experiments where tethered particles are used. We show that experimental data obtained with TPM, MTs and a combination of MTs and FS can indeed be explained using our model. Overall, this simulation program describes the motion of a tethered particle system with high accuracy, making it an excellent tool for biophysicists to extract quantitative information from their measured data.

5.2 Theoretical background

The motion of a tethered microsphere (Figure 5.1) is derived by calculating both its position and orientation for a large number of time steps, using the Langevin equation at low Reynolds numbers[15] This is allowed since inertia is negligible on the time scales assessed. The surrounding environment interacts with the microsphere by exerting random thermal forces $\vec{F}_{th}$ and torques $\vec{T}_{th}$ to the microsphere, leading to Brownian motion, and via a drag force and drag torque that are proportional to the translational and angular velocity of the microsphere respectively. Due to the proximity of the surface to which the particles are tethered, translation and rotation are coupled[16,17]:

$$\vec{F}_{th} - \begin{pmatrix} \gamma_x(z) \\ \gamma_y(z) \\ \gamma_z(z) \end{pmatrix} \begin{pmatrix} \dot{x} \\ \dot{y} \\ \dot{z} \end{pmatrix} + \begin{pmatrix} \zeta_x(z) \\ \zeta_y(z) \end{pmatrix} \begin{pmatrix} \dot{\alpha}_y \\ \dot{\alpha}_x \end{pmatrix} + \vec{F}_{ext} = 0, \qquad \text{Equation 5.1}$$

$$\vec{T}_{th} - \begin{pmatrix} \beta_x(z) \\ \beta_y(z) \\ \beta_z(z) \end{pmatrix} \begin{pmatrix} \dot{\alpha}_x \\ \dot{\alpha}_y \\ \dot{\alpha}_z \end{pmatrix} + \begin{pmatrix} \chi_x(z) \\ \chi_y(z) \end{pmatrix} \begin{pmatrix} \dot{y} \\ \dot{x} \end{pmatrix} + \vec{T}_{ext} = 0. \qquad \text{Equation 5.2}$$

In Equation 5.1 $\gamma_x(z)$ denotes the effective viscous-drag coefficient in the x-direction, $\dot{x}$ is the microspheres velocity in the x-dimension, $\dot{\alpha}_x$ is the angular microsphere velocity about the x-axis, $\zeta_x(z)$ is a constant that couples the microspheres angular velocity about the *y*-axis to a force in the x-dimension and $\vec{F}_{ext}$ denote all additional external forces. In Equation 5.2 β_x denotes the effective rotational drag coefficient along the x-dimension, $\chi_x(z)$ is a constant that couples the microspheres velocity in the y-dimension to a torque about the x-axis and $\vec{T}_{ext}$ denote all additional external torques. See Appendix A for the hydrodynamic coefficients γ, β, ζ and χ used. The random thermal force and torque are Gaussian distributed (following from the fluctuation-dissipation theorem) with the following properties in the three different dimensions[15,18,19]:

$$\langle F_{th} \rangle = 0, \quad \langle T_{th} \rangle = 0, \qquad \text{Equation 5.3}$$

$$\langle F_{th}(t') F_{th}(t'+t) \rangle = 2\gamma k_B T \delta(t), \qquad \text{Equation 5.4}$$

$$\langle T_{th}(t') T_{th}(t'+t) \rangle = 2\beta k_B T \delta(t). \qquad \text{Equation 5.5}$$

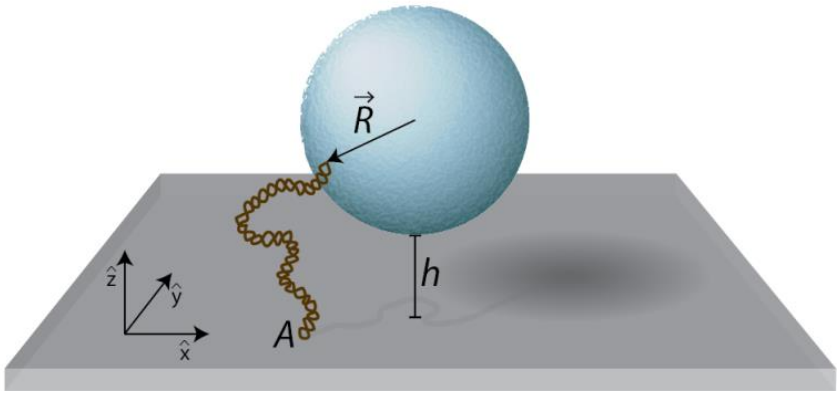

Figure 5.1 Schematic showing the tethered microsphere system. The DNA is anchored to the surface at point A. The vector $\vec{R}$ points from the microsphere center to the DNA-microsphere anchor point and can rotate in three dimensions. The endpoint of $\vec{R}$ determines the extension of the DNA. The distance between surface and microsphere is denoted by h. Note that the width of the DNA is not to scale, in reality this width is much smaller.

with k_B Boltzmann's constant, T the temperature and $\delta(t)$ the Dirac delta function. The external forces that act on the microsphere are the buoyancy force, gravitational force, surface force and the force of the DNA acting on the microsphere:

$$\vec{F}_{ext} = \left[\begin{matrix} \frac{4}{3}\pi R^3 g(\rho_{med} - \rho_{bead}) + \\ 4\pi\epsilon_W\epsilon_0\psi_0^2 R e^{-h/l} \end{matrix} \right] \hat{z} + \vec{F}_{DNA}, \qquad \text{Equation 5.6}$$

with R the microsphere's radius, g Earth's gravitational constant, ρ_{med} and ρ_{bead} the density of the medium and microsphere respectively, ϵ_W and ϵ_0 the permittivity of water and vacuum, ψ_0 the effective surface potential and l the Debye screening length[20] (parameter values are listed in Table 5.1).

Besides the thermal torque, we account for an external torque $\vec{T}_{ext}$ acting on the microsphere caused by the DNA (Figure 5.1):

$$\vec{T}_{ext} = \vec{R} \times \vec{F}_{DNA}. \qquad \text{Equation 5.7}$$

For $\vec{F}_{DNA}$ Gaussian-chain[9], worm like chain (WLC)[21], extendible WLC (eWLC)[22] and finite-WLC (fWLC)[21] polymer models can be used. The fWLC model is an extension of the WLC model accounting for DNA end effects, making the model valid for the regime where the WLC model breaks down (short DNA molecules (< 1 μm) in the low force regime (< 0.1 pN)). The eWLC takes the enthalpic stretching of the DNA backbone at higher forces into account, making the eWLC more accurate than the fWLC in the enthalpic regime (>1pN). We apply the eWLC model when forces of more than a few pN are applied and the fWLC model at lower forces. The Gaussian-chain model was implemented to compare the simulation results to analytical, Gaussian-chain based estimations of Segall et al.[9]. In Figure 5.2a,b the force-distance relation predicted by the different DNA models is presented for the low-force regime for a 500 bp and 10 kbp DNA molecule. The energy needed to extend the DNA provides insight in the extensions accessible by thermal fluctuations (Figure 5.2c,d). Note that additional forces can be implemented in the simulations, such as magnetic forces or solvent-drag forces.

The volume-exclusion effects due to the interaction of the DNA with itself, the surface and the microsphere are ignored. In addition we neglect the time that is needed for the DNA to rearrange itself. These assumptions seem valid since our model (while ignoring these effects) is able to describe measured data accurately.

Table 5.1 Values of the variables used as input parameters of the simulation.

Parameter	Variable	Value
Viscosity of water	η	1 mPas
Density of polystyrene microsphere	ρ_{bead}	1050 $\mathrm{kg/m^3}$
Density of magnetic microsphere	ρ_{bead}	1600 $\mathrm{kg/m^3}$
Density of water	ρ_{med}	1000 $\mathrm{kg/m^3}$
Absolute permittivity of water	$\varepsilon_0\varepsilon_w$	$70.83 \cdot 10^{-13}$ F/m
Effective surface potential	ψ_0	10 mV
Debye screening length	l	2 nm
DNA persistence length	L_p	50 nm
DNA stretch modulus	S	1000 pN

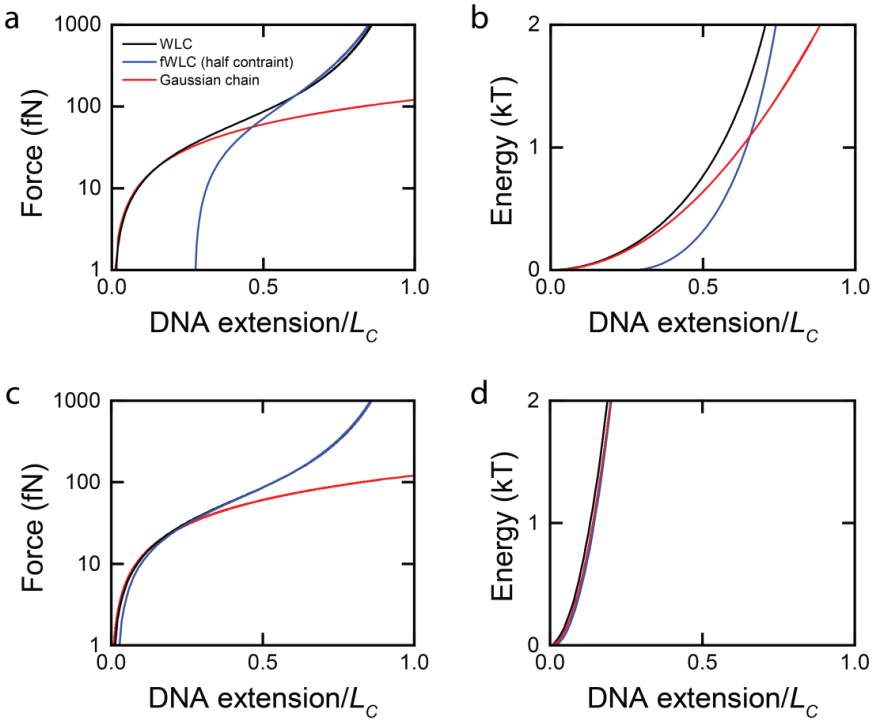

Figure 5.2 (**a**) Force distance curves of the different DNA models for a molecule of 500 bp. The fWLC model assumes half constraint boundary conditions. Below forces of 10 fN the Gaussian chain is a good approximation for the WLC and above 100 fN the difference between WLC and fWLC is negligible. (**b**) The energy that is needed to extend the 500 bp DNA molecule a certain fraction of its contour length for the different models (which is the area below the curves of panel a) to indicate which extensions are accessible by thermal energy. (**c**) Force distance curves for a 10 kbp DNA molecule. Differences between the WLC and fWLC are negligible for DNA molecules of this length. (**d**)The energy needed to extend the 10 kbp DNA molecule a certain fraction of its contour length. On the energy scale of thermal fluctuations the models show no substantia difference.

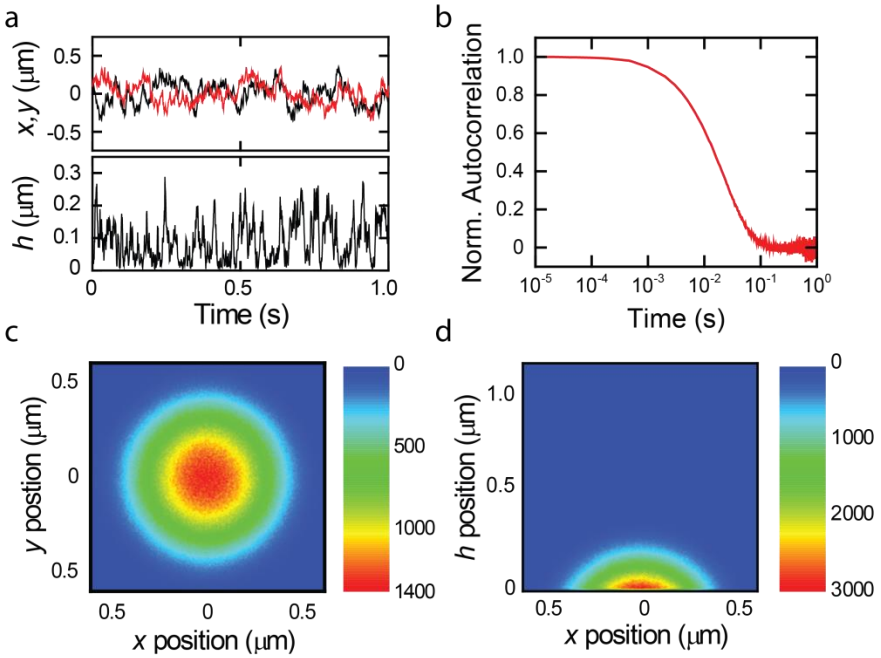

Figure 5.3 Typical simulated TPM data set using DNA with contour length of $0.5\ \mu m$ and a microsphere diameter of 300 nm. (**a**) The three dimensional position (upper panel black data: x, red data: y) time trace of the microsphere center. (**b**) The Normalized autocorrelation time calculated using the x,y data of a 10^5 s time trace with a simulation time step of 10^{-5} s (10^{10} simulation steps). (**c**) Histogram of the x,y positions of the microsphere center. (**d**) h,x position histogram of the simulated trace. The inset shows the same data with a rescaled vertical axis.

The simulations of the particle motion are performed using software written in Labview 2013 via numerical integration (backward Euler method) of differential Equations 5.1 and 5.2. Figure 5.3 shows a typical simulated data set of a tethered particle (0.5 μm DNA contour length, 300 nm microsphere diameter). Simulations yield the particle's three-dimensional trajectory (Figure 5.3a), from which the normalized autocorrelation time of the system can be calculated (Figure 5.3b). Simulating the movement for a large number of steps makes it possible to create high-resolution histograms of the particle positions (Figure 5.3c,d). These

histograms give insight into the volume the microsphere is able to frequent and the probabilities thereof. Note that the position of the DNA-microsphere anchor point and the rotation angle of the microsphere can also be extracted from the simulations.

5.3 Results and discussion

5.3.1 Tethered-particle motion simulations

To validate our model in the low-force regime we compared our simulations with experimental TPM data obtained using different DNA contour lengths L_c and microsphere diameters (Figure 5.4). Figure 5.4a shows the measured and simulated (using the fWLC model) probability distributions of the distance between microsphere center and DNA-surface anchor point $r_\perp = \sqrt{x^2 + y^2}$. The temporal autocorrelations of simulated position time traces are shown in Figure 5.4b. Measurement and simulation agree quantitatively, indicating that our simulations accurately describe both the thermodynamic equilibrium and the dynamics of our system. Note that no prior knowledge from the experiments is used in these simulations: the eight input parameter were obtained from literature or from the microsphere manufacturer (Table 5.1). Next, we investigated the influence of DNA contour length on microsphere excursions (Figure 5.4c), which we quantified by calculating the root mean square values $RMS = \sqrt{\langle (x - \bar{x})^2 + (y - \bar{y})^2 \rangle}$, with $\bar{x}$ and $\bar{y}$ the mean positions over the full measured and simulated time traces[23]. A typical TPM microsphere diameter of 440 nm was used. When the DNA is longer, the microsphere is able to move over a longer distance, leading to a larger RMS value. Both the WLC (dashed grey line) and the fWLC (blue line) model are able to describe the measured microsphere excursion accurately. The Gaussian chain model agrees with earlier analytical models of TPM[9] but overestimates the RMS for DNA molecules that are shorter than a few kilo base pairs (kbp). The small difference in simulated *RMS* between between WLC and fWLC (also for short DNA) indicate that the system has an effective free energy that is larger than $3/2\, k_B T$ (Figure 5.2b). That the WLC, fWLC and Gaussian chain model predict the same *RMS* for larger DNA molecules is expected since the models are virtually equivalent at the energy scale of thermal fluctuations (Figure 5.2d). The influence of the microsphere size on the RMS of the microsphere center excursion is shown in Figure 5.4d for DNA tethers with L_C 1.1 kbp. Again the WLC and fWLC are both

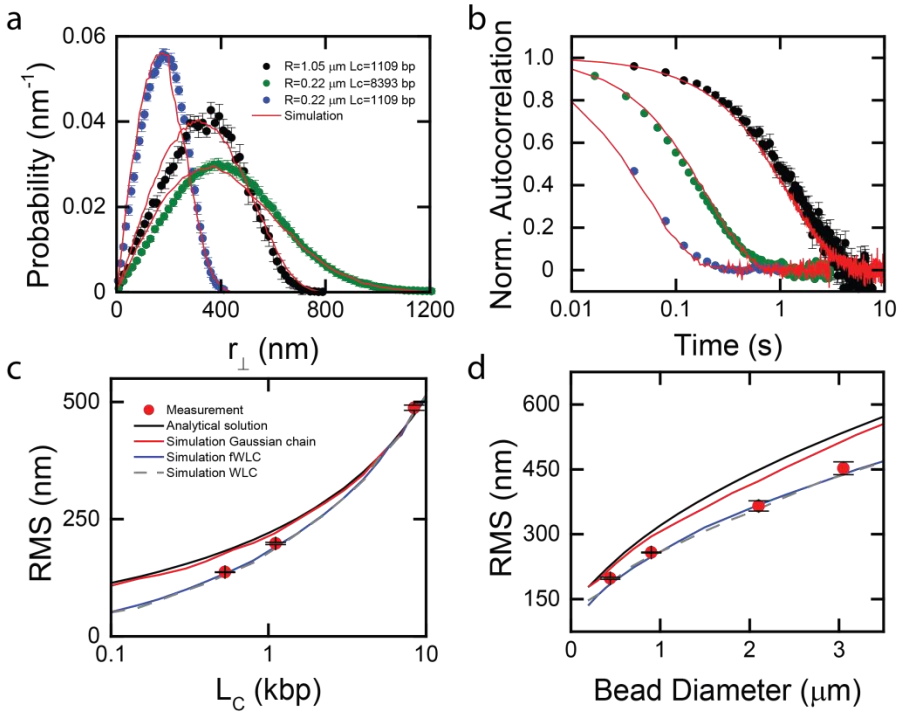

Figure 5.4 Measured and simulated TPM data. (**a**) The measured (using the fWLC model) and simulated probability distribution of the projected $r_\perp$ of the microsphere center for different DNA contour lengths and microsphere radii. (**b**) The measured (fWLC) and simulated normalized temporal autocorrelation. (**c**) The measured, simulated and analytically calculated RMS as function of DNA contour length using microspheres with a diameter of 440 nm. (**d**) The RMS versus microsphere diameter using DNA with a contour length of 1.1 kbp (~380 nm). Different DNA models have been used in the simulations in **c** and **d**. Both the WLC as the fWLC are able to describe the measured data correctly. Error bars are standard errors of the mean (s.e.m.) with $\langle n \rangle = 23$.

suitable to predict the measured data and the Gaussian-chain model predicts larger excursions. Our simulations are thus able to accurately describe TPM experiments for a large range of DNA lengths and microsphere radii, making them a universal tool for the characterization and calibration of TPM experiments.

5.3.2 Magnetic tweezers and flow-stretching simulations

Magnetic tweezers (MT) is a powerful and well-established single-molecule technique to apply forces to single tethered DNA molecules[5,6]. A common MT layout is shown in Figure 5.5a, with the magnetic-field lines parallel to the surface. Magnetic microspheres experience a magnetic gradient force directed towards the magnet. The permanent magnetic moment of the microspheres will align with the field lines, which prohibits microsphere rotation along the *y* and *z* axis[14]. In order to simulate microsphere motion in MT the axis of the field lines, the magnitude of the magnetic force and the position of the DNA-microsphere anchor point have to be defined. In Figure 5.5b, simulations of the motion of a tethered microsphere (2.69 μm DNA contour length, 2.8 μm microsphere diameter) subjected to various forces are presented. The data clearly shows that the microsphere is pulled away from the surface by the applied force and that microsphere fluctuations decrease with increasing force due to stiffening of the system. To validate our simulations we compared the mean variance of the *x*-position of the microsphere center of simulated data with experimental data and with theoretical calculations derived using the equipartition theorem (Figure 5.5c):

$$\langle \Delta x^2 \rangle = k_b T \langle z \rangle / F \qquad \textbf{Equation 5.8}$$

This formula is often used to calculate the applied force in magnetic tweezers experiments from the measured microsphere fluctuations[24]. This formula is not valid at low forces since it is derived using a perturbative approach assuming small fluctuations of the microsphere in comparison to the DNA length. Figure 5.5c clearly shows that, for this system, Equation 5.8 breaks down for forces below 0.1 pN and that our simulations are able to describe the experimental data over the full force range. Experimentalists using MTs in this low force regime should therefore be aware that forces derived using measured microsphere fluctuations might be incorrect. To ensure the forces of the measured data shown in Figure 5c are correct over the full range they were computed theoretically using numerical simulations of the magnetic field[24,25].

Magnetic tweezers in combination with flow-stretching is a powerful tool to perform force and fluorescence measurements on single molecules in a highly parallel fashion[7]. Using the viscous force applied on the microsphere by the buffer flow, the DNA is extended close to parallel to the glass surface, such that fluorescence can be recorded along the DNA. This is achieved by exerting a viscous flow force to the microspheres. The magnet is used to prevent the microspheres

from touching the surface to avoid sticking of the microspheres to the surface. In our simulations (DNA with 16.45 µm DNA contour length, 2.8 µm microsphere diameter) the magnetic force is kept constant (at 1 pN) while the flow is adjusted to vary the force ($F_{stokes} = 6\pi\eta Rv$). The shear flow velocity is determined using[26]:

$$v_x(z) = 4v_{max}\frac{z}{h_{ch}}\left(1-\frac{z}{h_{ch}}\right), \qquad \text{Equation 5.9}$$

with v_{max} is the maximum flow speed in the middle of the channel and h_{ch} is the height of the channel. Note, that there is a non-linear relation between the flow rate and the applied force (experimental forces were determined using equipartition theorem). Our model is able to predict this non-linearity well and also shows the influence of the position of the anchor point of the DNA to the bead (Figure 5.5e). This shows that even when the experimental setup has a perfectly uniform flow and there is no variation in microsphere size, there will still be a substantial spread and uncertainty in the applied force to each microspheres since for each microsphere the anchor point is randomly oriented with respect to the its magnetic moment[6]. We assume here that the torque exerted by the non-uniform flow is not enough to cause microsphere rotation and thereby affect microsphere alignment with respect to the magnetic field lines. In addition, in experiments the in-plane displacement of the microsphere relative to the DNA-surface anchor point position is used to determine the DNA's length. This is, however, not straightforward, since the DNA is not completely parallel to the surface (Figure 5.5d) and the angle between surface and DNA depend on the applied viscous force (the higher the force the smaller the angle) and position of the anchor point. Therefore, the experimental extension along the *x* dimension does not overlay with the eWLC model (Figure 5.5f). Using our simulations we can predict the relation between force and the *x* position of the microsphere center for different anchor points and obtain a deeper understanding of the impact of the variation in anchor point on the experimentally determined DNA length. The figure shows that the measured data lies within the force-distance range predicted by our simulation method, illustrating that our simulations can also be used characterize and calibrate these types of measurements.

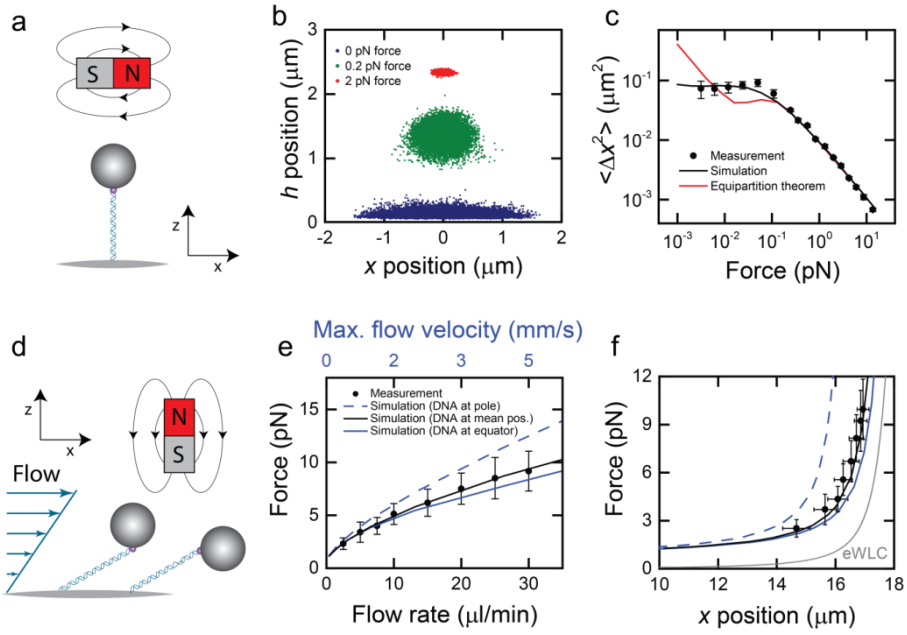

Figure 5.5 Measured and simulated MT and FS data. (**a**) Schematic of the magnetic tweezers configuration that was used to obtain data shown in **b** and **c.** In the measurements microspheres were selected that had a DNA anchor point close to the pole. (**b**) Scatter plot of simulated data of a DNA (L_c =2.69 μm) tethered microsphere (Ø 2.8 μm) subjected to different forces. At 0 pN the microsphere does not align with the magnetic field lines. (**c**) Mean variance in the x-position of DNA (L_c =2.69 μm) tethered microspheres (Ø 2.8 μm) obtained from measured data[14], simulated data and calculations using Equation 5.8. Error bars are s.e.m. with $\langle n \rangle = 5.4$. (**d**) Schematic of the flowstretching experiment that was used to obtain the data shown in **e** and **f,** indicating the two extreme DNA anchor point positions to the microsphere (the equator and the pole). The magnet prevents the magnetic microspheres from sticking to the surface during flowl. (**e**) The force subjected to flowstretched DNA (L_c = 16.45 μm) tethered microspheres (Ø 2.8 μm) as a function of flow rate (experimental) and maximum flow velocity (simulation). (**f**) The force versus the extension in the x-direction for measured and simulated data. A eWLC curve assuming the extension along the x-axis is shown as a reference. Error bars in **f** and **g** are s.e. with $n = 21$.

5.3.3 Surface friction and volume exclusion forces

We have validated with experimental data that our simulation method is able to describe a wide variety of microsphere-DNA tethered systems. With this validation in place we can now use our model to make predictions of the influence of different variables on the tethered microsphere which cannot be easily determined experimentally. An example is the influence of the no-slip boundary condition of the surface (Figure 5.6a,b). Experimentally it is not possible to change from a no-slip to a slip condition and therefore hard to investigate how this could affect the motion of a tethered microsphere used in typical TPM measurements. Our simulations show that the surface friction does not alter the distribution of the microspheres location, which is expected since the distribution only depends on the potential energy of the microsphere. The surface friction does cause the microsphere to move slower in close proximity of the surface, which decreases the autocorrelation time (Figure 5.6b). Segall et al.[9] have shown that due to the presence of the surface a purely entropic force emerges, repelling the tethered microsphere from the surface. The sphere in turn pulls on the DNA, which could influence, for instance, protein-induced DNA looping. We extracted this force using our model and compared in to the results of Segall et al. (Figure 5.6c). We observe that, especially for small contour lengths, the analytical estimation substantially underestimates the simulated volume-exclusion force. These results show that the volume exclusion effects of a microsphere in close proximity to a wall might be larger than previously estimated (~150 fN instead of ~50 fN for a 1.1 kbp DNA tethered microsphere with a diameter of 440 nm).

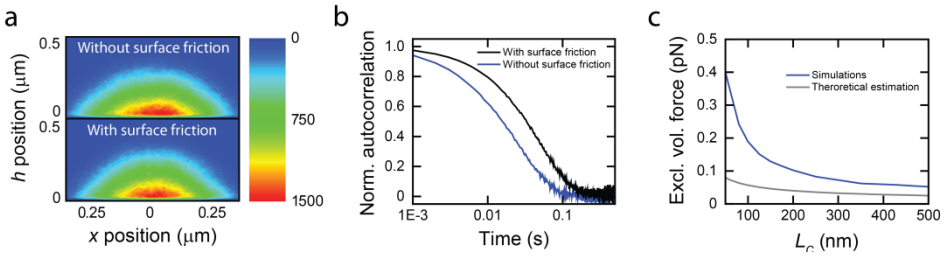

Figure 5.6 The influence of the no-slip boundary condition at the surface and the microsphere (diameter of 440 nm and DNA contour length of 1.1 kbp). (**a**) Position histogram of two simulated microsphere trajectories. In the upper panel no surface friction is taken into account. In the lower panel a no-slip boundary condition at the surface is assumed. (**b**) The normalized temporal autocorrelation of the microsphere with and without surface friction. With surface friction present the microsphere diffuses slower. (**c**) The mean simulated and analytically estimated excluded volume force as a function of DNA contour length.

5.4 Conclusion

In conclusion, we have shown a new simulation approach of the motion of tethered microsphere systems such as those used in tethered-particle motion, magnetic tweezers and flow-stretching experiments. No fitting parameters are used in our simulations, which makes them very suitable for use as calibration tool for these techniques and enables the extraction of additional information from experimental data. Furthermore, the method can be used to create insight in how external factors influence the motion of a tethered microsphere, such as surface friction (as shown in this study), temperature or viscosity of the medium, the Debye screening length or surface potential (surface type). Taken together, our simulation model can be used as a powerful tool for biophysicist to help interpret their data from tether particle experiments.

Acknowledgements

I would like to thank Aartjan te Veldhuis (University of Oxford), Jan Lipfert (Ludwig-Maximilian-University), Zhongbo Yu (TU Delft), Jacob Kerssemakers (TU Delft) and Nynke Dekker (TU Delft) for their collaboration and discussion on the magnetic tweezers data they provided.

Appendix A: Additional information

Hydrodynamic coefficients. The translational and angular motion of a spherical particle in close proximity to a plane wall in the limit of zero Reynolds number has been extensible studied and described by Luo et al[17]. For our simulations we assume a no-slip boundary condition at the surface of both the particle and the wall. Due to these no-slip effects the flow along the sphere will be non-uniform in contrary to the Stokes' flow in bulk medium. This causes: (i) a sphere translating parallel to a surface to experience a higher drag force compared to drag in bulk medium, (ii) a sphere translating parallel to a surface to experience a torque causing the sphere to make a rolling motion over the surface, (iii) a rotating sphere that has its axis of rotation parallel to a surface to experience an increased rotational drag compared to the drag in bulk medium and (iv) a rotating sphere that has its axis of rotation parallel to a surface in close proximity to experience a force causing the bead to translate parallel to the wall. These effects have been accounted for using the hydrodynamic coefficient vectors $\vec{\gamma}, \vec{\beta}, \vec{\zeta}$ and $\vec{\chi}$. Due to the symmetry of the system the radial vector components are similar:

$\gamma_x = \gamma_y \equiv \gamma_{x,y}$ (i), $\quad \chi_x = \chi_y \equiv \chi_{x,y}$ (ii),

$\beta_x = \beta_y \equiv \beta_{x,y}$ (iii), $\quad \zeta_x = \zeta_y \equiv \zeta_{x,y}$ (iv).

We used an 8th order polynomial fits of the simulated data of Luo et al. to extract the hydrodynamic coefficients as a function of microsphere height (Supplementary Figure 5.1).

The case of a translating sphere perpendicular to the surface and the case of a rotating sphere that has its axis of rotation perpendicular to the surface has not been described by Luo et al. Due to the symmetry of the system translation and rotation are not coupled in these dimensions. The sphere does, however, experience an increased translational and rotational drag due to the nearby surface. To calculate the increased translational drag coefficient as a function of sphere height we used the interpolation formula derived by Schäfer et al., which he showed to be accurate within 0.3% of the exact solution[20] (Supplementary Figure 5.2). For the rotational drag coefficient we used a 8th order polynomial to fit the exact solution derived by Jeffery et al.[27] (Supplementary Figure 5.2). Note that calculating the exact solution for every timestep in our simulation would increase computation times dramatically.

Appendix B: Supplementary Figures

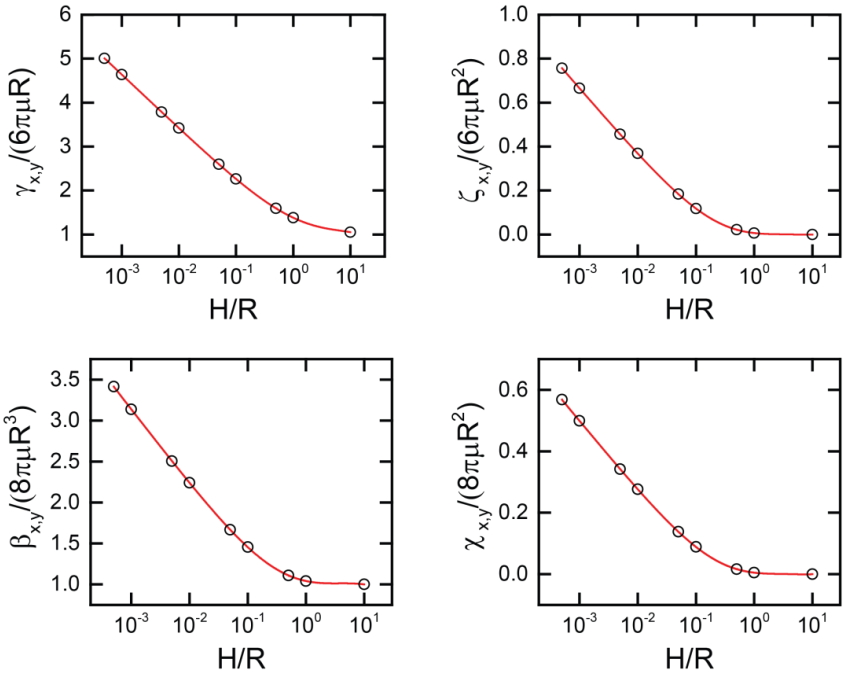

Supplementary Figure 5.8 The numerically derived drag coefficients by Luo et al (data points) which we fitted using 8th order polynomials (lines). Data has been normalized by the bulk drag coefficients $\gamma_0 = 6\pi\mu R$ and $\beta_0 = 8\pi\mu R^3$, which corresponds to Stokes drag with viscosity μ.

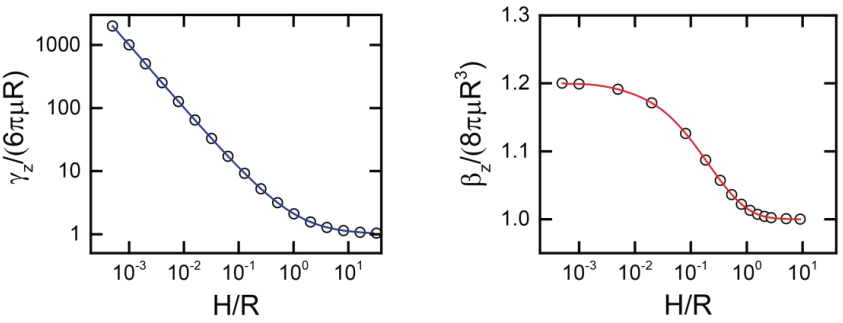

Supplementary Figure 5.2 The left panel shows the exact solution of γ_z (Brenner) calculated using equation 17 of ref[20] (data points) and the 12th order interpolation derived by Schäfer et al[20] (line). The right panel shows the exact solution of β_z using equation 12 of ref[27] (data points) and our 8th order polynomial fit (line). Data has been normalized by the bulk drag coefficients $\gamma_0 = 6\pi\mu R$ and $\beta_0 = 8\pi\mu R^3$. Note that the left panel has a logarithmic vertical axis.

References

1. Heller, I., Hoekstra, T. P., King, G. a, Peterman, E. J. G. & Wuite, G. J. L. Optical tweezers analysis of DNA-protein complexes. *Chem. Rev.* **114,** 3087–119 (2014).

2. Finzi, L. & Dunlap, D. D. Single-molecule approaches to probe the structure, kinetics, and thermodynamics of nucleoprotein complexes that regulate transcription. *J. Biol. Chem.* **285,** 18973–8 (2010).

3. Laurens, N. *et al.* Dissecting protein-induced DNA looping dynamics in real time. *Nucleic Acids Res.* **37,** 5454–64 (2009).

4. Sitters, G. *et al.* Acoustic force spectroscopy. *Nat. Methods* (2014). doi:10.1038/nmeth.3183

5. Gosse, C. & Croquette, V. Magnetic tweezers: micromanipulation and force measurement at the molecular level. *Biophys. J.* **82,** 3314–29 (2002).

6. De Vlaminck, I. & Dekker, C. Recent advances in magnetic tweezers. *Annu. Rev. Biophys.* **41,** 453–72 (2012).

7. Kim, S., Blainey, P. C., Schroeder, C. M. & Xie, X. S. Multiplexed single-molecule assay for enzymatic activity on flow-stretched DNA. *Nat. Methods* **4,** 397–9 (2007).

8. Leith, J. S. *et al.* Sequence-dependent sliding kinetics of p53. *Proc. Natl. Acad. Sci. U. S. A.* **109,** 16552–7 (2012).

9. Segall, D., Nelson, P. & Phillips, R. Volume-Exclusion Effects in Tethered-Particle Experiments: Bead Size Matters. *Phys. Rev. Lett.* **96,** 088306 (2006).

10. Towles, K., Beausang, J. & Garcia, H. First-principles calculation of DNA looping in tethered particle experiments. *Phys. …* **6,** 105–107 (2009).

11. Lindner, M., Nir, G., Vivante, A., Young, I. T. & Garini, Y. Dynamic analysis of a diffusing particle in a trapping potential. *Phys. Rev. E* **87,** 022716 (2013).

12. Reif, F. *Fundamentals of statistical and thermal physics*. (McGraw-Hill, 1985).

13. Beausang, J. F., Zurla, C., Sullivan, L., Finzi, L. & Nelson, P. C. Elementary simulation of tethered Brownian motion. 1–8 (2006).

14. Te Velthuis, A. J. W., Kerssemakers, J. W. J., Lipfert, J. & Dekker, N. H. Quantitative guidelines for force calibration through spectral analysis of magnetic tweezers data. *Biophys. J.* **99,** 1292–302 (2010).

15. Purcell, E. M. Life at low Reynolds-number. *Am. J. Phys.* **45,** 3–11 (1977).

16. Kezirian, M. T. *Hydrodynamics with a wall-slip boundary condition for a particle moving near a plane wall bounding a semi-infinite viscous fluid*. (Massachusetts Institute of Technology, 1992).

17. Luo, H. & Pozrikidis, C. Effect of surface slip on Stokes flow past a spherical particle in infinite fluid and near a plane wall. *J. Eng. Math.* **62,** 1–21 (2007).

18. Risken, H. *The Fokker-Plank Equation. Methods of Solution an Applications*. (Springer Berlin Heidelberg, 1989).

19. Grassia, P. S., Hinch, E. J. & Nitsche, L. C. Computer-simulations of Brownian-motion of complex-systems. *J. Fluid Mech.* **282,** 373–403 (1995).

20. Schäffer, E., Nørrelykke, S. & Howard, J. Surface forces and drag coefficients of microspheres near a plane surface measured with optical tweezers. *Langmuir* **287,** 3654–3665 (2007).

21. Seol, Y., Li, J., Nelson, P. C., Perkins, T. T. & Betterton, M. D. Elasticity of short DNA molecules: theory and experiment for contour lengths of 0.6-7 microm. *Biophys. J.* **93,** 4360–73 (2007).

22. Odijk, T. Stiff chains and filaments under tension. *Macromolecules* **28,** 7016–7018 (1995).

23. Han, L. *et al. Calibration of Tethered Particle Motion Experiments. Math. DNA Struct. Funct. Interact.* **150,** 123–138 (Springer New York, 2009).

24. Strick, T. R., Allemand, J., Bensimon, D., Bensimon, A. & Croquette, V. The Elasticity of a Single Supercoiled DNA Molecule. *Science (80-.).* **271,** 1835–1837 (1996).

25. Lipfert, J., Hao, X. & Dekker, N. H. Quantitative modeling and optimization of magnetic tweezers. *Biophys. J.* **96,** 5040–9 (2009).

26. Williams, K. *et al.* A single molecule DNA flow stretching microscope for undergraduates. *Am. J. Phys.* **79,** 1112 (2011).

27. Jeffery, G. On the steady rotation of a solid of revolution in a viscous fluid. *Proc. London Math. …* 327–338 (1915).

6 Optical Pushing

The ability to measure and manipulate single-molecules has greatly advanced the field of biophysics. Yet, the addition of more single-molecule tools that enable one to measure in a highly parallel fashion is important in order to diversify the questions that can be addressed. Here, we present optical pushing (OP), a novel bionano-sensing method to exert forces on many individual biomolecules tethered to microspheres using a single collimated laser beam. Forces ranging from a few femtonewtons to several piconewtons can be applied with a sub-millisecond response time. To determine forces exerted on the tethered particles by the laser, we analyzed their measured Brownian motion using a newly derived analytical model and numerical simulations. In the new model, Brownian rotation of the microspheres is taken into account, which proved to be a critical component to correctly determine the applied forces. We used our novel OP technique to map the energy landscape of the protein-induced looping dynamics of DNA. OP can be used to apply loading rates in the range of 10^{-4} to 10^{6}pN/s to many molecules at the same time, which makes it a tool suitable for dynamic force spectroscopy.

Based on: Gerrit Sitters*, Niels Laurens*, Emile J de Rijk, Holger Kress, Erwin J G Peterman & Gijs J L Wuite, Optical Pushing: A tool for highly parallelized bionano-sensing (not published yet)

6.1 Introduction

Single-molecule techniques such as tethered-particle motion (TPM)[1], magnetic tweezers (MTs)[2], optical tweezers (OTs)[3], biomembrane-force probe (BFP)[4], centrifuge force microscopy (CFM)[5] and atomic force microscopy (AFM)[6] have greatly advanced our ability to quantify the mechanical properties, dynamics and interactions of biological macromolecules[7–9]. Dynamic force spectroscopy, an approach in which molecular interactions are subjected to various loading rates in order to quantify their energy landscapes, is a particularly popular approach in biophysics[4]. Many single-molecule methods probing one molecule at a time are limited by low experimental throughput, which makes obtaining statistical information over many molecules and identifying rare events challenging. Techniques such as TPM, MTs and CFM tackle this problem by measuring multiple single molecules in parallel. All these techniques, however, have their limitations: in TPM no forces are applied, in CFM and MTs constant forces are applied that can only be varied on a time scale of seconds. Here we present a novel bionano-sensing method that combines high throughput with rapid force application: optical pushing (OP). OP uses the momentum of laser-generated photons to apply tensions of up to several piconewtons per Watt to multiple DNA molecules tethered between a surface and microspheres.

6.2 Results

6.2.1 Experimental setup

In our implementation of OP, we used a single, collimated laser beam, coupled into an inverted microscope to apply controlled forces to multiple microsphere-tethered biomolecules distributed over a field of view with a size of tens of micrometers. The setup (Figure 6.1) contained three sets of components: (i) the optical pathway of the laser, (ii) the flow cell with sample, and (iii) the imaging pathway. (i) As source of radiation pressure a collimated laser beam was used with wavelength 1070 nm, maximum power 20W (power regulation was achieved by a combination of a half-wave plate and a polarizing beam splitter), and beam diameter ~70 μm (FWHM, generated using a telescope consisting of an achromatic lens (focal length 150mm) and an aspherical lens (focal length 4 mm)). (ii) The flow cell with sample chamber

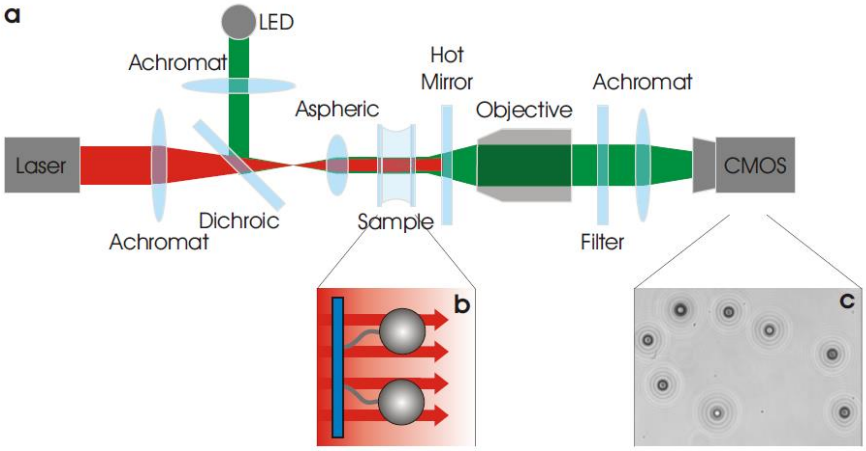

Figuur 6.1 Schematic drawing of the setup. (a) a 1070 nm laser that is used to apply an optical force to microspheres in the sample. Behind the sample, the beam is reflected back using a hot mirror, to prevent heating the imaging objective. LED light is used to image the microspheres. LED light is transmitted through the hot mirror and imaged on a CMOS camera. (b) Biomolecules are tethered to the surface and attached to microspheres. (c) Example image of the CMOS camera (25 Hz, 40 ms integration time). The radial ring patterns around the microsphere images are used to determine their height.

consisted of a quartz microscope slide and a quartz cover slip separated by parafilm spacers. Quartz was used to minimize sample heating by the laser. Functionalized molecules were attached to both the surface and the microspheres (Figure 1b)[9]. (iii) For imaging a 455 nm light emitting diode (LED) was used, coupled into the aspherical lens using a dichroic mirror. The light transmitted by the sample was collected with an air microscope objective (50X NA0.42) and imaged, using the tube lens of the microscope, on a CMOS camera (Figure 1c), which allowed taking images with a frame rate of 25 Hz (full frame). An IR neutral density filer was placed in front of the camera, to remove remaining laser light. The particles in the images were tracked in three dimensions using a cross-correlation algorithm (x, y), and by comparing the measured radial profile against a database of calibrated radial-profiles, made at known heights (z). This resulted in a 3D sub-pixel precision of < 2 nm in x, y and < 5 nm in the z (Supplementary Figure 6.1). For stable use of OP it

was essential to avoid heating of the objective by the laser, which induced drifting aberrations in the acquired images. The heating was minimized by redirecting the laser light after interacting with the sample, before entering the imaging objective, using a hot mirror back into the sample. Because of the divergence of the Gaussian laser beam the radiation pressure due to the reflected laser light was more than 1 order of magnitude weaker than due to the direct light.

6.2.2 OP applied to tethered DNA

In order to demonstrate that OP is suitable for the manipulation of tethered molecules, we investigated the restriction of three-dimensional Brownian motion of a single, DNA-tethered (1.1 kilobasepairs) microsphere (Ø 2.10 µm polystyrene) (Figure 6.2). When a laser power of 1.6 Watt was applied to the sample, the random motion of the microsphere in all three dimensions was restricted. In addition, the distance of the microsphere with respect to the surface (*z*) increased. Both observations indicate that the radiation pressure of the laser beam actively pushed the microsphere away from the surface. Note that the microsphere found its new equilibrium position, within one camera frame demonstrating that OP allows switching on and off forces faster than 40ms (acquisition time of a single camera frame).

6.2.3 Force calibration

In order to assess the performance of OP the forces exerted on the biomolecules were determined, by measuring and analyzing the Brownian motion of the microspheres. Apart from translational Brownian motion the microspheres also underwent rotational Brownian motion, which caused them to swivel around their attachment points (supplementary Figure 6.2). Because of this swiveling motion, current force-calibration methods for tethered microspheres, as used for e.g. MTs, are not directly applicable to our system[10]. In MTs, the paramagnetic microspheres have a fixed alignment with respect to the external magnetic field, which allows neglecting Brownian rotation[11]. In the absence of this fixed alignment, the swiveling of the microsphere increases its motion, leading to an underestimation of the force up to 10% if the swiveling is not taken into account (with DNA tethers short compared to te microsphere radius, supplementary Figure 6.3). Solving the linearized system of Langevin equations for translation and rotation (Equations 6.1 and 6.2)[12,13], under the assumption that the exerted force is substantially larger than the thermal fluctuations, yielded an analytical expression for the power

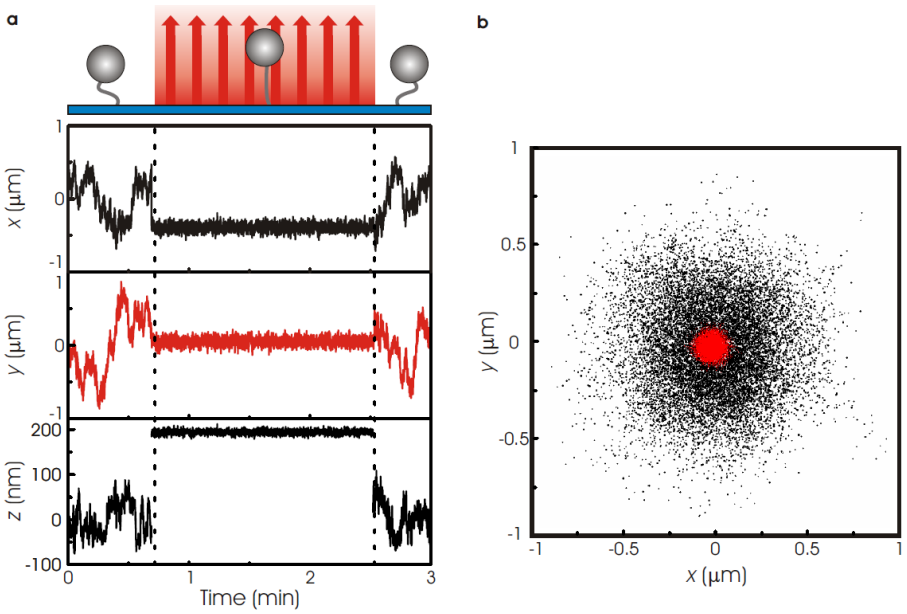

Figuur 6.2 Proof of principle of optical pushing.(**a**) Raw motion trace of a DNA (1.1 kbp) tethered microsphere (ϕ 4.26 μm) when the laser is off and set to 2 W (between dashed lines). The motion of the microsphere is quenched in all three dimensions when the laser is on. (**b**) A x,y-scatter plot of the beads position when the laser is off (black) and set to 2 W (red).

spectrum of the microsphere's motion in *x*- and *y*-directions (Equation 6.3) (see Appendix A for derivation):

$$m\frac{d\vec{v}}{dt} = \vec{F}_{brown}(t) - \vec{\gamma}\vec{v}(t) + \vec{F}_{ext}(t) \qquad \text{Equation 6.1}$$

$$I\frac{d\vec{\omega}}{dt} = \vec{T}_{brown}(t) - \vec{\beta}\vec{\omega}(t) + \vec{T}_{ext}(t)\,, \qquad \text{Equation 6.2}$$

$$P(f) = 2k_bT\frac{(\beta+\gamma\langle z\rangle^2)R^2F^2+(\langle z\rangle-R)^2\beta^2\gamma(2\pi f)^2}{\left((R-\langle z\rangle)\beta\gamma(2\pi f)^2+RF^2\right)^2+(2\pi f(R\gamma\langle z\rangle-\beta)F)^2}. \qquad \text{Equation 6.3}$$

In Equations 6.1 - 6.3, m is the mass of the microsphere, $\vec{v}$ its velocity, $\vec{F}_{brown}$ the random Brownian force, $\vec{\gamma}$ the effective translational drag coefficient, $\vec{F}_{ext}$ the external forces acting on the microsphere, I the microsphere's moment of inertia, $\vec{\omega}$ its angular velocity, $\vec{T}_{brown}$ the random Brownian torque, $\vec{\beta}$ the effective

rotational drag coefficient, $\vec{T}_{ext}$ the external torques acting on the particle, k_b Boltzmann's constant, T the temperature, $\langle z \rangle$ the average microsphere height, R the microsphere radius, F the exerted laser force and f the frequency. To confirm the validity of our analytical solution we compared it to simulations. Simulated data was obtained by implementing an initial microsphere position and rotation, and recursively solving Equation 6.1 and 6.2 (for full derivation see Appendix A) using randomly varying instantaneous Brownian forces and torques. The difference between the simulated data and the analytically obtained restoring force and torque data (red) lies within a few percent (Supplementary Figure 6.2c). Moreover, the analytical solution of the power spectrum (Equation 6.3) agrees with the power spectra of simulated data traces (Supplementary Figure 6.2d), for forces $F_{laser} \gg F_{brown}$, confirming that our new rotational model is a suitable calibration method for the optical force acting on the biomolecules.

With a calibration method in place, we validated OP and determined what forces could be obtained. Power spectra of DNA tethers attached to microspheres of two different sizes were obtained as a function of laser power and fitted using Equation 6.3 (Figure 6.3). For both microsphere sizes a linear dependency of force on total laser power was obtained, as expected from the linear dependence of radiation pressure on light intensity (Figure 6.3b). Moreover, the measured forces match theoretical predictions based on Mie scattering theory[14]. These measurements demonstrate that our OP instrument is capable of applying forces up to 2.6 pN/Watt to 4.26 µm microspheres. It is important to note that the maximum measured pushing force ~15 pN is limited by the strength of the dig-antiDIG interaction used to attach the DNA to the surface, not by a physical constraint of our approach. These forces are not as high as forces obtained using OTs on similar microspheres (typically in the order of 100 pN/Watt[8]). In OP, the maximum force can be readily increased by using different microsphere sizes or composition. Mie scattering theory predicts that the force is approximately 4-fold higher when gold-coated (instead of bare) polystyrene microspheres are used (Supplementary Figure 6.4). Our setup also allows sampling of smaller microspheres and lower forces. Our linearized model, however, does not allow correct determination of forces that are close to the Brownian force (< 150 fN) (Figure 6.3c). At these low forces, the force can be calibrated accurately by determining the root mean square (RMS) displacement of the microspheres and comparing that with simulated data using the full kinetic model based on Equations 6.1 and 6.2 . Using this approach, OP forces were determined accurately for 440 nm diameter microspheres to be 10.6 fN/Watt at the sample (Figure 6.3d), again in agreement with Mie theory.

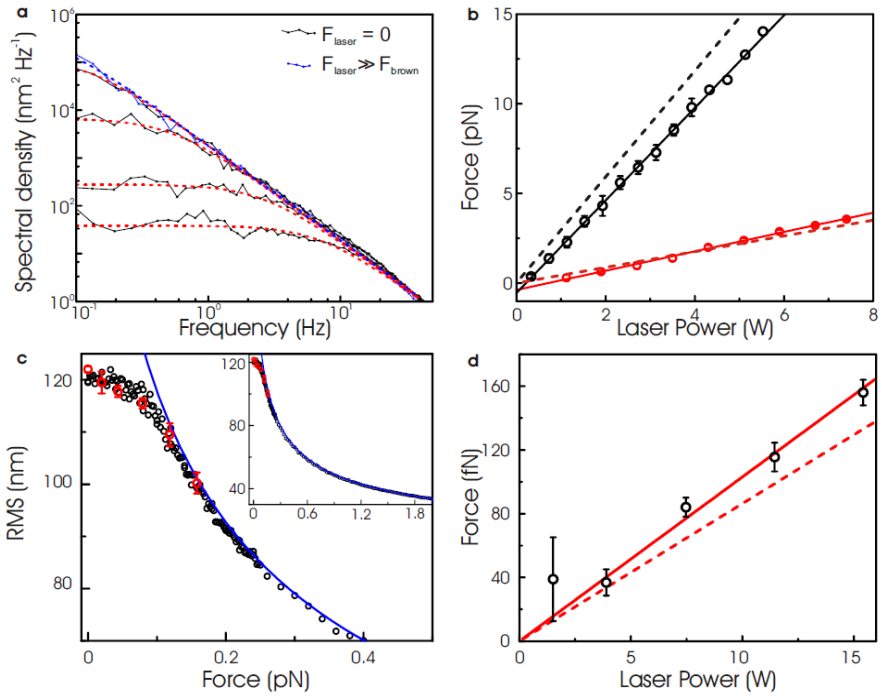

Figuur 6.3 Force calibration of OP. (**a**) Fitted power spectra of the measured x,y, motion of tethered microspheres. A power spectrum obtained in the absence of force (blue) is shown for reference. (**b**) Exerted optical pushing force as a function of total laser intensity at the sample. Forces are determined by fitting the power spectra of measured polystyrene tethers with the analytical theory, error bars indicate s.e.m. (ϕ 4.26 µm, and ϕ 1.84 µm in black and red respectively). Solid lines represent linear fits yielding slopes of 2.6 ± 0.1 pN W^{-1} (black) and 0.5 ± 0.1 pN W^{-1} (red). Dotted lines represent the Mie theory predictions. (**c**) RMS motion of small (ϕ 440 nm) microspheres. Measurements (red), fitted simulated data using our full model (black) and our analytical model (Eq. 6.3, blue). (**d**) The derived force, using the RMS fitted data sets, as a function of applied laser power. The linear fit (solid line) yielded a slope of 10.6 fN/Watt and the dotted line represents Mie theory predictions.

6.2.4 Manipulating protein looped DNA

To demonstrate the power of OP in bionano-technological applications, we performed a force-spectroscopy study of protein-induced DNA looping. DNA loops occur whenever proteins interact with multiple sites on the same DNA molecule[15]. Loops have both organizing and regulatory functions in processes such as DNA replication, repair, transcription, and cleavage[16,17]. We chose the well-studied Type II restriction endonuclease FokI as our model system[18–20]. Two FokI monomers each bind to distinct recognition sites on the DNA ('5-GGATG-3'), subsequently they associate in dimers, while both monomers remain attached to the DNA, forming a DNA loop[18]. When only Ca^{2+} (and not Mg^{2+}) is present in solution as a cofactor, the restriction enzymes specifically bind to the DNA, forming loops, but they cannot cut the DNA[21,22]. Looping of multiple DNA molecules containing two FokI recognition sites was monitored in real time using our OP microscope. Excursions of DNA-tethered microspheres depend on the length of the DNA and, as a consequence, loop formation can be observed as a decrease in the microspheres' RMS motion. In the current study we only analyzed the transition from looped to unlooped state, which occurs in a single kinetic step. The opposite transition, from unlooped to looped state, consists of two distinct, subsequent kinetic steps, one of which depends on protein concentration and tether activity, and is therefore far more complex to interpret (Figure 6.4a)[19].

Example OP time traces of the RMS displacement in the presence of FokI are shown in Figure 6.4b. The RMS motion of each microsphere was calculated as described by Laurens *et al.*[19]. When the laser is off, the system stochastically switched between the unlooped and looped state. With increasing laser intensity, and thus increased force applied to the DNA tether, loop formation was less frequent (Figure 6.4b) and loops lasted for shorter times (Figure 6.4c). Measurements on multiple microspheres simultaneously enhanced experimental throughput (Supplementary Figure 6.5) and allowed obtaining the force dependence of the average loop lifetime t_{loop} (Figure 6.4c). This lifetime decayed exponentially with force, as expected from Arrhenius' law $t_{loop} = 1/k_0 \exp(F \cdot \Delta x / k_B T)$ (with k_0 the unlooping rate at zero force and Δx the distance to the barrier along the direction at which the force F is applied). The single-exponential decay indicates that the transition from looped to unlooped state involves a single kinetic step. From the fit, a zero-force unlooping rate (k_0) of $0.15 \pm 0.01 \mathrm{s}^{-1}$ was obtained, in agreement with earlier measurements[19]. In addition, a length change from looped state to transition state (Δx) of 75 ± 2 nm was obtained. This length change is relatively

large since it exceeds the size of the protein by at least one order of magnitude, which demonstrates that only very small forces, in the femtonewton range, are required to disrupt the DNA looping. At these low forces the DNA is in a coiled state, in this entropy dominated state the DNA end-to-end length reacts highly elastic to applied forces. Hence, this apparent DNA elasticity attributes significantly to Δx since we pull on the loop via the two elastic DNA arms extending from it. Because the volume-exclusion effect is in the same order of magnitude as the bond strength it is important to correct the unlooping rate at zero force for this volume-exclusion effect, which, in turn is dependent on the size of the microspheres and the interactions with the surface. In our setup the volume-exclusion effect generates an effective force on the DNA of about 52 fN in the looped state[23]. Under the assumption that the volume-exclusion force acts as a constant force offset, correction reduces the unlooping rate by a factor of ten, $k_{0,cor} = 0.015 \pm 0.003\ s^{-1}$. Apart from the looping rate, also the looped fraction was be obtained from the data, which allowed calculation of the force dependence of the free energy change from the unlooped to the looped state (Supplementary Figure 6.6). This approach yielded a standard free energy change ΔG^0 of 0.7±0.1 k_BT (with the unlooped state having a lower free energy). However, this ΔG^0 needs to be corrected because the volume-exclusion effect introduces an energy penalty for loop to occur. When we correct for this it yields a ΔG^0_{cor} of -0.6±0.4 k_BT i.e. leading to the expected situation in which the looped state having a lower free energy. The low forces that are needed to disrupt the protein induced DNA loops indicate that thermal fluctuations are sufficient to cross the energy barrier from looped to unlooped state and vice versa, which from a biological point of view makes sense since restriction enzymes function is to recognize and cut specific sequences within a few seconds and not to mechanically stabilize DNA loops for longer time periods[19]. This determination of energetics and kinetics of the FokI restriction enzyme demonstrates the great level of control OP provides in the femtonewton force regime, allowing the extraction of subtleties in the energy landscapes of molecular interactions as well as the characterization of the impact of surfaces on bond formation (Figure 6.4d).

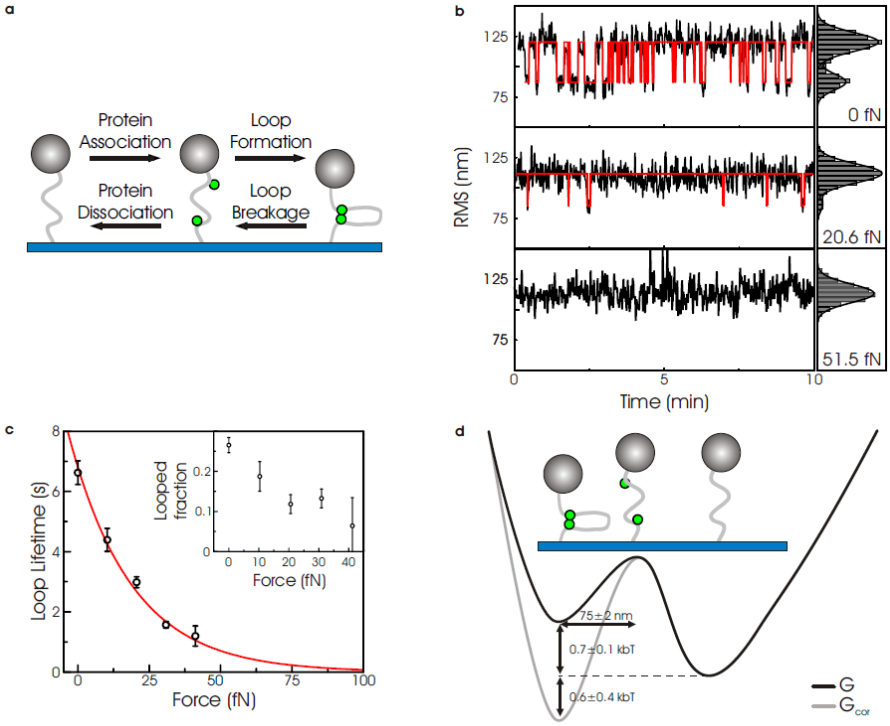

Figuur 6.4 Manipulating protein induced DNA loops with OP. (**a**) Kinetic scheme of protein-induced DNA looping. (**b**) Time traces of the root mean square (RMS) motion of a single DNA tether (left panel, black line), and the corresponding histograms (right panel), with increasing optical pushing force. The histograms show two distinct states corresponding to the unlooped (large RMS) and looped state (small RMS). From the histograms a threshold value is obtained, which is used to determine the dwell times (red lines, left panels). (**c**) Average loop lifetime plotted as a function of optical pushing force. Black circles: experimental data points (error bars s.e.m.), red line: fit using Arrhenius' law, inset: looped fraction as a function of the optical pushing force (error bars s.e.m.). (**d**) Energy landscape obtained from the force spectroscopy measurements.

6.3 Discussion and Conclusion

We have characterized the performance of our novel OP method and shown its potential by unraveling the energey landscape of the DNA-looping FokI restriction enzyme by the use of constant force measurements. Apart from applying a constant force, OP is capable of rapidly switching and changing forces, by shuttering or strobing the incoming light, or varying the intensity using for example an acousto-optical modulator. This allows OP to apply a wide dynamic range of loading rates, as is required for dynamic force spectroscopy[4]. Radiation pressure travels at the speed of light, the theoretical response time of a typical DNA-tethered microsphere is, however, limited by viscous drag (slowing down the motion of the microsphere and thus the extension of the loading of the tether) to typically about 100 µs (see supplementary information). From this we estimate that OP can be used to apply linear force ramps in the range of 10^{-4} to 10^{6} pN/s to DNA (Supplementary Figure 6.7). Current MT systems allow access to a more limited range of loading rates from 10^{-4} to 10^{2} pN/s [24]. Finally, it should be noted that one does need to take care of sample heating caused by the high laser powers used. We were able to reduce heating substantially effects by using quartz microscope slides and coverslips. To calibrate the forces in OP, we derived an analytical description of the power spectrum taking into account Brownian rotation of the tethered microspheres (Equation 6.3). We note that our equation can be used more generally to tethered systems (including MTs) as long as the externally applied force on the microsphere dominates the Brownian force i.e. $F_{ext} \gg F_{brown}$. Supplementary Figure 6.3 shows how the analytical power spectrum derived here compares to the MT power spectrum used by Velthuis *et al*.[11] for the dimension perpendicular to the direction of the field lines:

$$P(f) = \frac{2\gamma k_b T}{\gamma^2 (2\pi f)^2 + (F/(L_{ext}+R))^2}. \qquad \text{Equation 6.4}$$

The MT model only holds for tethered microspheres with a diameter that is smaller than the contour length of the DNA (Supplementary Figure 6.3c); for larger diameters the model underestimates the Brownian motion of the microsphere (Supplementary Figure 6.3a,b). In contrast, our new model was able to describe the Brownian motion for the larger microspheres; it fails, however, for external forces lower than the Brownian force (< 0.1 pN). We have shown that the Brownian motion can be predicted accurately in this low-force regime (down to ~30 femtonewton) with numerical simulations. By making use of the analytical solution (Equation 6.3) for the enthalpic regime (> 0.1 pN) and the numerical simulations in

the entropic regime (< 0.1 pN) we were able to predict microsphere motion subjected to forces that are biophysically relevant. Due to its generality applicability our model is not constrained to OP alone, but is also applicable to other microsphere-tether systems such as MTs and TPM.

To conclude, we have shown that a collimated laser beam can be used to apply a force to multiple biomolecules in parallel (Supplementary Figure 6.5). We have demonstrated the feasibility of OP as a flexible (dynamic) force spectroscopy technique. In future implementations, improvements can be made, inspired by other force-spectroscopy approaches. For example, spatial light modulators[21,27] could be used to flatten the light intensity, the number of usable tethers could be increased by printing antibodies in a periodic pattern on a coverslip[28], (sub)millisecond dynamics of weak DNA-enzyme interactions could be imaged using integrated fluorescence microscopy[28,29], or the polarization of the laser light could be employed to control the torque acting on the biomolecules[30,31]. Finally, OP instruments can be readily implemented in any existing OTs instrument: placing a single lens, converting a collimated beam in one focused in the back-focal plane of the microscope objective, will convert an OTs into an OP apparatus.

Appendix A: Additional information

The analytical model. To determine the exerted force on tethered molecules it is important to understand the motion of the system. Apart from translational Brownian motion the microspheres also experiences rotational Brownian motion causing them to swivel around the attachment point as shown schematically for one dimension in Supplementary Figure 6.2a,b. Existing force calibration methods for tethered microspheres, which are used for instance for MT, are not directly applicable to our system. Microsphere rotation is neglected in these models because of the fixed alignment of the paramagnetic microsphere with the external magnetic field[11]. Neglected microsphere rotation leads to an underestimation of the applied force (Supplementary Figure 6.3). We therefore derived a power spectrum for the microspheres motion parallel to the surface using the Langevin equation for both the translation as the rotation[12,13]:

$$m\frac{d\vec{v}}{dt} = \vec{F}_{brown}(t) - \vec{\gamma}\cdot\vec{v}(t) + \vec{F}_{ext}(t)\,, \qquad \text{Equation 6.5}$$

$$I\frac{d\vec{\omega}}{dt} = \vec{T}_{brown}(t) - \vec{\beta}\cdot\vec{\omega}(t) + \vec{T}_{ext}(t)\,, \qquad \text{Equation 6.6}$$

where $\vec{v}$ and $\vec{\omega}$ are respectively the translational and angular velocity, m is the particle mass and I is the moment of inertia of the particle. The forces due to the laser, the tether, the surface, buoyancy and gravity are included in the external force term $\vec{F}_{ext}$ and are described in detail bellow. Equations 6.5 and 6.6 account for the increased viscous drag near the surface, using Faxen's law for both the translation and rotation coefficients $\vec{\gamma}$ and $\vec{\beta}$ (see section surface effects, Equations 6.20-6.23. The external torque $\vec{T}_{ext}$ results from the cross product of the vector between the microsphere center and the DNA attachment point $\vec{R}$ and the DNA force $\vec{F}_{DNA}$ (Supplementary Figure 6.2b). $\vec{F}_{brown}$ and $\vec{T}_{brown}$ are the fluctuating thermal force and torque. The amplitude of these terms are described by the fluctuation-dissipation theorem and are Gaussian distributed with the following statistical properties[32]:

$$\langle F_{brown}(t)\rangle = 0, \qquad \text{Equation 6.7}$$

$$\langle T_{brown}(t)\rangle = 0, \qquad \text{Equation 6.8}$$

$$\langle F_{browm}(t')F_{browm}(t'+t)\rangle = 2\gamma k_B T\delta(t), \qquad \text{Equation 6.9}$$

$$\langle T_{browm}(t')T_{browm}(t'+t)\rangle = 2\beta k_B T\delta(t). \qquad \text{Equation 6.10}$$

With $\delta(t)$ the Dirac delta function. The inertial terms in equations (6.5) are neglected since the Reynolds number is sufficiently low. For microspheres in the micro range the Reynolds number is in the order of $1 \cdot 10^{-3}$ at room temperature (Table 6.1).

To simplify calculations we assume a laser force $F_{laser} \gg F_{brown}$, leading to small angles of θ, α, φ, β and ξ (Supplementary Figure 6.2a,b). The DNA-microsphere system is in equilibrium when the DNA and vector $\vec{R}$ are aligned with the z axis. If the system is pulled out of equilibrium due to Brownian fluctuations the DNA and the laser force will tend to force the microsphere back into equilibrium:

$$F_{restoring,x} = F_{DNA} \cdot \sin\theta, \qquad \text{Equation 6.11}$$

$$T_{restoring,y} = |R| \cdot |F_{DNA}| \cdot \sin\beta. \qquad \text{Equation 6.12}$$

Assuming that $|F_{DNA}| = |F_{laser}|$ (for $\theta \ll 1$), $|\varphi| + \alpha + \xi \ll 1$ and $x_{cm} = x_{DNA} + R\varphi$ (see Supplementary Figure 6.2a,b for the parameters) we derive the following linearized versions of equations (6.7):

$$F_{restoring,x} = F_{laser} \cdot \frac{x_{DNA}}{z-R}, \qquad \text{Equation 6.13}$$

$$\begin{aligned} T_{restoring} &= |R| \cdot |F_{laser}| \cdot \sin(\pi - |\varphi| - \alpha - \xi) \\ &= |R| \cdot |F_{laser}| \cdot \left(|\varphi| + \frac{x_{cm}}{z} + \frac{Rx_{cm}}{z^2 - zR} + \frac{R|\varphi|}{z-R}\right). \end{aligned} \qquad \text{Equation 6.14}$$

See Supplementary Figure 6.2c how they compare to the non-linearized force and torque (using the numerical simulations described below). To calculate the power spectrum of equations (6.6) we implement the linearized restoring force and torque as the external force and torque in these equations and calculate the Fourier transform, with $\tilde{x}(\omega) = \int_{-\infty}^{\infty} x(t)e^{-i\omega t}dt$. Note that surface, buoyancy and gravity forces are neglected:

$$\tilde{F}_{brown} = i\omega\gamma\tilde{x}_{cm} - \frac{F_{laser}}{z-R}(\tilde{x}_{cm} - R\tilde{\varphi}), \qquad \text{Equation 6.15}$$

$$\tilde{T}_{brown} = i\omega\beta\tilde{\varphi} - RF_{laser}\left(|\tilde{\varphi}| + \frac{\tilde{x}_{cm}}{z} + \frac{R\tilde{x}_{cm}}{z^2 - zR} + \frac{R|\widetilde{\varphi}|}{z-R}\right). \qquad \text{Equation 6.16}$$

From these equations we derive the power spectrum $P(f) \equiv \langle \tilde{x}_{cm} \tilde{x}_{cm}^{*} \rangle$, with the frequency f (* denotes the complex conjugate), using the relations $\langle \tilde{F}_{brown}^{2} \rangle = 2\gamma k_B T$ and $\langle \tilde{T}_{brown}^{2} \rangle = 2\beta k_B T$:

$$P(f) = 2k_b T \frac{(\beta+\gamma\langle z\rangle^2)R^2F^2+(\langle z\rangle-R)^2\beta^2\gamma(2\pi f)^2}{\left((R-\langle z\rangle)\beta\gamma(2\pi f)^2+RF^2\right)^2+(2(R\gamma\langle z\rangle-\beta)F\pi f)^2}. \qquad \text{Equation 6.17}$$

Note that the equation (6.10) reduces to the power spectrum of magnetic tweezers when $\beta = 0$ (neglecting rotation) is implemented (equation 6.4).

Numerical simulations. To validate the assumptions made in the derivation of the analytical power spectrum we also simulated microsphere movement. The microsphere equation of translation and rotation was solved numerically using the following equations:

$$\vec{x}_{n+1} = \vec{x}_n + \vec{\gamma}^{-1} \cdot \left(\vec{F}_{ext} + \vec{F}_{brown}\right)\Delta t, \qquad \text{Equation 6.18}$$

$$\vec{\varphi}_{n+1} = \vec{\varphi}_n + \vec{\beta}^{-1} \cdot \left(\vec{T}_{ext} + \vec{T}_{brown}\right)\Delta t, \qquad \text{Equation 6.19}$$

where $\vec{x}_n$ and $\vec{x}_{n+1}$ is the microspheres three dimensional position at the step n and $n+1$ of the simulation respectively. $\vec{\varphi}_n$ and $\vec{\varphi}_{n+1}$ denote the microspheres orientation. In order to simulate the microspheres trajectory we implemented an initial microsphere position and rotation, after which successive positions and rotations were calculated using Equations 6.18 and 6.19. The Brownian force and torque terms were drawn from Gaussian distributions that suffice Equations 6.7-6.10 where the Dirac delta distribution was set to $\delta(t) = 1/\Delta t$, with Δt the time step of the simulation for which we typically used 10^{-5}s. Decreasing Δt did not affect the statistical properties of the simulated traces.

Surface effects. Equations 6.5 and 6.6 account for the increased viscous drag near the surface, using Faxen's law for both the translation and rotation coefficients for the parallel and perpendicular direction relative to the surface[33]:

$$\gamma_x = \gamma_y = \frac{\gamma_0}{1-\frac{9}{16}\left(\frac{R}{z}\right)+\frac{1}{8}\left(\frac{R}{z}\right)^3-\frac{45}{256}\left(\frac{R}{z}\right)^4-\frac{1}{16}\left(\frac{R}{z}\right)^5}, \qquad \text{Equation 6.20}$$

$$\gamma_z = \frac{\gamma_0}{1-\frac{9}{8}\left(\frac{R}{z}\right)+\frac{1}{2}\left(\frac{R}{z}\right)^3-\frac{57}{100}\left(\frac{R}{z}\right)^4+\frac{1}{5}\left(\frac{R}{z}\right)^5+\frac{7}{200}\left(\frac{R}{z}\right)^{11}-\frac{1}{25}\left(\frac{R}{z}\right)^{12}}, \qquad \text{Equation 6.21}$$

$$\beta_x = \beta_y = \frac{\beta_0}{1-\frac{1}{8}\left(\frac{R}{z}\right)^3}, \qquad \text{Equation 6.22}$$

$$\beta_z = \frac{\beta_0}{1-\frac{5}{16}\left(\frac{R}{z}\right)^3+\frac{15}{256}\left(\frac{R}{z}\right)^6}, \qquad \text{Equation 6.23}$$

where γ_0 and β_0 are respectively the translational and rotational drag coefficients in bulk and are defined as $\gamma_0 = 6\pi\eta R$ and $\beta_0 = 8\pi\eta R^3$, with R is the microspheres radius and z is the microsphere center-surface separation in the axial direction and η representing the dynamic viscosity.

External forces. The external forces that are implemented in our numerical simulation are the laser force $\vec{F}_{laser}$, the force of the DNA $\vec{F}_{DNA}$, the force of the surface $\vec{F}_{surface}$, the buoyancy force $\vec{F}_{buoyancy}$ and the gravitational force $\vec{F}_{gravity}$. The laser force is implemented as a constant force in z direction and is set manually:

$$\vec{F}_{laser} = F_{laser}\hat{z} \qquad \text{Equation 6.24}$$

The force of the DNA is calculated with the extensible worm like chain model (ref):

$$\vec{F}_{DNA} = -\left(\frac{k_B T}{L_p}\right)\left[\begin{array}{c} \frac{1}{4}\left(\begin{pmatrix}1\\1\\1\end{pmatrix} - \frac{\vec{a}}{L_c} + \frac{\vec{F}_{DNA}}{S}\right)^{-2} \\ -\frac{1}{4}\begin{pmatrix}1\\1\\1\end{pmatrix} + \frac{\vec{a}}{L_c} - \frac{\vec{F}_{DNA}}{S} \end{array}\right], \qquad \text{Equation 6.25}$$

with L_p, L_c and S respectively the persistence length, the contour length and the stretch modules of DNA (**Table 6.1**). The vector $\vec{a} = (x_{DNA}, y_{DNA}, z_{DNA})$ points from the DNA-surface attachment point towards the DNA-microsphere attachment point. The surface force results from the electrostatic interaction between microsphere and surface[34]:

$$\vec{F}_{surface} = 4\pi\epsilon_W\epsilon_0\psi_0^2 R e^{-(z-R)/l}\hat{z}, \qquad \text{Equation 6.26}$$

with ϵ_W and ϵ_0 respectively the permittivity of water and vacuum, ψ_0 the effective surface potential, R the microsphere radius, z the axial distance between surface and microsphere center and l the Debye screening length. The buoyancy and gravity forces are implemented as follows:

$$\vec{F}_{buoyancy} + \vec{F}_{gravity} = \frac{4}{3}\pi R^3 g(\rho_{med} - \rho_{bead})\hat{z}, \qquad \text{Equation 6.27}$$

with g the gravitational constant, ρ_{med} the density of water and ρ_{bead} the density of the microsphere. See the supplementary information for the parameters used.

Mie calculations. Radiation pressure exerted on a spherical particle by a beam of light is calculated using Mie theory[14]. The laser force is expressed in terms of the extinction coefficient C_{ext}, the scattering cross section C_{sca} and the average cosine of the scattering angles $\langle\cos\theta\rangle$:

$$F_{laser} = \frac{n_m I}{c}(C_{ext} - C_{sca}\langle\cos\theta\rangle), \qquad \text{Equation 6.28}$$

with n_m the refractive index of the surrounding medium, I the laser intensity and c the speed of light. C_{ext}, C_{sca} and $\langle\cos\theta\rangle$ are expressed by:

$$C_{sca} = \frac{2}{x^2}\sum_{n=1}^{\infty}(2n+1)(|a_n|^2 + |b_n|^2), \qquad \text{Equation 6.29}$$

$$C_{ext} = \frac{2}{x^2}\sum_{n=1}^{\infty}(2n+1)\mathrm{Re}\{a_n + b_n\}, \qquad \text{Equation 6.30}$$

$$\langle\cos\theta\rangle = \frac{4\pi R^2}{x^2 C_{sca}}\sum_{n=1}^{\infty}\left[\frac{n(n+2)}{n+1}\mathrm{Re}\{a_n a_{n+1}^* + b_n b_{n+1}^*\} + \frac{2n+1}{n(n+1)}\mathrm{Re}\{a_n b_n^*\}\right], \qquad \text{Equation 6.31}$$

where $x = 2\pi R/\lambda$, R is the particle radius, λ is the wavelength of the light in the surrounding medium and the asterisk denotes complex conjugation. a_n and $b_n$are classical Mie coefficients depending on the particle size and material. The calculation of these coefficients is done according to Bohren et al[14]. See the Table 6.1 for the material parameters.

Once a_n and b_n are calculated the equation above are used to derive the laser force acting on the particles numerically. To decrease computation times, the summations are terminated after $n_{max=}x + 4x^{1/3} + 2$. This amount a terms has proven to be sufficient to calculate a_n and b_n correctly[14].

Loading rates. Laser powers and therefore the laser forces on the microspheres can be altered with a frequency in the 100Mhz regime using AOMs. The tension of the DNA will respond much slower due to the viscous drag of the microsphere. To calculate the response time of the system the following equation of motion for the microsphere is solved (inertia is neglected):

$$F_{laser}(t) - \gamma\dot{x}(t) - kx(t) = 0, \qquad \text{Equation 6.32}$$

with $\dot{x}$ the time derivative of the position x and k the stiffness of the DNA. If we assume that both the laser force and the stiffness of the DNA are constant, the solution of the equation of motion is $(t) = \frac{F_{laser}}{k}\left(1 - e^{-\frac{k}{\gamma}t}\right)$. The response time of the system is thus proportional to $\frac{\gamma}{k}$. Supplementary Figure 6.7a shows that the typical switching time lies in the order of 100 µs for 4µm microsphere in diameter and a DNA stiffness of 2,000 $\mathrm{pN/\mu m}$ (enthalpic regime of DNA with L_c=0.5 µm). Linear force ramps exerted on the DNA can be achieved below the response time of the system if a linearly increasing laser force is applied with an initial offset (Supplementary Figure 6.7b). The initial laser offset that should be applied to create a linear loading rate on the DNA is proportional to the height of the loading rate. This limits the force range for high loading rates. Supplementary Figure 6.7b shows that it is possible to apply a loading rate of $10^6\,\mathrm{pN/s}$ over 50 % of the total force range. This range increases to 95 % for a loading rate of $10^5\,\mathrm{pN/s}$. The smallest achievable loading rate using OP is limited by the laser power stability, which typically fluctuates 1 % over 4 hours (IPG laser spec. sheet). To achieve a loading rate that is linear within an accuracy of 10 %, the loading rate should at least be ten times larger than the rate of the laser power fluctuations. This results in a minimal loading rate of $\frac{F_{laser,max}}{1440s} \sim 3 \cdot 10^{-2}\,\mathrm{pN/s}$ for a maximum loading force of 40 pN. The power fluctuations of the laser can be reduced using a feedback loop to control the laser power. Laser intensity stabilizers can attenuate the noise by a factor of 400.[35] This decreases the minimum force ramp to $\sim 1 \cdot 10^{-4}\,\mathrm{pN/s}$ for a maximum loading force of 40 pN.

Table 6.1: parameters used for calculations.

Parameter	Variable	Value (for 1µm polystyrene microsphere at 21°C)
Viscosity of medium	η	1.00 mPa s
Refr. index medium at 1070 nm	n_{med}	$1.32 + 10^{-6}i$
Refr. index polystyrene at 1070 nm	n_{poly}	$1.58 + 0i$
Refr. index melamine at 1070 nm	n_{mel}	$1.68 + 0i$
Refr. index titania at 1070 nm	n_{tit}	$2.50 + 0i$
Refr. index gold at 1070 nm	n_{gold}	$0.27 + 7.15i$
Density polystyrene	ρ_{poly}	1.05 g cm^{-3}
Density melamine	ρ_{mel}	1.57 g cm^{-3}
Density titania	ρ_{tit}	4.23 g cm^{-3}
Density gold	ρ_{gold}	19.3 g cm^{-3}
Viscous drag of microsphere	$\gamma = 6\pi R\eta$	9.42 pN s µm^{-1}
Average thermal velocity	$v_{th} = \sqrt{k_B T/m}$	2.71 mm s^{-1}
Reynolds number	$\mathrm{Re}=\mathrm{R}v_{th}\rho/\eta$	$1.4 \cdot 10^{-3}$
Absolute permittivity of water	$\epsilon_0\epsilon_W$	$70.8 \cdot 10^{-13}$ Fm^{-1}
Effective surface potential	ψ_0	10 mV
Debye screening length	l	2 nm
Persistence length of DNA	L_p	50 nm
Contour length of DNA	L_c	350 nm
Stretch modules of DNA	S	1500 pN

Appendix B: Supplementary Figures

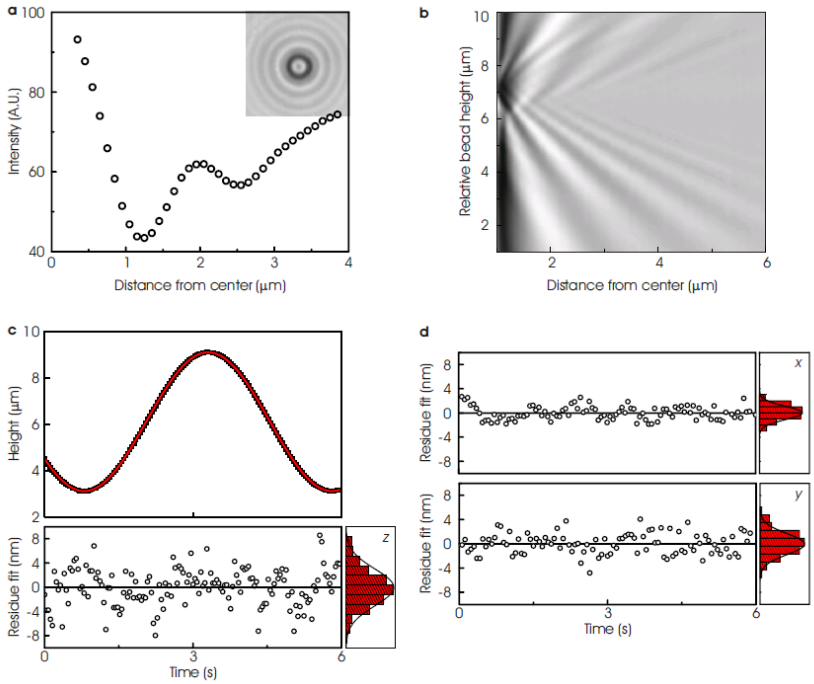

Supplementary Figure 6.1 Relative height determination of a microsphere using a look up table (LUT). (**a**) Images of the microsphere (inset) are converted to a radial profile. Radial profiles of 6 images are averaged and binned over 100 nm. The radial profile is measured as a function of the microsphere height, using the piezo stage to control the height. (**b**) Stack of radial profiles as a function of the relative microsphere height. During a measurement the microspheres radial profile is compared to the radial profiles in the LUT to obtain the microspheres height. (**c**) To determine the accuracy of our microsphere tracking in z (at 25 Hz) we measured the height of a stuck microsphere (2.1 um diameter) that is moved up and down in a sinusoidal manner using the pizo stage. The standard deviation of the residues from the sinusoidal fit of the height data is 4 nm, which is the accuracy we achieve in z. (**d**) The residues in the x and y dimension, determined in the same way as in **c** but moving the piezo stage in respectively x and y. In both these dimensions we achieve an accuracy of approximately 2nm (at 25 Hz).

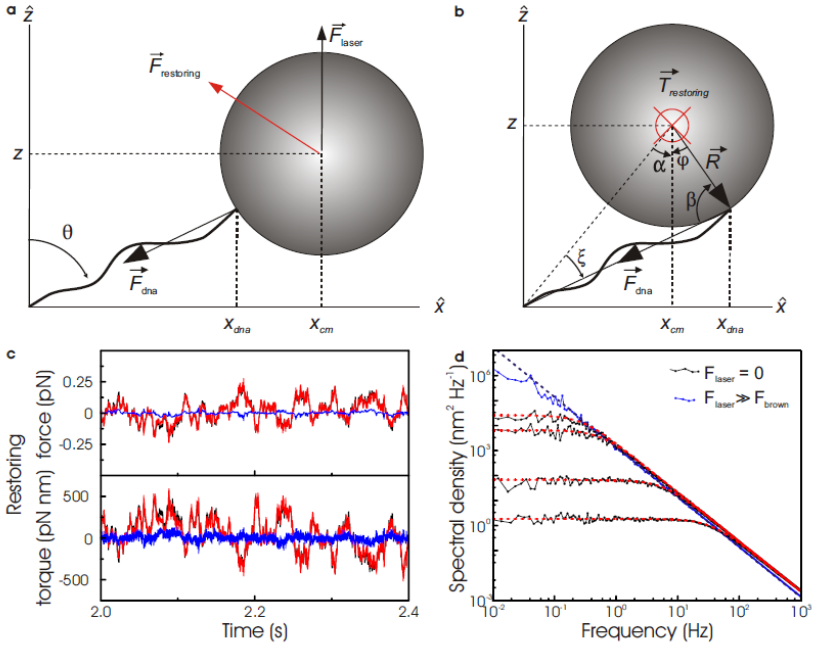

Supplementary Figure 6.2 Schematic overview of a DNA tether pushed out of its equilibrium position by the Brownian force. (**a**) The displacement due to the Brownian motion leads to a small angle θ, giving rise to a restoring force. Note that there is also a difference between the observed centre of the microsphere and the real attachment point of the DNA. (**b**) The displacement and rotation of the microsphere (ϕ) lead to a different anchor point position of the DNA and to a restoring torque acting on the centre of the microsphere. The angles α, β, ξ are introduced to assist the calculations. (**c**) Comparison of the restoring torque and force for the linearised (red) and full model (black). The residuals (blue) are symmetrical and have a standard deviation of 0.01 pN and 26 pN·nm for the force and torque respectively. (**d**) Power spectra of the simulated data sets (black) and plots of the analytical model using the same parameters (dashed red). The spectrum and plot in the absence of force is given in blue for reference.

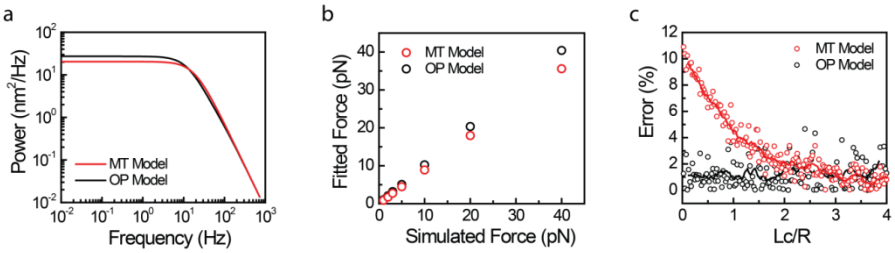

Supplementary Figure 6.3 (a) Power spectra of the Magnetic Tweezer (MT) model and the Optical Pushing (OP) model calculated for a microsphere that is 3 µm in diameter, a DNA with a contour length of 0.3 µm and a exerted force of 10 pN. The graph shows that the microspheres fluctuations are higher at lower frequencies if microsphere rotation is taken into account, leading to a higher plateau in the power spectrum for the OP case. (b) Fitting power spectra of simulated data (acquired from trajectories of 600s) shows the MT model clearly underestimates the applied force, whereas the OP model predicts the forces accurately. (c) The error of the fitted force (using 10pN) for simulated microsphere trajectories using the MT and the OP model. For microsphere-tether systems with $L_c/R < 2$ the OP model is clearly able to fit applied forces more accurately than the MT model.

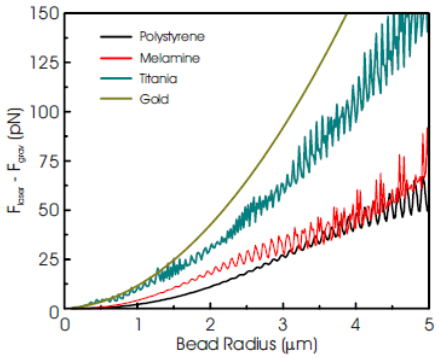

Supplementary Figure 6.4 Calculated resulting optical force for different materials. Gravity is subtracted from the forward scatter force as calculated with the Mie theory. In general materials with a higher refractive index experience a bigger force using the same intensity.

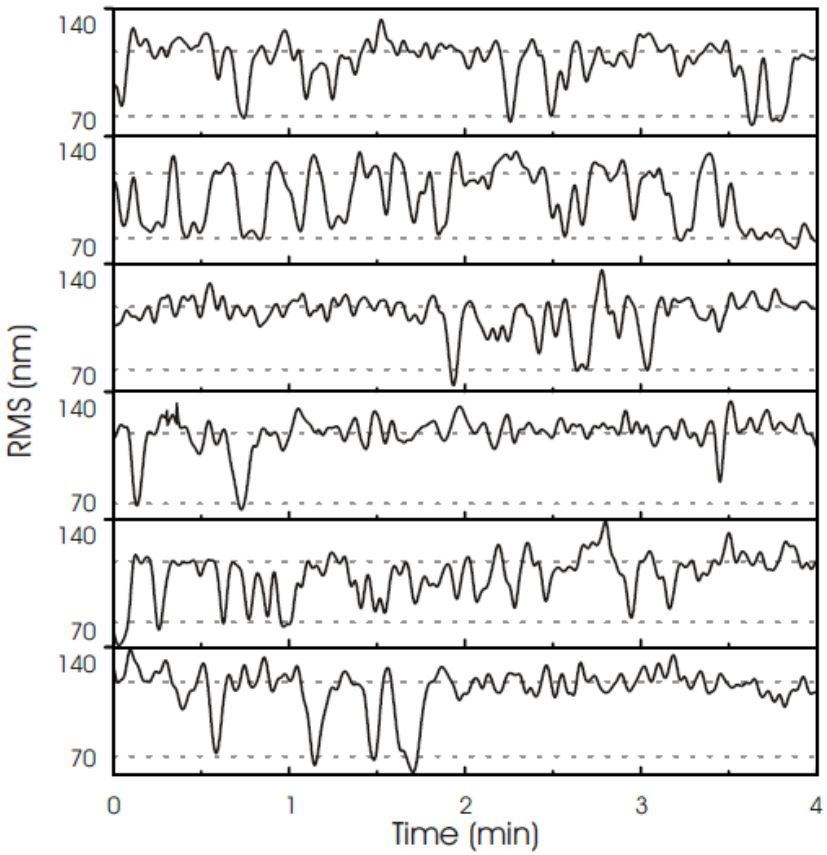

Supplementary Figure 6.5 Root mean square (RMS) traces of simultaneous measured microspheres under constant force of 2 pN, show clear looping behavior (indicated by the dashed lines) in the presence of the FokI restriction enzyme.

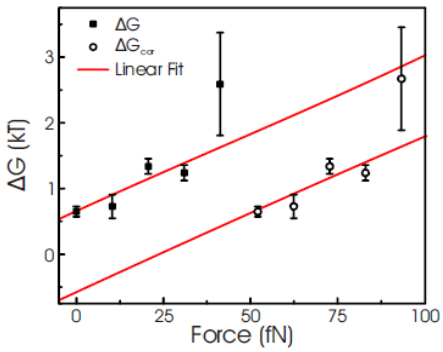

Supplementary Figure 6.6 The calculated free energy change ΔG at different forces for the both the uncorrected and corrected forces (volume exclusion force taken into account). The linear fit is used to determine the standard free energy change ΔG^0

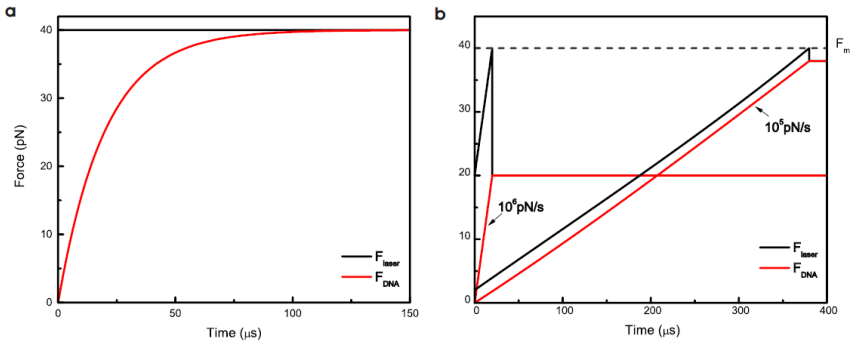

Supplementary Figure 6.7 (a) The force response on the DNA ($L_c = 400nm$) if 40pN is applied instantaneously on the microsphere (ϕ 4.26μm). The response time of the system is ~ 100μs. (**b**) It is possible to achieve a linear force response on the DNA if a a initial offset is applied to the force ramp of the laser. Note that a higher ramp results in a lower maximum force on the DNA.

References

1. Gellert, M. & Nash, H. Communication between segments of DNA during site-specific recombination. *Nature* **325,** 401–4 (1987).

2. Smith, S., Finzi, L. & Bustamante, C. Direct mechanical measurements of the elasticity of single DNA molecules by using magnetic beads. *Science (80-.).* **258,** 1122–1126 (1992).

3. Ashkin, A. Forces of a single-beam gradient laser trap on a dielectric sphere in the ray optics regime. *Biophys. J.* **61,** 569–582 (1992).

4. Merkel, R., Nassoy, P., Leung, a, Ritchie, K. & Evans, E. Energy landscapes of receptor-ligand bonds explored with dynamic force spectroscopy. *Nature* **397,** 50–3 (1999).

5. Halvorsen, K. & Wong, W. P. Massively parallel single-molecule manipulation using centrifugal force. *Biophys. J.* **98,** L53–5 (2010).

6. Binnig, G. & Quate, C. F. Atomic Force Microscope. *Phys. Rev. Lett.* **56,** 930–933 (1986).

7. Svoboda, K., Schmidt, C. F., Schnapp, B. J. & Block, S. M. Direct observation of kinesin stepping by optical trapping interferometry. *Nature* **365,** 721–7 (1993).

8. Neuman, K. C. & Nagy, A. Single-molecule force spectroscopy: optical tweezers, magnetic tweezers and atomic force microscopy. *Nat. Methods* **5,** 491–505 (2008).

9. Laurens, N. *et al.* Dissecting protein-induced DNA looping dynamics in real time. *Nucleic Acids Res.* **37,** 5454–64 (2009).

10. Strick, T. R., Allemand, J., Bensimon, D., Bensimon, A. & Croquette, V. The Elasticity of a Single Supercoiled DNA Molecule. *Science (80-.).* **271,** 1835–1837 (1996).

11. Te Velthuis, A. J. W., Kerssemakers, J. W. J., Lipfert, J. & Dekker, N. H. Quantitative guidelines for force calibration through spectral analysis of magnetic tweezers data. *Biophys. J.* **99,** 1292–302 (2010).

12. R. Reif. *Fundamentals of Statistical and Thermal Physics*. (1985).

13. Howard, J. *Mechanics of motor proteins and the cytoskeleton*. (2001).

14. *Absorption and Scattering of Light by Small Particles*. (Wiley-VCH Verlag GmbH, 1998). doi:10.1002/9783527618156

15. Saiz, L. & Vilar, J. M. G. DNA looping: the consequences and its control. *Curr. Opin. Struct. Biol.* **16,** 344–50 (2006).

16. Allen, D. J. *et al.* MutS mediates heteroduplex loop formation by a translocation mechanism. *EMBO J.* **16,** 4467–76 (1997).

17. Halford, S. E., Welsh, A. J. & Szczelkun, M. D. Enzyme-mediated DNA looping. *Annu. Rev. Biophys. Biomol. Struct.* **33,** 1–24 (2004).

18. Bitinaite, J., Wah, D. a, Aggarwal, a K. & Schildkraut, I. FokI dimerization is required for DNA cleavage. *Proc. Natl. Acad. Sci. U. S. A.* **95,** 10570–5 (1998).

19. Laurens, N. *et al.* DNA looping by FokI : the impact of twisting and bending rigidity on protein-induced looping dynamics. *Nucleic Acids Res.* **40,** 4988–4997 (2012).

20. Rusling, D. a, Laurens, N., Pernstich, C., Wuite, G. J. L. & Halford, S. E. DNA looping by FokI: the impact of synapse geometry on loop topology at varied site orientations. *Nucleic Acids Res.* **40,** 4977–87 (2012).

21. Vipond, I. B. & Halford, S. E. Specific DNA recognition by EcoRV restriction endonuclease induced by calcium ions. *Biochemistry* **34,** 1113–9 (1995).

22. Embleton, M. L., Williams, S. a, Watson, M. a & Halford, S. E. Specificity from the synapsis of DNA elements by the Sfi I endonuclease. *J. Mol. Biol.* **289,** 785–97 (1999).

23. Segall, D., Nelson, P. & Phillips, R. Volume-Exclusion Effects in Tethered-Particle Experiments: Bead Size Matters. *Phys. Rev. Lett.* **96,** 088306 (2006).

24. Yang, Y., Erb, R. M., Wiley, B. J., Zauscher, S. & Yellen, B. B. Imaginary magnetic tweezers for massively parallel surface adhesion spectroscopy. *Nano Lett.* **11,** 1681–4 (2011).

25. Peterman, E. J. G., Gittes, F. & Schmidt, C. F. Laser-induced heating in optical traps. *Biophys. J.* **84,** 1308–16 (2003).

26. Maurer, C., Jesacher, a., Bernet, S. & Ritsch-Marte, M. What spatial light modulators can do for optical microscopy. *Laser Photon. Rev.* **5,** 81–101 (2011).

27. Kress, H. *et al.* Cell stimulation with optically manipulated microsources. *Nat. Methods* **6,** 905–9 (2009).

28. De Vlaminck, I. & Dekker, C. Recent advances in magnetic tweezers. *Annu. Rev. Biophys.* **41,** 453–72 (2012).

29. Gross, P., Farge, G., Peterman, E. J. G. & Wuite, G. J. Combining optical tweezers, single-molecule fluorescence microscopy, and microfluidics for studies of DNA-protein interactions. *Methods Enzymol.* **475,** 427–53 (2010).

30. La Porta, A. & Wang, M. Optical Torque Wrench: Angular Trapping, Rotation, and Torque Detection of Quartz Microparticles. *Phys. Rev. Lett.* **92,** (2004).

31. Pedaci, F., Huang, Z., van Oene, M., Barland, S. & Dekker, N. H. Excitable particles in an optical torque wrench. *Nat. Phys.* **7,** 259–264 (2010).

32. Risken, H. *The Fokker-Plank Equation*. (Springer Berlin Heidelberg 1989).

33. Happel, J. & Brenner, H. *Low Reynolds Number Hydrodynamics*. (Kluwer Academic Publishers, 1983).

34. Scha, E., Nørrelykke, S. F. & Howard, J. Surface Forces and Drag Coefficients of Microspheres near a Plane Surface Measured with Optical Tweezers. **287,** 3654–3665 (2007).

35. Pawley, J. *Handbook of Biological Confocal Microscopy*. (Springer Science + Business Media, 2006).

7 Acoustic Force Spectroscopy

Force-spectroscopy has become an indispensable tool to unravel the structural and mechanochemical properties of biomolecules. Here we extend the force-spectroscopy toolbox with an acoustic manipulation device that allows exerting acoustic forces from sub-pN to hundreds of pN applied to thousands of biomolecules in parallel, with sub-millisecond response time and inherent stability. This method can be readily integrated in lab-on-a-chip devices, allowing cost-effective and massively parallel applications.

Based on: Gerrit Sitters*, Douwe Kamsma*, Gregor Thalhammer, Monika-Ritsch-Marte, Erwin J G Peterman‡ & Gijs J L Wuite‡, *Nature Methods* **12**, 47-50 (2015)

7.1 Introduction

Single-molecule techniques have revolutionized the study of biomolecules, allowing experiments, such as force-induced denaturation of biomolecules, hitherto impossible[1–3]. So far, single-molecule instruments have remained rather complex, requiring specialized expertise for construction and operation, limiting their use mainly to specialized biophysics labs. In addition, many single-molecule techniques allow the user to study only a limited number (often one) of biomolecules simultaneously, reducing experimental throughput and limiting statistics[2,4]. On the single-molecule level, discriminating heterogeneous behavior and rare events from intrinsic stochasticity requires obtaining many independent measurements[2,5]. Novel methods that are less complex, more cost-effective, smaller and allow high throughput are highly desirable[6–8]. Here we present and validate a single-molecule manipulation method, *Acoustic Force Spectroscopy* (AFS), that uses acoustic forces to stretch multiple molecules individually tethered between a surface and a microsphere. We demonstrate that AFS allows the application of controlled forces to at least 120 pN, strong enough to induce major conformational changes in biomolecules, such as the DNA overstretching and the mechanical unfolding of proteins[1,9,10], in a highly parallel fashion.

7.2 Results

7.2.1 Experimental setup

In our AFS instrument (Figure 7.1a,b) we used a piezo element driven by an oscillating voltage to resonantly excite a planar acoustic standing wave over a flow cell. A microsphere (with volume V) subjected to this standing wave experiences a force F along the vertical (z) direction:

$$F = -V\nabla\left[\frac{1-\kappa^*}{4}\kappa_{\mathrm{m}}p^2 - \frac{(\rho^*-1)}{2\rho^*+1}\rho_{\mathrm{m}}v^2\right], \qquad \text{Equation 7.1}$$

in which p is the acoustic pressure, v the acoustic velocity, and ρ^* (= ρ_p / ρ_m) and κ^* (= κ_p / κ_m) the density and compressibility ratio between the particle and the medium, respectively[11]. In the case of polystyrene or silica microspheres in water, the force is dominated by the gradient of the squared acoustic pressure, driving the

microspheres towards an acoustic pressure node. We calculated resonance frequencies and force profiles of the flow chamber used (originally designed for an instrument combining optical tweezers and microfluidics[12]) using a one-dimensional model with the dimensions and material properties of flow cell and microspheres as input parameters (Appendix A)[13] and compared them to the experimentally obtained values. Driving the piezo element at a predicted frequency of 6.8 MHz (measured at 6.7 MHz, determined from the maximum force obtained with a frequency sweep, see below) resulted in microspheres near the upper glass-water interface strongly being pulled away from the surface (Figure 7.1c,d,f). This force was used in the following experiments to apply tension on biomolecules tethered between the upper surface and the microsphere. The force applied to the microsphere was constant within 5% when changing the microsphere's axial position by 1 µm, which was the length scale of the force-induced extension of the biomolecules used here. Another predicted resonance at 9.2 MHz (measured at 9.0 MHz) allowed pushing of the microspheres towards the surface, which was very useful in our experiments, since it allowed precise determination of the surface location and, in principle could facilitate the formation of interactions between functionalized microspheres and surface-attached biomolecules (Figure 7.1c,e,f). We determined three-dimensional positions of the tethered microspheres by analyzing the images obtained with a 40x air spaced microscope objective (NA = 0.75) and a digital camera (Figure 7.1a,b). Our tracking software is available online (Appendix A) and has a precision of ~2 nm in the *x*- and *y*-directions and ~5 nm in *z* (at 50 Hz), as determined from the standard deviation of traces of immobilized microspheres (Appendix A and Supplementary Figure 7.1). We corrected for mechanical drift by tracking the displacement of an immobilized reference microsphere attached to the surface (Figure 7.1aiii). Bright-field illumination was provided in epi-configuration, through the objective, reflected by an aluminum layer sputtered on top of the flow cell, below the opaque piezo element. This allowed for a simple, very compact design, compatible with a standard microscope with epi-illumination (Supplementary Figure 7.2).

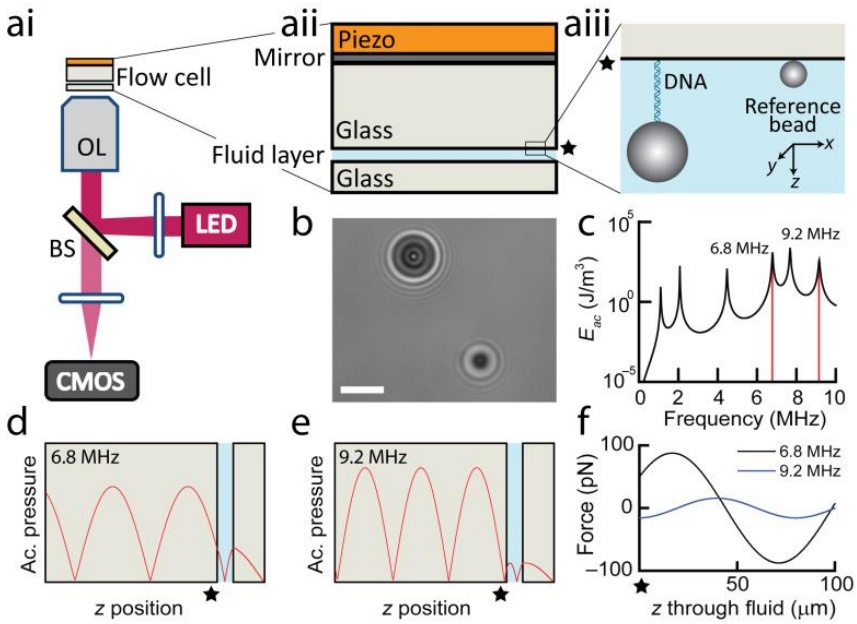

Figure 7.1 Principle of Acoustic Force Spectroscopy. (**ai**) The experimental setup consisted of the AFS device integrated in a flow cell. The optics used for imaging were: an inverted microscope equipped with a microscope objective lens (OL), a digital camera (CMOS), a LED light source (455 nm) and a 50/50 beam splitter (BS). (**aii**) The flow cell consisted of two glass plates with a fluid chamber in between. For illumination purposes, the upper glass slide had a sputtered mirroring aluminum layer on top. A piezo plate was glued on top of the mirror. (**aiii**) A single DNA molecule, attached with one end to the upper glass plate (indicated by the black star) and the other end to a microsphere, was stretched by acoustic forces acting on the microsphere. (**b**) Digital camera image of a DNA-tethered polystyrene microsphere (4.5 µm diameter; DNA length 8.4 kbp) and a silica reference microsphere (1.5 µm diameter; scale bar 5 µm). (**c**) Theoretically predicted acoustic resonances of the AFS device (driven with 5 V_{pp}). (**d,e**) Predicted pressure distribution at the 6.8 MHz and 9.2 MHz resonance frequencies across the glass and fluid layers. (**f**) Predicted forces for a 4.5-µm-diameter polystyrene microsphere within the fluid layer directed along the z-direction (0.5 W input power). Microspheres near the surface denoted with the black star (z = 0) experienced a force directed away from the surface for the 6.8 MHz resonance, or towards the surface for the 9.2 MHz resonance.

7.2.2 AFS applied to tethered DNA

To validate our approach, we applied acoustic forces to stretch individual, double-stranded DNA tethers (8.4 kilobase pair (kbp), ~2.8 µm contour length) attached with one end to the flow cell glass surface and the other end to a polystyrene microsphere (diameter 4.5 µm) (Figure 7.2a). Without driving the piezo, diffusive motion of the tethered microsphere was observed, comparable to a tethered-particle motion experiment[14]. Driving the piezo at the 9.0 MHz resonance, pushed the microspheres towards the surface, allowing the determination of the zero z-position. Operating at the 6.7 MHz resonance, pulled the microsphere away from the surface. At the same time the Brownian motion of the microspheres in the directions parallel to the surface was quenched due to the increased tension on the DNA tether. To quantify the tension on the DNA, we calculated the power spectrum of the position fluctuations of the microsphere (in the directions parallel to the glass interface) and fitted it with a model using the tension as a free fit parameter (Figure 7.2b, Appendix A). The planar nature of the acoustic waves allowed application of the acoustic forces homogeneously over an area of several millimeters squared (Supplementary Figure 7.3). As predicted by Eq. 1, tension scales with the volume of the particle (Figure 7.2c), and was higher for silica microspheres than for polystyrene ones, due to silica's higher stiffness and density. In further agreement with theory, the tension on the DNA tether scaled with the squared voltage applied over the piezo element (Figure 7.2c), allowing accurate control of tether tension by changing the piezo driving voltage. Note that, although acoustic forces acting on the microsphere can be changed fast, the response of the tension on the molecule is limited by the effect of solvent drag on the motion of the microsphere. For the microsphere sizes tested here, the response time was less than a millisecond in the enthalpic force regime (i.e. at forces above approximately 1 pN; Appendix A). Theory predicts that ultimately the precision of AFS is limited by thermal fluctuations of the position of the tethered microsphere, which we verified by experimental determination of the standard deviation (σ_L) of the positions (Figure 7.2d, Appendix A). Finally, AFS is very stable and thus allowed long-time determination of forces and positions, as is evident from measurements of the length of a single DNA molecule subjected to a force of 9 pN, which showed no substantial drift on a time scale of 16 hours (Supplementary Figure 7.4).

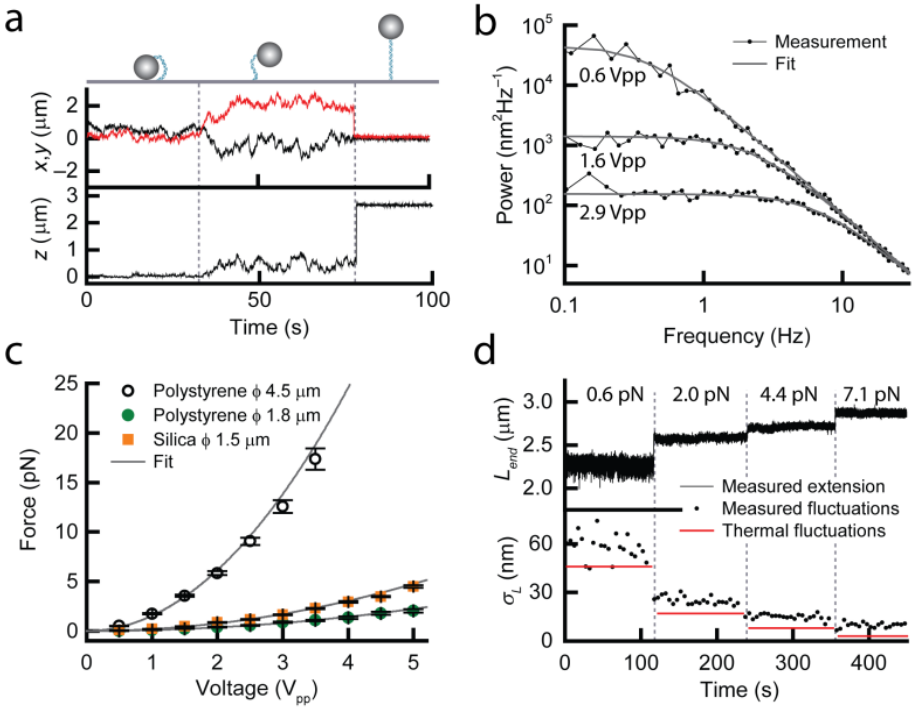

Figuur 7.2 | AFS applied to tethered DNA (a) Time traces showing the position of a DNA-tethered microsphere (polystyrene, diameter 4.5 µm; DNA length 8.4 kbp). In the first 35 s the piezo was driven at 9.0 MHz (0.5 V_{pp}), pushing the microsphere towards the surface. From 35-80 s, no acoustic force was applied and after 80 s the piezo was driven at 6.7 MHz (2.4 V_{pp}), pulling the microsphere away from the surface. (b) Measured and fitted mean power spectra values of the microsphere's x and y positions using a Lorentzian (Appendix A). Forces obtained: 0.61 ± 0.07, 3.9 ± 0.1 and 11.8 ± 0.2 pN at 0.6, 1.6 and 2.9 V_{pp} piezo driving voltages respectively (piezo driven at 6.7 MHz). (c) Forces acting on polystyrene and silica microspheres tethered to the glass surface with DNA (length 8.4 kbp) as determined from power spectrum analysis (data points: mean, error bars: s.e.m., <n> = 30). Quadratic fits yielded quadratic constants of 1.54 ± 0.06, 0.19 ± 0.01, 0.089 ± 0.003 pN V^{-2} for the 4.5, 1.5 and 1.8 µm microspheres respectively. (d) Noise characterization of the measured end-to-end distance. Upper panel: measured end-to-end distance as a function of time (acquired at 50 Hz) for different forces. Lower panel: standard deviation σ_L of the measured length fluctuations and calculated thermal fluctuations (Appendix A).

7.2.3 Force-extension, constant-force and dynamic force spectroscopy measurements

To demonstrate the use of AFS as a powerful single-molecule technique that can give access to the force range relevant for measurements on biomolecules, we performed force-spectroscopy experiments on individual double-stranded DNA molecules (Figure 7.3a). AFS allowed accurate determination of the force-extension behavior of both torsionally unconstrained (8.4 kbp; 2.8 µm contour length) and torsionally constrained DNA (10.1 kbp; 3.4 µm contour length), over the full range of forces where the double helix remains intact (0–65 pN and 0–110 pN for torsionally unconstrained and constrained DNA, respectively[9,10]). These experimental curves were well described by the extensible wormlike chain model[15]. Next, we used AFS to investigate how protein binding affects DNA mechanical properties. To this end, we probed RecA-filament assembly on torsionally unconstrained dsDNA (8.4 kbp) in the presence of ATP. A single RecA protein binds to three base pairs in the DNA and increases the contour length of the three base pairs by 0.51 nm[16]. A double-stranded DNA molecule completely coated with RecA thus has a 1.5-fold longer contour length than naked DNA. Such a length increase could be clearly resolved in force-extension measurements using AFS (Figure 7.3b). To obtain insight in the dynamics and stochasticity of the cooperative RecA binding to DNA, we used AFS to perform constant-force measurements of the extension of multiple DNA molecules simultaneously, in the presence of RecA and ATP. It is well documented that RecA binding to double-stranded DNA depends strongly on DNA tension: the binding rate increases with tension, while the unbinding rate decreases[17]. Monitoring DNA extension showed that indeed RecA-filament formation was enhanced at a tension of 40 pN, leading to an effective increase of DNA length (Figure 7.3c). RecA-filament disassembly was dominant at 2.5 pN, resulting in shortening of the DNA molecule. At an intermediate tension of 30 pN, the competition between filament formation and disassembly led to heterogeneity between two DNA tethers: one showing a period of length increase due to filament growth after a rare nucleation event, followed by a period of length decrease due to disassembly of filaments, the other showing no overall length change.

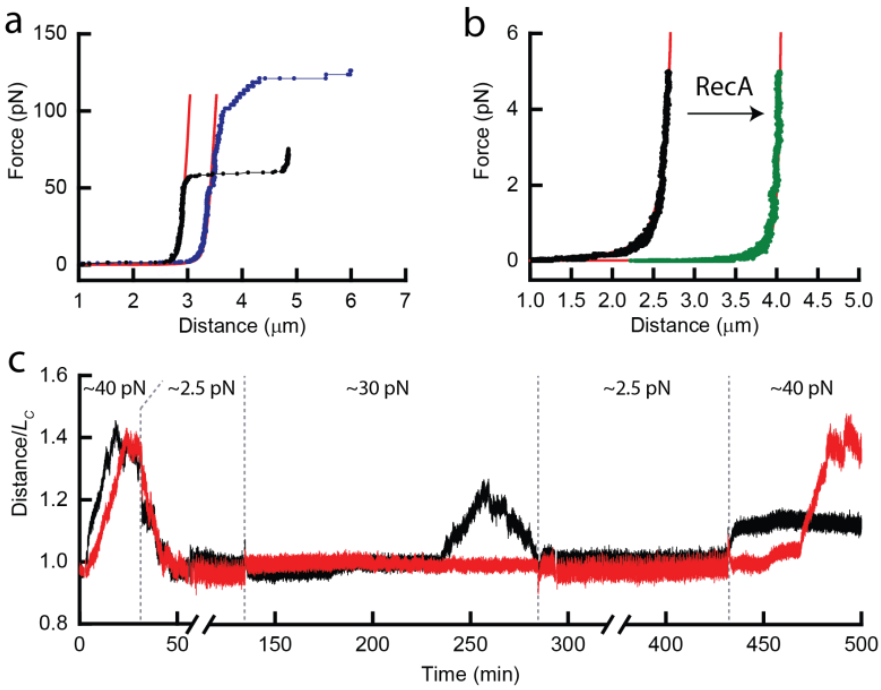

Figuur 7.3 Force-extension and constant-force and measurements. (**a**) Stretching curve of 8.4 kbp torsionally unconstrained DNA and 10.1 kbp torsionally constrained DNA and their corresponding extensible worm-like chain fits (8.4 kbp DNA: persistence length 52 nm, contour length 2.87 µm and stretch modulus 2,000 pN; 10.1 kbp DNA: persistence length 50 nm, contour length 3.46 µm and stretch modulus 2,100 pN). (**b**) Experimental force-extension curves of a 8.4 kbp DNA molecule measured in absence and in presence of 1 µM RecA (pH 6.4). Fits yielded contour lengths of 2.82 ± 0.02 µm and 4.26 ± 0.04 µm, for the bare DNA and RecA-coated DNA respectively. (**c**) Length-time traces of two DNA molecules (8.4 kbp) in the presence of 0.5 µM RecA (pH 7.4): DNA length increased at 40 pN and decreased at 2.5 pN. At 30 pN stochastic length variations were observed.

Finally, to demonstrate the massive multiplexing capability of AFS, we used dynamic force spectroscopy to unravel the energy landscape of the DIG::anti-DIG antigen-antibody interaction between digoxigenin and anti-digoxigenin. We tracked over 2000 microspheres in real time in *x* and *y* within one field of view (Figure 7.4a). We applied very strict selection criteria to discriminate singly tethered microspheres from doubly tethered and surface-attached ones, yielding, in a typical field of view, approximately 8% (~150) of singly, DIG::anti-DIG tethered spheres (using a 1.1 kbp DNA linker). A force calibration was performed independently for each of these spheres (Appendix A, Supplementary Figure 7.5 and 7.6). The number of microspheres tracked yielded in a single run of the machine a complete bond ruptures force histogram (analysis software available online, Appendix A). We performed measurements at seven different loading rates spanning six orders of magnitude (from 6.3×10^{-4} pN s^{-1} to 5.4×10^{2} pN s^{-1}, Figure 7.4b). Note that even higher loading rates are attainable when a camera with a higher frame rate is used. A plot of the rupture force against the logarithm of the loading rate showed two distinct linear regimes (inset, Figure 7.4b**),** which correspond to two energy barriers along the unbinding pathway[18]. Linear fits yielded a dissociation rate at zero force of $k_{off1} = (7 \pm 1) \times 10^{-5}$ s^{-1} and a distance from the ground state to the energy barrier of $\Delta x_1 = 1.54 \pm 0.07$ nm at low loading rates and $k_{off2} = (2.7 \pm 0.7) \times 10^{-2}$ s^{-1} and $\Delta x_2 = 0.57 \pm 0.05$ nm at high loading rates (Appendix A). Previous single-molecule studies have yielded higher off-rates for DIG::anti-DIG bonds, indicating weaker binding[7,19], which, most likely, is due to the different antibodies used[20] (Appendix A). So far, most dynamic force-spectroscopy experiments have been performed using Atomic Force Microscopy, requiring breaking of individual bonds, one at a time. When we used the slowest loading ramp (6.3×10^{-4} pN s^{-1}) it took on average several hours for a single bond to rupture. Consequently, measuring a histogram consisting of ~150 rupture events with this loading rate using AFM would take several months, which makes this regime difficult to access for AFM measurements.

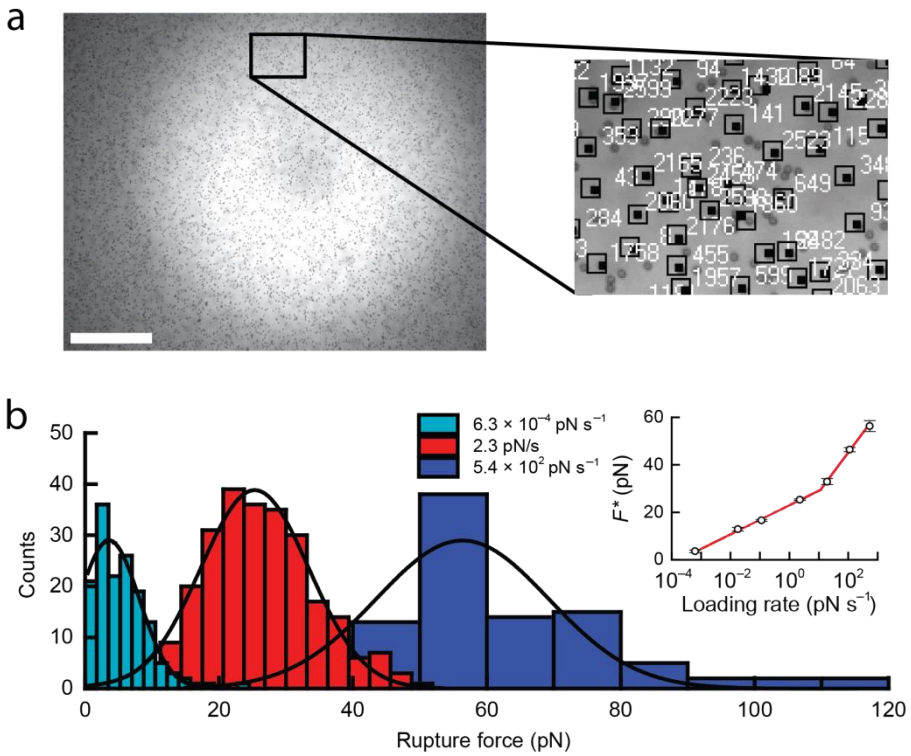

Figuur 7.4 Dynamic force spectroscopy measurements. (**a**) Typical field of view (scale bar 200 µm) of the dynamic force spectroscopy measurements, showing thousands of microspheres (diameter 2.8 µm). The majority of these were tracked in real time. Zoom shows a section with several regions of interest (black squares) around tracked microspheres (black points) and the identification number the tracking software had given them. (**b**) Rupture-force distribution of the DIG::anti-DIG bond at different loading rates. Each histogram was obtained from a single field of view. The inset shows the most probable rupture force (F*), obtained from the Gaussian fits, as a function of loading rate (errors are s.e.m., <n> = 145).

7.3 Conclusion

In conclusion, we have demonstrated that AFS is an accurate single-molecule technique providing insight into protein-DNA and protein-protein interactions by force-extension, constant-force and dynamic force spectroscopy measurements. Applications can be readily extended to studies of other (bio)molecules and (bio)molecular interactions. Moreover, AFS is a unique single molecule tool that combines a high dynamic force range with massive multiplexing capabilities. Other advantages of AFS are its relative simplicity, low cost and compactness, which allow straightforward implementation in lab-on-a-chip devices. These aspects will help to spread single-molecule methods from the realm of fundamental research in specialized laboratories, towards more wide-spread applications in for example molecular biology and medical diagnostics.

Appendix A: Additional information

Experimental setup. For the force-extension and constant-force measurements (Figure 7.2 and 7.3) a 40x microscope objective was used to image and illuminate the tethered microspheres, together with automatic focus-drift correction (Nikon, Perfect Focus, CFI Plan Fluor 40x, NA 0.75). Images were taken with a CMOS camera (Thorlabs, DCC1545M). For the dynamic force spectroscopy measurements (Figure 7.4) a 10x microscope objective (Nikon, CFI Plan Fluor 10x, NA 0.30) was used in combination with a 0.45x c-mount adapter (Nikon, MQD42040). Images were obtained with a CMOS camera (Thorlabs, DCC3240M, with a full-frame frame rate of 60 Hz. For illumination, a fiber-coupled blue LED (Thorlabs, M455F1) was coupled into the imaging path with a 50:50 beam-splitter plate (Thorlabs, EBS2). Reference images required for particle tracking in *z* were obtained by mounting the AFS device consisted of a flow chamber and a piezo plate. The borosilicate-glass flow chamber (Micronit Microfluidics B.V.) consisted of bottom and top glass plates of 170 µm and 1 mm thickness respectively, the fluid channel width was 2 mm and thickness was 100 µm. On top of the flow cell a thin (approx. 200 nm) aluminum layer was applied, serving as a mirror allowing bright-field microscopy in epi configuration. The disk-shaped piezo element (Meggitt Sensing Systems, material PZ26) had a diameter of 7 mm and a thickness of 0.22 mm, and was equipped with wrap-around gold-nickel (1.5–2 µm nickel and a few nm gold) electrodes allowing connection of both electrodes from the same side. The piezo element was glued to the chamber with a cyanoacrylate adhesive (Permatex, 40150A) (Supplementary Figure 7.2). The piezo element was driven with a function generator (Agilent, 33250A) in combination with an RF-amplifier (SCD, ARS 2_30_30, 50 Ω impedance, 10 W max. output power). A maximum driving voltage of 20 V_{pp} was applied, which did not result in ultrasonic cavitation. Powers used in our measurements did not lead to sample heating of more than a few degrees (Supplementary Figure 7.7). When connected directly to the function generator, the maximum voltage that could be applied to the piezo element was 4.0 V_{pp} (at 6.7 MHz). The thickness of the individual layers was not very critical for the construction of an AFS device since tolerances were quite large (Supplementary Figure 7.8). One feature that is important was the use of a thin layer of glue[13], which we achieved by applying force to the piezo plate while gluing.

One-dimensional acoustical model. To provide insight into the operation of the AFS device and for identifying acoustic resonances with the desired properties a one-

dimensional model was used, as previously described[13,21]. The model considers the different layers (piezo, glass and fluid) as analogous to a set of electrical transmission lines in which the voltage represents the acoustic pressure. The impedance of every layer is determined by the density and the speed of sound of the different layers. The piezo layer is driven by an applied voltage, which is coupled to mechanical quantities via a transformation ratio that is defined by the piezo material. When the thickness, impedance and damping of all layers are known, resonance frequencies, acoustic pressures and velocities along the different layers can be calculated. Our layered resonator was modeled with a transducer of PZT4D material (thickness t = 220 µm, speed of sound c = 4530 m s^{-1}, density ρ = 7700 kg m^{-3}, piezo-constant h_{33} = 2.37 × 10^9 V m^{-1}, relative permittivity ε_r = 700), and carrier (t = 1000 µm) and reflector (t = 170 µm) layers of glass (c = 6000 m s^{-1}, ρ = 2200 kg m^{-3}) and water as the fluid (t = 100 µm, c = 1480 m s^{-1}, ρ = 1000 kg m^{-3}). Forces were calculated for polystyrene particles (c = 1960 m s^{-1}, ρ = 1000 kg m^{-3}). The Quality factor (ratio between the stored and dissipated acoustic energy) accounts for the damping and all other losses throughout the resonant device. These values are generally much lower than material Q-factors and are commonly determined experimentally[22]. We assumed Q = 230 in every layer to match the calculated with the measured forces. The electrodes of the transducer and the glue layer were neglected in the acoustical model because of their relatively small thickness.

Microsphere tracking. Acquired images were processed in real time to extract the microsphere positions in 3 dimensions. To determine the x- and y-position a cross-correlation algorithm was applied[14], whereas for z-position a look-up table (LUT) was used, containing a library of radial profiles previously acquired as a function of microsphere z-position[23]. The precision of x- and y-position determination was about 3 nm and for z-position determination about 5 nm at an acquisition rate of 50 Hz (Supplementary Figure 7.1). Tracking software is available online.

Force calibration. Experimental power spectra were obtained for each microsphere and binned using equal-sized blocks on the frequency axis (having n points per block). These binned power spectra were fitted by a Lorentzian using importance-weighted least squares[24,25]:

$$P(f) = \frac{D/(2\pi^2)}{f^2 + \left(k/\left(2\pi \times \gamma_{fax}\right)\right)^2} \qquad \text{Equation 7.2}$$

With $D = k_BT / \gamma_{fax}$ the microspheres diffusion constant, γ_{fax} the effective drag coefficient, k_B Boltzmann's constant, T the temperature, f the frequency and k the stiffness of a Hookean spring acting on the microsphere in the x- and y- dimension $k = F / (L_{ext} + R)$. In this expression of k, F is the force, L_{ext} is the measured extension of the DNA and R is the radius of the microsphere. Since microsphere and surface were in close proximity, their hydrodynamic interaction was taken into account using Fáxen's law to calculate the effective drag on the microsphere[25]. Both D and F were used as free fit parameters. The values for D obtained from the fits were bias corrected by $D_{cor} = D \times (n / n - 2)$ to account for the non-Gaussian distributed data in each block[26]. We plotted the bias-corrected power spectra together with the log-binned experimental spectra (Figure 7.2b). We did not correct for aliasing or motion blurring since these effects did not contribute significantly to the calibrations performed here (Supplementary Figure 7.9).

Response time. When the acoustic force acting on a tethered microsphere is changed by altering the driving voltage, the tension acting on the molecule does not change immediately, but is delayed due to viscous drag. To estimate the system response time, we used Newton's 2nd law, while neglecting inertia due to the low Reynolds number of the system:

$$F(t) - \gamma \dot{z}(t) - k_z z(t) = 0, \qquad \text{Equation 7.3}$$

With $\dot{z}$ the time derivative of the position z, γ the drag coefficient and k_z the stiffness of the Hookean spring acting on the microsphere when it is displaced by a distance z from its equilibrium position at $z = 0$. When the acoustic force $F(t)$ is suddenly switched from F_1 to F_2 at $t = 0$ then the microsphere approaches its equilibrium position following:

$$z(t) = \frac{F_2}{k_z}\left(1 - \frac{F_2 - F_1}{k_z} e^{-\frac{k_z}{\gamma}t}\right). \qquad \text{Equation 7.4}$$

The response time of the system is thus of the order γ / k_z, which is approximately 0.4 ms for a 4.5 µm diameter microsphere, assuming a 8.4 kbp DNA stretched within the enthalpic regime ($k_{DNA} \approx 100\ \mathrm{pN\ \mu m^{-1}}$). This is much longer than the switching time of the driving voltage (which is of the order 100 ns) and the time it takes until the acoustic standing wave reaches its final amplitude ($2Q / \omega_0 \approx 10$ µs). The response time can thus be reduced by increasing system stiffness (using shorter DNA) or decreasing microsphere drag (using smaller microspheres).

Thermal fluctuations and instrumental uncertainty. The tethered microspheres undergo Brownian motion, leading to fluctuations in DNA end-to-end length. The standard deviation of these fluctuations are estimated to be[5]:

$$\sigma_{\text{therm}} = \left[\frac{2k_BT}{\pi k_{\text{DNA}}}\arctan\left(\frac{2\pi\gamma_{\text{fax}}f_s}{k_{\text{DNA}}}\right)\right]^{\frac{1}{2}}, \qquad \text{Equation 7.5}$$

with f_s the sampling frequency. For a 4.5 µm microsphere tethered by a DNA molecule with length 8.4 kbp and stretched with a force of 8.0 pN, position fluctuations with a standard deviation $\sigma_{\text{therm}} \approx 3$ nm are expected (sampling frequency 50 Hz). We measured larger fluctuations $\sigma_L \approx 10$ nm, indicating that the instrumental uncertainty lied around 10 nm. A major contribution to this uncertainty was the tracking uncertainty, which was 5 nm for immobilized microspheres (**Supplementary Figure 7.1**) and which was most likely larger for tethered spheres due to motion blurring.

Dynamic force-spectroscopy measurement. The bond-rupture measurements (Figure 7.4) were performed to characterize the force-dependent unbinding kinetics of digoxigenin (DIG) and its antibody (polyclonal anti-digoxigenin (anti-DIG) from sheep, Roche, Cat. No. 11 333 089 001). In the assay, DNA molecules (1091 bp) labeled with a single DIG antigen at one end and a streptavidin at the other end were used, which were tethered between an anti-DIG coated surface and to 2.85 µm streptavidin coated microsphere. Since the DIG::anti-DIG bond is by far the weakest link, all rupture events could be safely assigned to these bonds (example: Supplementary Figure 7.6). Note that our experimental approach allowed performing such experiments for a few thousand microspheres in parallel. Evaluation of this large amount of measured position data to extract rupture forces was done in parallel as well. It was therefore, not more time consuming to analyze thousands of traces than to analyze a single trace, apart from the computation time (which was well below a minute). Analysis software is available online. Tracking the positions of all microspheres individually enabled us to discriminate between single-tethered microspheres and stuck or multiple-tethered microspheres (Supplementary Figure 7.5). By selecting on the total amount of motion both microspheres that were stuck to the glass or hindered in some way in their motion (low RMS) and microspheres that were tracked poorly (high RMS due to tracking errors) were discarded. The amount of motion was quantified using root mean square motion of the microsphere in *x* and *y* over a period of more than 15 minutes[27]:

$$\mathrm{RMS} = \sqrt{\langle (x-\bar{x})^2 + (y-\bar{y})^2 \rangle_t}\ , \qquad \text{Equation 7.6}$$

with $\bar{x}$ and $\bar{y}$ the average positions over time t. In our experiments, microspheres with RMS values below 350 nm and above 550 nm were discarded. Determination of the symmetry of motion allows discrimination between microspheres tethered with a single and multiple DNA molecules. Only single-tethered particles exhibit symmetrical motion around their anchor points. Motion symmetry was calculated using the covariance matrix[27]:

$$C = \begin{pmatrix} \sigma_{xx} & \sigma_{xy} \\ \sigma_{yx} & \sigma_{yy} \end{pmatrix}, \qquad \text{Equation 7.7}$$

with

$$\sigma_{xy} = \langle xy - \bar{x}\bar{y} \rangle_t\ . \qquad \text{Equation 7.8}$$

The eigenvalues (λ_1, λ_2) of C are equal for a perfectly symmetric motion. We used $s = \sqrt{(\lambda_{max} / \lambda_{min})} < 1.2$ as a threshold. Forces on single-tethered microspheres were then calibrated by applying a low acoustic force for a few minutes and measuring the microsphere positions. Power spectra of the *x* and *y*-motion were calculated and fitted for every individual microsphere. Finally a linear force ramp was applied (because of the quadratic dependence of force on applied voltage this corresponds to a voltage that increases like a square root function). The voltage and corresponding force at which a bond rupture took place was determined from the frame at which a given microsphere leaved the region of interest. To determine this frame, the measured region of interest was compared to a template image made when the microsphere was present at the beginning of the measurement. This was done by setting the following threshold:

$$\Delta Template = \sum_{n=1}^{144} \sqrt{\left(I_{n,meas.} - I_{n,temp.}\right)^2} > 200\ . \qquad \text{Equation7.9}$$

With I_n the intensity of the nth closest pixel to the sub-pixel tracked center of the microsphere (Supplementary Figure 7.6).

Energy landscape of the antibody-antigen bond. The lifetime due to thermal activation of a weak non-covalent bond decreases when subjected to a force. Applying a force tilts the energy landscape, effectively lowering energy barriers, decreasing the likelihood that the bond stays intact. The faster the force is increased, the less time the system has to overcome the energy barriers via thermal

fluctuations. Therefore, the most probable rupture force of a population of bonds will increase as a function of loading rate. Linear regimes that appear over multiple orders of magnitude of loading rates can be interpreted as distinct energy barriers along the unbinding pathway[18]. For the DIG::anti-DIG bond two regimes were observed, which we associate with two barriers. Parameters of these barriers were obtained by fitting the linear regimes with[19]

$$F^* = \frac{k_B T}{\Delta x} \ln \frac{r \Delta x}{k_B T \times k_{off}} \quad , \qquad \text{Equation 7.10}$$

where Δx is the distance between the bound and the transition state, k_{off} is the dissociation constant at zero force and r is the loading rate.

DNA tethers. Both torsionally unconstrained (8.4 kbp) and constrained (10.1 kbp) DNA tethers were used. The 8.4 kbp DNA was obtained from a pKYBI vector that was restricted with KpnI and EcoRI (Fermentas), resulting in a 8364 bp fragment. To the 3'-end overhang, a 29-mer (5'-C(T-DIG)CTC(T-DIG)CT CTC (T-DIG)TC TC(T-DIG) CTT CTC TT GTAC -3') was ligated. The 5'-end overhang was filled in using Klenow exo$^-$ polymerase (Fermentas) using biotin-14-dATP (Invitrogen) and dTTP (Fermentas), resulting in a DNA construct labeled with biotins on one end and digoxigenins on the other, on the same strand. The 10kbp torsionally constrained DNA (gift of David Dunlap) was based on pWM530 and was generated by doubling the length of an earlier construct to give an 11564 bp sequence. Double digesting with SpeI and ApaLI produced a fragment of 10160 bp, which subsequently was ligated to ~1.4 kbp PCR fragments as tethers, containing either biotin or digoxigenin[28]. For the bond rupture measurements of DIG and anti-DIG DNA (1091 bp) with a single DIG label was used as described previously[14]. The DNA tethers were attached to the surface using anti-Dig (Roche, Cat. No. 11 333 089 001). To this end the flow cell was incubated for several minutes with an antibody-containing solution (20 μg/ml) for several minutes. Streptavidin-coated polystyrene (Spherotech) or silica microspheres (BaseClear) were attached to the other end of the DNA molecules.

Buffers and RecA solutions. Experiments on naked DNA were conducted in PBS (138 mM NaCl, 2.7 mM KCl and 10 mM phosphate (pH 7.4); Sigma) supplemented with 5 mM NaN_3 (sodium azide; Sigma), 0.5 mM EDTA (ethylenediaminetetraacetic acid; Sigma) and 20 mg ml^{-1} Casein (Sigma). To fully coat DNA with RecA (Figure 7.3b), a 70 mM MES (pH 6.4) buffer (2-(N-morholino)ethanesulfonic acid; Sigma) was used, with 1 μM RecA (New England Biolabs), 50 mM KCl, 10 mM $MgCl_2$, 1 mM

DTT (dithiothreitol; Sigma) and 1mM ATP (adenosine triphosphate; Sigma). To analyze the binding and unbinding of RecA to DNA (**Figure 7.3c)** a 70 mM Tris-HCL (pH 7.5) buffer was used, containing 0.5 µM RecA, 10 mM $MgCl_2$, 5mM DTT and 1 mM ATP.

Software code. AFS tracking and AFS data analysis implemented in Labview software is made available online. This software package is designed to do live particle tracking and data analysis of a large number of tethered particles in parallel. The software can be downloaded from:

http://figshare.com/articles/AFS_software/1195874

Appendix B: Supplementary figures

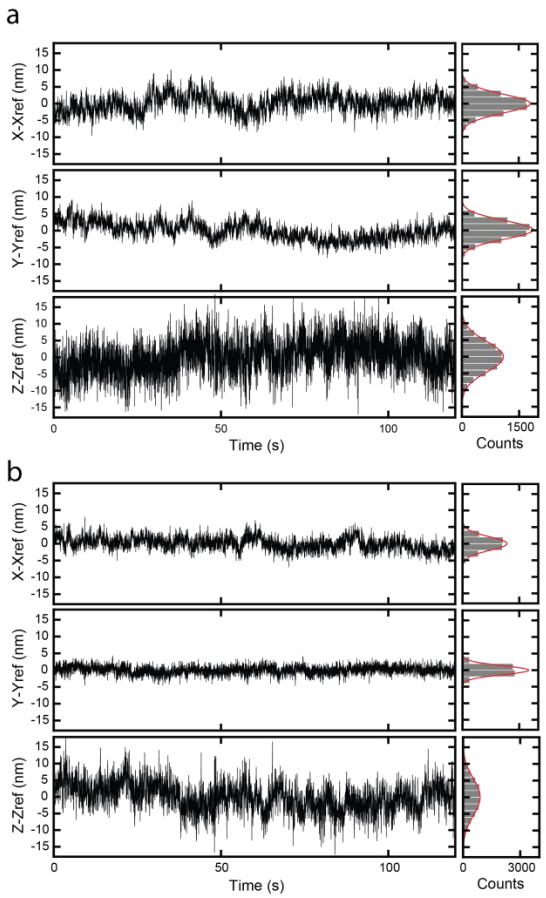

Supplementary Figure 7.1 Accuracy of microsphere tracking in x, y and z. Accuracy of tracking at 50 Hz in x, y, and z of a 4.5 µm diameter polystyrene microsphere (**a**) and a 1.5 µm diameter silica microsphere (**b**). These microspheres were stuck nonspecifically to the flow cell surface. To correct for mechanical drifts a reference microsphere (1.5 µm diameter silica) was tracked simultaneously and its position was subtracted. The standard deviations of the position distributions for the 4.5 µm diameter polystyrene microsphere and 1.5 µm diameter silica microsphere are $\sigma_{x,4.5} = 3$ nm, $\sigma_{y,4.5} = 3$ nm, $\sigma_{z,4.5} = 4$ nm and $\sigma_{x1.5} = 2$ nm, $\sigma_{y,1.5} = 1$ nm, $\sigma_{z,1.5} = 5$ nm respectively.

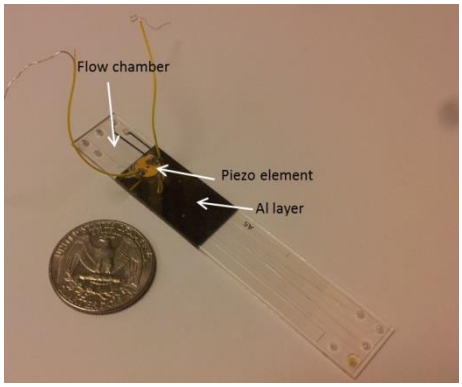

Supplementary Figure 7.2 The AFS device. The piezo element, with wires connected to the electrodes, is glued onto the aluminum layer. A US quarter dollar coin is placed at the side for size perspective.

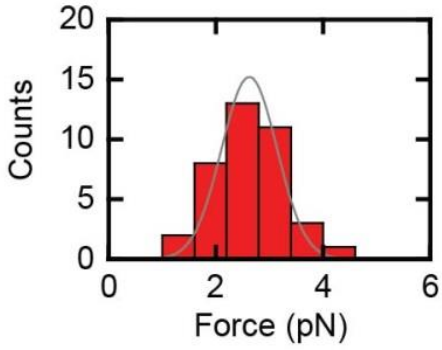

Supplementary Figure 7.3 Histogram of the force distribution. The measured force on DNA (8.4 kbp) tethered microspheres (silica, diameter 1.5 μm) distributed over a distance of more than a millimeter. The grey curve represents the force distribution expected from the size variation from microsphere to microsphere ($\sigma_{bead} \approx 6\%$). This variation is probably the limiting factor of the force homogeneity in our setup.

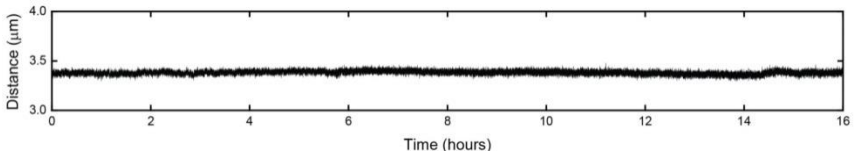

Supplementary Figure 7.4 The stability of the AFS setup. The measured end-to-end distance of a DNA molecule (10.1 kbp) to illustrate the stability of the AFS apparatus. The DNA molecule was tethered to a 4.5 μm polystyrene microsphere that was subjected to an acoustic force of 9 pN. No significant drifts were observed over a timescale of 16 hours.

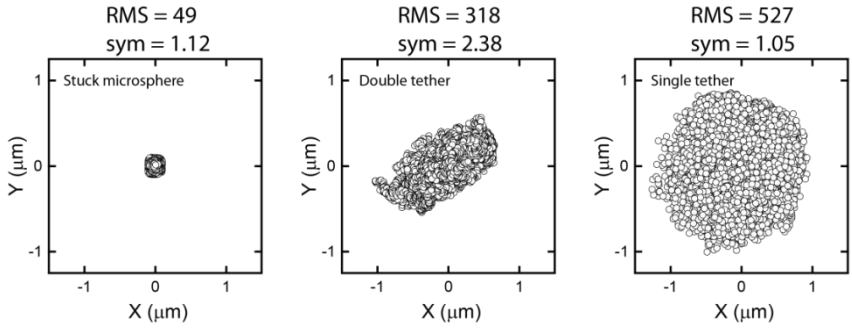

Supplementary Figure 7.5 Selection criteria for single tethers. XY scatter plots for a microsphere that was stuck (left panel), double tethered (middle panel) and single tethered (right panel). Stuck microspheres were discarded by their low RMS value and microspheres tethered to multiple molecules were discarded by their asymmetric motion (high symmetry value).

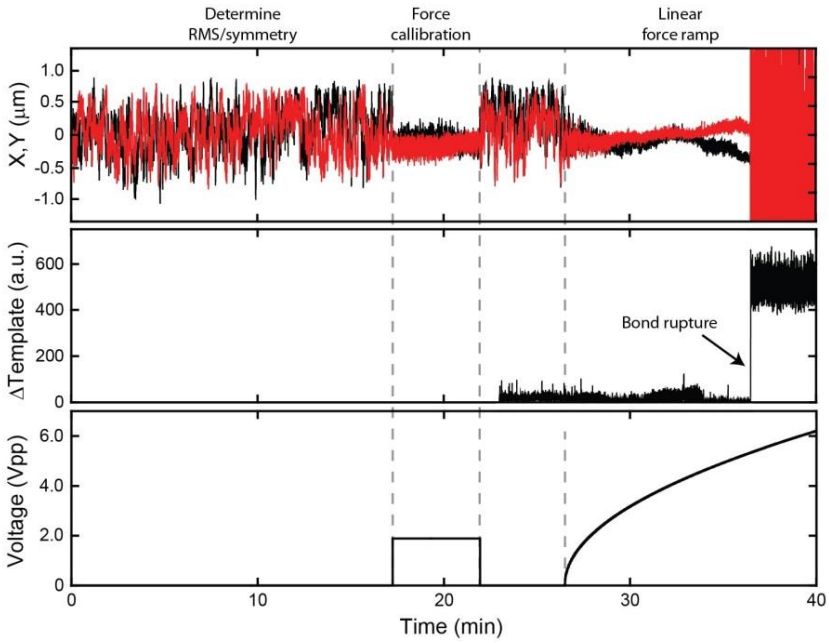

Supplementary Figure 7.6 Typical bond rupture measurement. A typical bond-rupture measurement of a DIG/anti-DIG bond. This measurement was performed for thousands of microspheres in parallel. At the beginning of the measurement no force was applied to determine the RMS and symmetry value of each tether in order to discriminate between single tethered microspheres and microspheres that were stuck or tethered to multiple molecules (**Supplementary Figure 7.5**). To calibrate forces acting on individual microspheres, a constant voltage was applied for several minutes and the power spectrum of the quenched x, y motion was analyzed for each microsphere independently. Finally, a linear force ramp ($\sim 0.02\, pN/s$) was applied. After the Dig/anti-Dig bond breaks, the microsphere leaves the selected tracking region of interest, leading to an increased value of ΔTemplate (equation (7.8), Appendix A) yielding a random tracked positions. Note that, in these experiments, the positions were not corrected for drift.

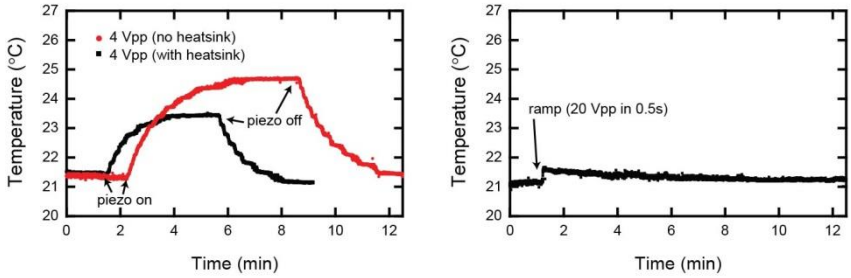

Supplementary Figure 7.7 Sample heating. Temperature measurement of the sample using a Platinum thermocouple that is embedded in the upper glass layer close to the piezo. The left panel shows that the heating is approximately 3°C if 4 Vpp is applied for several minutes. Using a heatsink, a block of aluminum that is connected to the flow cell next to the piezo, decreases heating of the sample by a third. A more efficient heatsink will probably reduce the heating further. The right panel shows that we measure almost no heating for fast force ramps to high voltages (20 Vpp). Note that heating can be decreased if silica microspheres are used instead of polystyrene spheres since less than half the power is needed to achieve the same forces. Another option to decrease the amount of input power is simply using larger microspheres.

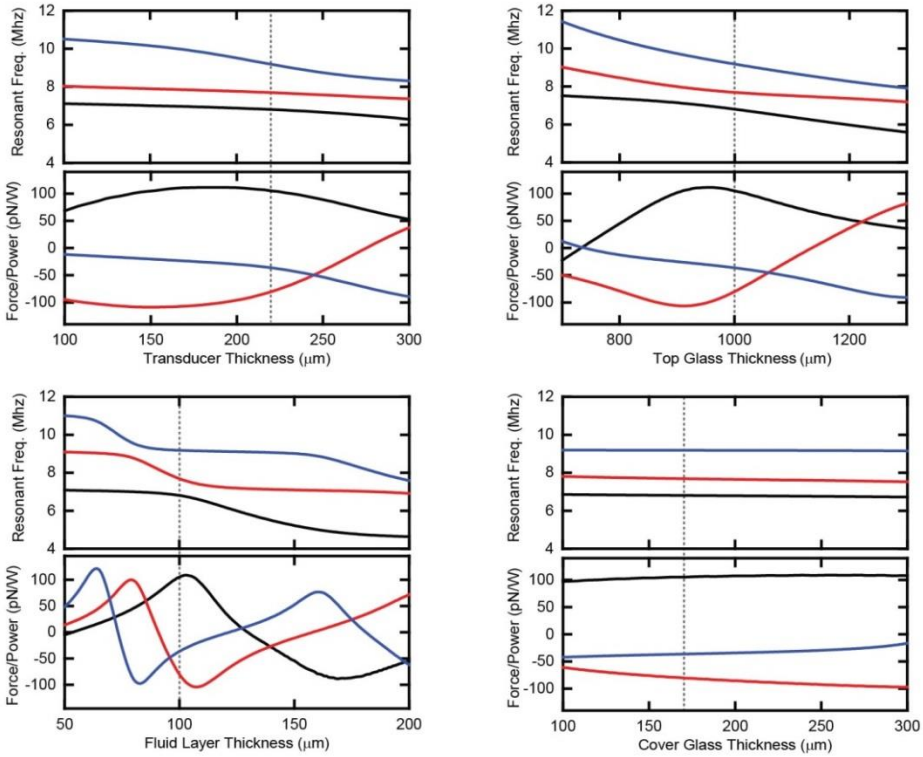

Supplementary Figure 7.8 Influence of layer thicknesses. Simulated frequencies of three acoustic resonances of the probe chamber and the corresponding forces at the upper glass/water interface per electrical input power of the transducer when varying the thickness of an individual layer. A positive force is directed towards the fluid layer and is calculated for 4.5 μm polystyrene microspheres. The dashed lines indicate the actual thicknesses for our device, which are also the values used in the simulation for the layers that are not varied. The results show that varying the fluid layer thickness has the largest influence on the force.

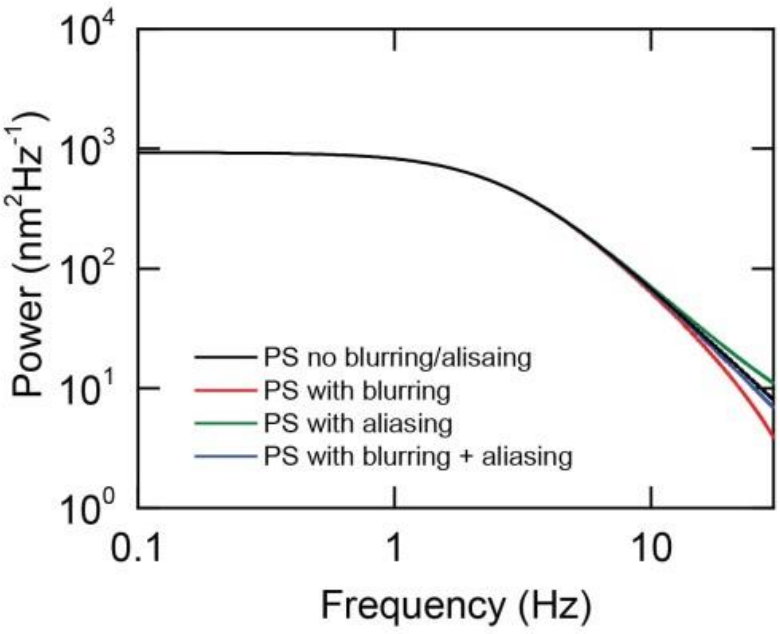

Supplementary Figure 7.9 Effect of blurring and aliasing. Theoretical power spectra calculated for a typical, tethered microsphere (diameter 4.5 µm; DNA length 8.4 kbp) that is subjected to a force of 5 pN. For this frequency range motion blurring due to the finite integration time (15 ms) effectively suppresses the extra power due to aliasing. Therefore there is no significant difference between the power spectrum without blurring or aliasing effects (black line) and the power spectrum that takes both effects into account (blue line).

References

1. Bustamante, C., Cheng, W., Mejia, Y. X. & Meija, Y. X. *Cell* **144,** 480–497 (2011).

2. Neuman, K. C. & Nagy, A. *Nat. Methods* **5,** 491–505 (2008).

3. Herbert, K. M., Greenleaf, W. J. & Block, S. M. *Annu. Rev. Biochem.* **77,** 149–176 (2008).

4. Zhao, Y. *et al. Lab Chip* **13,** 2183–2198 (2013).

5. De Vlaminck, I. & Dekker, C. *Annu. Rev. Biophys.* **41,** 453–472 (2012).

6. Kim, S., Blainey, P. C., Schroeder, C. M. & Xie, X. S. *Nat. Methods* **4,** 397–399 (2007).

7. Halvorsen, K. & Wong, W. P. *Biophys. J.* **98,** L53–5 (2010).

8. Fazio, T., Visnapuu, M.-L., Wind, S. & Greene, E. C. *Langmuir* **24,** 10524–10531 (2008).

9. Smith, S. B., Cui, Y. & Bustamante, C. *Science (New York, N.Y.)* **271,** 795–799 (1996).

10. Van Mameren, J. *et al. Proc. Natl. Acad. Sci. U. S. A.* **106,** 18231–18236 (2009).

11. Settnes, M. & Bruus, H. *Phys. Rev. E* **85,** 016327 (2012).

12. Heller, I. *et al. Nat. Methods* **10,** 910–916 (2013).

13. Glynne-Jones, P., Boltryk, R. J. & Hill, M. *Lab Chip* **12,** 1417–1426 (2012).

14. Laurens, N. *et al. Nucleic Acids Res.* **37,** 5454–5464 (2009).

15. Odijk, T. *Macromolecules* **28,** 7016–7018 (1995).

16. Chen, Z., Yang, H. & Pavletich, N. P. *Nature* **453,** 489–493 (2008).

17. Fu, H., Le, S., Muniyappa, K. & Yan, J. *PLoS One* **8,** e66712 (2013).

18. Merkel, R., Nassoy, P., Leung, a, Ritchie, K. & Evans, E. *Nature* **397,** 50–53 (1999).

19. Neuert, G., Albrecht, C., Pamir, E. & Gaub, H. E. *FEBS Lett.* **580,** 505–509 (2006).

20. Moayed, F., Mashaghi, A. & Tans, S. J. *PLoS One* **8,** e54440 (2013).

21. Hill, M., Shen, Y. & Hawkes, J. J. *Ultrasonics* **40,** 385–392 (2002).

22. Hill, M., Townsend, R. J. & Harris, N. R. *Ultrasonics* **48,** 521–528 (2008).

23. Gosse, C. & Croquette, V. *Biophys. J.* **82,** 3314–3329 (2002).

24. Te Velthuis, A. J. W., Kerssemakers, J. W. J., Lipfert, J. & Dekker, N. H. *Biophys. J.* **99,** 1292–1302 (2010).

25. Berg-Sørensen, K. & Flyvbjerg, H. *Rev. Sci. Instrum.* **75,** 594–612 (2004).

26. Norrelykke, S. F. & Flyvbjerg, H. *Rev. Sci. Instrum.* **81,** 075103 (2010).

27. Han, L., Lui, B. & Blumberg, S. *Mathematics of DNA Structure, Function and Interactions* **150,** 123–138 (2009).

28. Dunlap, D., Yokoyama, R. & Ling, H. *Nucleic Acids Res.* **40,** 11281–11291 (2012).

Nederlandse Samenvatting

De blauwdruk van het leven afgetast: de ontwikkeling en toepassing van nieuwe enkel-molecuul technieken

Hier vindt u een zeer beknopte samenvatting van het wetenschappelijke werk dat ik verricht heb tijdens mijn vier jaar durende promotie.

In de introductie, die geschreven is voor een breder publiek, ga ik in op de rol van de natuurkunde in de biologie. Deze rol is tweezijdig, aan de ene kant ontwikkelen natuurkundigen geavanceerde apparatuur die onderzoekers in staat stelt biologische vraagstukken op te lossen. Aan de andere kant hebben natuurkundigen een belangrijke rol te vervullen door hun krachtige onderzoeksmethodiek toe te passen om de mysteries van het leven op te lossen. Deze methodiek is kort gezegd gebaseerd op het versimpelen van complexe systemen zodat we er modellen van kunnen maken die gebaseerd zijn op de fundamentele wetten van de natuurkunde. Deze modellen verschaffen op hun beurt weer inzicht in de complexe systemen die we graag willen begrijpen. Dit inzicht kan op zijn beurt weer gebruikt worden om meer realistische modellen te creëren. Aan dit iteratieve proces doen wetenschappers over heel de wereld mee, wat er voor zorgt dat we zo onze krachten bundelen in de zoektocht naar antwoorden. In de biofysica bestaan de complexe systemen uit levende systemen. Gedacht hierbij kan worden aan een cel, een organisme of zelfs een compleet ecosysteem. In mijn promotie heb ik mij ten eerste gericht op het ontwikkelen van geavanceerde apparatuur die het mogelijk maakt om onderzoek te verrichten naar de moleculaire bouwstenen, zoals DNA en eiwitten, van het leven. Deze technieken zijn “enkel-molecuul” technieken, wat betekent dat ze in staat zijn om daadwerkelijk de individuele mechanische eigenschappen en interacties van deze bouwstenen te kunnen meten. Deze apparatuur heb ik daarnaast gebruikt om biologische vraagstukken te beantwoorden middels de methodiek die hierboven beschreven staat. Al het onderzoek dat ik verricht heb is gedaan in een zogenaamde *in vitro* omgeving. Dat betekent dat ik DNA, eiwitten en hun interacties buiten de cel heb onderzocht. Dit heeft als grote voordeel dat het onderzochte systeem een stuk eenvoudiger is en dat er goede controle is over de experimentele condities. Het nadeel is dat dit niet de natuurlijke *in vivo* omgeving is van het DNA en de eiwitten, wat vaak invloed heeft op de gemeten resultaten.

In hoofdstuk 2 wordt een nieuwe techniek beschreven die wij ontwikkeld hebben om individuele DNA moleculen te kunnen bestuderen in een omgeving die vergelijkbaar is met de cellulaire om zo een brug te leggen tussen de artificiële *in vitro* met de natuurlijke *in vivo* omgeving. In een cel is DNA volledig bedekt en omgeven met eiwitten. "Naakt" DNA bestaat in de natuurlijke omgeving dus niet. Het doel van het onderzoek in dit hoofdstuk was een apparaat ontwikkelen dat DNA eiwit interacties kan meten op DNA dat zowel bedekt als omgeven is met grote hoeveelheden eiwitten. Het ontwikkelde apparaat maakt gebruik van een combinatie van een optisch pincet en een super resolutie confocale fluorescentie microsoop. Het optisch pincet gebruiken we om twee kleine bolletjes (orde groote van een) vast te houden met een laser. Dit stelt ons in staat om deze bolletjes zeer nauwkeurig te bewegen in drie dimensies. Deze bolletjes zijn zo behandeld dat uiteinden van DNA moleculen eraan vast blijven plakken. Zo kunnen wij tussen deze bolletjes individuele DNA moleculen vasthouden en heel nauwkeurig bewegen. De confocale super resolutie microscoop zetten wij vervolgens in om met verschillende gepulseerde lasers over dit DNA te scannen en zo live te filmen hoe eiwitten op het DNA bewegen. In het hoofdstuk laten we zien dat we deze eiwitten op het DNA kunnen volgen bij eiwit-concentraties (vergelijkbaar met cellulaire concentraties) die veel hoger liggen dan met andere technieken mogelijk is. Daarnaast kunnen we met de super resolutie techniek (genaamd STED) het DNA filmen met een resolutie die zes keer beter is dan met conventionele fluorescentie microscopen. Deze verbeterde resolutie is essentieel om individuele eiwitten te kunnen volgen op dichtbevolkt DNA. We sluiten dit hoofdstuk af met een demonstratie meting die laat zien dat het transcriptie eiwit TFAM zich anders gedraagt op DNA in een cellulaire omgeving (veel eiwitten op het DNA in een omgeving met hoge eiwit concentraties) in vergelijking met een artificiële omgeving ("naakt" DNA in zeer lage eiwit concentraties). Met deze demonstratie meting tonen we aan dat het belangrijk is dat enkel-molecuul experimenten worden verricht in de natuurlijke omgeving van deze moleculen en dat onze techniek hiertoe in staat is.

In hoofdstuk 3 vergelijken wij verschillende fluorescentie microscopie technieken en wordt er bepaalt hoe deze technieken het beste ingezet kunnen worden om de meest waardevolle data te verkrijgen als men de mobiliteit van eiwitten op DNA wil bestuderen. Om dit goed in kaart te brengen hebben we een groot aantal computer simulaties, die eiwit mobiliteit op DNA nabootst, uitgevoerd en geanalyseerd. Onze algemene conclusies uit dit hoofdstuk vormen richtlijnen voor onderzoekers om hun experimenten op te stellen. Dit verzekert hen de meest waardevolle data met

betrekking tot de mobiliteit van eiwitten op DNA te vergaren met hun experimenten.

Hoofdstuk 4 heeft betrekking op het onderzoeken van een biologisch vraagstuk gebruik makende van enkel-molecuul technieken. Ons DNA raakt continu beaschadigd door natuurlijke processen in de cel of door omgevingsfactoren. Soms zijn deze beschadigingen dermate ernstig dat de gehele DNA streng breekt. Voor de overleving van de cel is het essentieel dat deze DNA breuken snel gerepareerd worden. In onze cellen zijn meerdere eiwitten verantwoordelijk voor deze reparatie. Ondanks dat de verschillende eiwitten zijn geïdentificeerd, is het onbekend wat de verschillende functies van deze eiwitten tijdens het reparatie proces zijn. Om dit op te helderen hebben we gebruik gemaakt van een optisch pincet die vier bolletjes en daarmee twee individuele DNA moleculen kan manipuleren. Ons onderzoek toont aan dat XRCC4 en XLF, eiwitten met vergelijkbare structuur, stabiel op DNA binden in grote complexen. Deze complexen zijn in staat over DNA te bewegen en blijven plakken op het uiteinden van DNA fragmenten. Daarnaast zijn ze in staat twee verschillende DNA moleculen aan elkaar te plakken door middel van mobiele eiwitbruggen. Een model. Gebaseerd op deze bevindingen laat zien wat de rollen van XRCC4 en XLF binnen het reparatie proces zijn.

Hoofdstuk 5 heeft betrekking op een computer simulatie programma die data kan voorspellen van bepaalde enkel-molecuul experimenten. Veel enkel-molecuul technieken maken gebruik van bolletjes op de nanometer of micrometer schaal die verbonden zijn aan een oppervlakte via een bio-molecuul. Dit bio-molecuul kan bijvoorbeeld een eiwit, DNA of RNA zijn. De bolletjes kunnen in sommige technieken gemanipuleerd worden door bijvoorbeeld lasers, magnetisme, vloeistofstromen of ultrasoon geluid. Daarmee kan men effectief de bio-moleculen manipuleren. Door tegelijkertijd de bolletjes te volgen in de tijd is het mogelijk de mechanische eigenschappen, zoals de lengte of de stijfheid, van het bio-molecuul te bepalen. Mijn simulatie programma kan nauwkeurig de beweging van zo'n bolletje beschrijven in de tijd. Deze beweging hangt af van veel verschillende factoren, zoals de grootte van het bolletje, de stijfheid van het bio-molecuul, de viscositeit van het medium waarin het bolletje zich bevindt, de temperatuur van het medium, enz. Deze verschillende factoren kunnen ingevoerd worden in het programma waarna de beweging van het bolletje in de tijd wordt berekend. Ik laat in het hoofdstuk zien dat de gesimuleerde data met grote nauwkeurigheid overeenkomt met experimentele data die gemeten is met vier verschillende technieken. Hiermee laat

ik zien dat ik veel verschillende experimenten kan beschrijven met mijn simulatie programma. Hierdoor is dit programma een krachtig hulpmiddel om de uitkomst van biofysische experimenten te voorspellen en dieper inzicht in gemeten data te creëren.

Hoofdstuk 6 en 7 beschrijft nieuwe technieken die grote hoeveelheden biomoleculen simultaan kunnen manipuleren en meten. Het voordeel hiervan is dat zo snell, voldoende statistische relavante data kan worden gemeten, wat essentieel is voor het onderbouwen van ondezoeksresultaten. In hoofdstuk 6 betreft het een techniek die meerdere moleculen kan manipuleren door gebruik te maken van een krachtige laser. Deze laser bundel is dermate krachtig dat het meerdere micrometer bolletjes weg kan duwen. Door tussen deze bolletjes en een oppervlakte biologische moleculen te plakken is het mogelijk gecontroleerde krachten uit te oefenen op deze biomoleculen. In het hoofdstuk wordt gedemonstreerd dat we met deze techniek biologische relevante krachten kunnen behalen die we op een zeer nauwkeurige manier kunnen varieren. We demonstreren onze techniek door te meten hoe een eiwit lusjes in DNA legt en hoe deze interactie afhangt van de hoeveelheid kracht die op het DNA wordt gezet.

Hoofdstuk 7 behandelt een nieuw ontwikkelde techniek waarmee biomoleculen met zeer grote aantallen tegelijk gemanipuleerd kunnen worden met ultrasoon geluid. Dit is de eerste techniek die gebruik maakt van geluid om metingen te verrichten op de moleculaire schaal. Het ultrasoon geluid wordt geproduceerd door een piezo element die wij op een glazen chip lijmen met een vloeistof kanaal waarin wij vloeistoffen kunnen inbrengen. In dit vloeistofkanaal brengen wij DNA of andere biomoleculen aan tussen een oppervlakte en micrometer grootte bolletjes. Met akoestische krachten kunnen wij deze micrometer grootte bolletjes en daarmee ook de biomoleculen manipuleren. De grote voordelen van deze techniek is dat de techniek zeer eenvoudig is en dat er een zeer groot aantal moleculen (duizenden) tegelijkertijd gemeten kunnen worden. In het hoofdstuk hebben we uiteenlopende metingen verricht die de kracht van deze techniek laten zien. Door de verschillende voordelen is deze techniek een belangrijke toevoeging voor het enkel-molecuul veld en wij anticiperen dat deze wijdverspreid gebruikt zal gaan worden.

Een groot gedeelte van mijn promotie heb ik besteed aan het onwikkelen van nieuwe instrumentatie voor het enkel-molecuul veld. Ik hoop dat deze technieken binnen en buiten de VU gebruikt zullen gaan worden om wetenschappelijke vraagstukken op te lossen.

Acknowledgements

Het proefschrift dat voor u ligt is het resultaat van een promotietraject van vier jaar. Voor het behalen van dit resultaat ben ik dank verschuldigd aan een groot aantal mensen. Een aantal daarvan zou ik hier graag expliciet willen noemen.

Mijn dank gaat allereerst uit naar mijn beide promotoren, Gijs en Erwin. Toen ik aan mijn afstudeerstage in de groep begon was ik vrij overtuigd dat ik niet wilde promoveren. Door de leuke sfeer en uitdagende werkzaamheden binnen jullie vakgroep ben ik tijdens deze stage van mening veranderd en besloten toch te gaan promoveren. Hier heb ik geen moment spijt van gehad. Als mijn eerste promotor Gijs ben ik dankbaar voor alle uren die we enthousiast gebrainstormd hebben om richting te geven aan de verschillende projecten. Door jouw begeleiding en hulp hebben we het onderzoek en daarmee de papers tot een niveau kunnen brengen waar ik enorm trots op ben. Ik ben erg blij dat je mij het vertrouwen hebt gegeven om tijd en budget te besteden aan projecten met een onzekere uitkomst. Erwin, jij bent ook altijd intensief betrokken geweest met de verschillende projecten, waarvoor veel dank. Je hebt enorm veel kennis, variërend van het schijven van een perfect abstract tot diepgaande technische details. Je bent altijd erg toegankelijk geweest om hulp te vragen en weet mensen enthousiast te maken over hun eigen resultaten. Het is me altijd een genoegen geweest om met jullie om te gaan binnen en buiten het lab.

Veel dank van mij gaat uit naar Iddo. Met jou heb ik de meeste uren in een lab besteed en heb deze samenwerking als erg goed ervaren. Ik heb enorm veel kunnen leren van jouw praktische manier van werken en dit heeft veel bijgedragen aan alle projecten waar ik aan heb gewerkt. Ineke, onze publicatie is net de deur uit en hopelijk wordt het in een mooi paper geaccepteerd. Ik heb altijd prettig met je samengewerkt. Jouw bijdrage, waaronder honderden complexe experimenten, is enorm, waarvoor veel dank. Graag wil ik Douwe bedanken voor de samenwerking aan de AFS. We zijn hier samen aan begonnen toen het nog niet zeker was of het überhaupt zou werken. Samen hebben we het in zeer korte tijd boven alle verwachtingen werkend gekregen. Zonder jouw bijdrage was dit zeker niet zo snel en soepel verlopen. Onno, graag zou ik jou willen bedanken voor alle tijd en moeite die jij in de verschillende software programma's hebt gestopt. Dit draagt enorm bij

aan de kwaliteit van de data die gemeten kan worden en daarmee aan het succes van de verschillende projecten. Niels, ooit mijn begeleider binnen de groep, heeft mij kennis laten maken met de biofysica. Bedankt voor de samenwerking en mij enthousiast maken om een promotie te gaan doen.

Daan, ooit samen begonnen in de oude studentenkamer in de kelder, bedankt voor de gezelligheid en succes met de verdere afronding van jouw promotie. Jona, bedankt voor alles wat je door de jaren heen hebt georganiseerd voor anderen en natuurlijk ook voor de leuke sfeer. Tjalle, ook jou natuurlijk enorm bedankt. Wij hebben veel lol gehad op werk, op conferenties, roadtrips en in de kroeg. Laten we dit, op de conferenties en het werk na, blijven doen. Bram, buurman, bedankt voor jou bijdrage aan mijn promotie. Ik kan niemand anders bedenken waar ik liever nutteloze time-lapse filmpjes mee maak.

Peter, dude, thanks for the good times and hope to see you around in Amsterdam or at future conferences. Pierre and Jules (nice roadtrip), all the luck in France and please let me know when visiting Amsterdam. Seyda, I hope you find a position soon and thanks for the good times in and outside the lab. Thanks a lot to Andreas, you were always available to help me out with various problems. Felix, thanks for the great time within the office, during the US road trip and at parties. We will hopefully be working together for a long time and I am quite confident we will enjoy.

Thanks to my Austrian colleagues Monika and Gregor. You inspired and helped us to develop the AFS instrument. I would also like to thank (old)-colleagues from the Nynke Dekker lab (Jan and Zhongbo) and Karl from the Antoine van Oijen lab for providing me with various data sets.

De opstellingen die ik gebouwd heb tijdens mijn promotie heb ik alleen kunnen doen met de ondersteuning van zowel de fijnmechanische als de elektronische werkplaats. Joost, Rob, Pieter, Peter, Niek, Mario, Jurriaan, Jacob, Frans, Tim, Pierre, Lex en Mathijs, enorm bedankt.

I also want to thank other non-group members with whom I did spend many coffee breaks. Boy, Dirk, Johannes, Fabio (nice roadtrip), Frank, Max (nice roadtrip), Miriam, Jianan, Joshua and Kari. Jelmer ook bedankt, vaak heb ik je lastiggevallen en je hebt me altijd direct goed geholpen. Ik wil in het bijzonder ook Mattijs bedanken. Je hebt vaak goed mee kunnen denken over problemen en dit is altijd erg nuttig geweest. Geweldig dat we nog langere tijd collega's zullen zijn.

Geraldine, Ienas, Marian, Astrid, thanks for the good times in the period we were both in the group. Aravindan, Mariska, Vandana, Ning, Graeme, Jordi, Els, Sandrine, Sandrijn and Wouter, thank you for all the good times at the coffee breaks, weekly meetings and friday drinks.

Special thanks to Andrea. Thanks for all the good times the previous years. I am happy to have you as a paranimf. Currently we are at the beginning of an exciting adventure with Lumicks, which is great to share with you. I would also like to thank all my new colleagues. Olivier, Willem, Jerom, Michiel, Rosalie, Vikram, Burak, Kim, Sergey and Vitali, let's make it happen.

Graag wil ik ook al mijn vrienden buiten mijn werk erg bedanken, waaronder de jongens van Montagne en de Whoeei app. Jullie hebben enorm bijgedragen aan de mooie periode van de afgelopen jaren. Jaap, enorm leuk dat je uit China overkomt voor mijn promotie. Ik ben erg blij om jou aan mijn zijde te hebben als paranimf.

Uiteraard heeft ook mijn familie bijgedragen aan mijn promotie. Veel dank aan mijn ouders, Han en Cox. Jullie hebben mijn keuzes altijd gesteund en mij alle vrijheid gegeven mij mijn eigen weg te laten vinden. Natuurlijk ook mijn zussen en broers bedankt. Sofie, Judith, Flip, Erik en Vincent, jullie zijn allemaal prachtige mensen en ben trots op jullie.

Als laatste wil ik graag mijn allerliefste vriendin Samantha bedanken. We zijn inmidels al een stukje langer bij elkaar dan mijn promotie geduurd heeft en hoop dat dit nog maar het begin is. Je maakt me gelukkig.

List of Publications

1. Iddo Heller, Gerrit Sitters, Onno D Broekmans, Géraldine Farge, Carolin Menges, Wolfgang Wende, Stefan W Hell, Erwin JG Peterman & Gijs JL Wuite, STED nanoscopy combined with optical tweezers reveals protein dynamics on densely covered DNA, *Nature Methods* 10, 910-916 (2013)
   Chapter 2

2. Iddo Heller, Gerrit Sitters, Erwin JG Peterman & Gijs JL Wuite, Dansende eiwitten op drukbezet DNA gefilmd, *Nederlands Tijdschrift voor Natuurkunde* 9, 312-317 (2014)
   Chapter 2

3. Iddo Heller*, Gerrit Sitters*, Onno D Broekmans, Andreas S Biebricher, Gijs JL Wuite & Erwin JG Peterman, Mobility Analysis of Super-Resolved Proteins on Optically Stretched DNA: Comparing Imaging Techniques and Parameters, *Chemphyschem* 15, 727-33 (2014)
   Chapter 3

4. Rosalie PC Driessen, Gerrit Sitters, Niels Laurens, Geri F Moolenaar, Gijs JL Wuite, Nora Goosen, Remus Th Dame, Effect of temperature on the intrinsic flexibility of DNA and its interaction with architectural proteins, *Biochemistry* 53, 6430-6438 (2014)
   Not in this thesis

5. Gerrit Sitters*, Douwe Kamsma*, Gregor Thalhammer, Monika-Ritsch-Marte, Erwin J G Peterman‡ & Gijs J L Wuite‡, Acoustic force spectroscopy, *Nature Methods* **12**, 47-50 (2015)
   Chapter 7

6. Gerrit Sitters*, Niels Laurens*, Emile J de Rijk, Holger Kress, Erwin J G Peterman & Gijs J L Wuite, Optical Pushing: A tool for highly parallelized bionano-sensing
   Chapter 6 - Submitted

7. Ineke Brouwer*, Gerrit Sitters*, Andrea Candelli, Stephanie J. Heerema, Abinadabe J. de Melo, Davide Normanno, Mauro Modesti‡, Erwin JG Peterman‡, Gijs JL Wuite‡, Sliding XRCC4-XLF sleeves bridge DNA and connect DNA-ends
   Chapter 4 – Submitted

8. Gerrit Sitters, Karl Duderstadt, Erwin JG Peterman, Gijs JL Wuite. Brownian dynamics simulation of tethered microspheres
Chapter 5 – In preparation

*Joint first authors, ‡Joint last authors